UNIVERSITÉ DE MONTRÉAL

Numerical Solutions of Three-Dimensional Transonic Flows Based on Upwind Schemes

par

Ge-Cheng Zha
DÉPARTEMENT DE GÉNIE MÉCANIQUE
ÉCOLE POLYTECHNIQUE

THESE PRÉSENTÉE EN VUE DE L'OBTENTION
DU GRADE DE PHILOSOPHIAE DOCTOR (Ph. D.)
(GÉNIE MÉCANIQUE)
Avril 1994

© Ge-Cheng Zha 1994

National Library of Canada
Bibliothèque nationale du Canada

Acquisitions and Bibliographic Services Branch
Direction des acquisitions et des services bibliographiques

395 Wellington Street
Ottawa, Ontario
K1A 0N4

395, rue Wellington
Ottawa (Ontario)
K1A 0N4

Your file Votre référence

Our file Notre référence

The author has granted an irrevocable non-exclusive licence allowing the National Library of Canada to reproduce, loan, distribute or sell copies of his/her thesis by any means and in any form or format, making this thesis available to interested persons.

L'auteur a accordé une licence irrévocable et non exclusive permettant à la Bibliothèque nationale du Canada de reproduire, prêter, distribuer ou vendre des copies de sa thèse de quelque manière et sous quelque forme que ce soit pour mettre des exemplaires de cette thèse à la disposition des personnes intéressées.

The author retains ownership of the copyright in his/her thesis. Neither the thesis nor substantial extracts from it may be printed or otherwise reproduced without his/her permission.

L'auteur conserve la propriété du droit d'auteur qui protège sa thèse. Ni la thèse ni des extraits substantiels de celle-ci ne doivent être imprimés ou autrement reproduits sans son autorisation.

ISBN 0-315-93393-3

Canada

UNIVERSITÉ DE MONTRÉAL

ÉCOLE POLYTECHNIQUE

Cette thése intitulée:

Numerical Solutions of Three-Dimensional Transonic Flows Based on Upwind Schemes

Présentée par: Ge-Cheng Zha

en vue de l'obtention du grade de: Philosophia Doctor (Ph. D.)

a été dument acceptée par le jury d'examen constitué de:

M.	VASSEUR, Patrich	Ph.D., Président
M.	BILGEN, Ertugrul	Ph.D., Supervisor
M.	PRUD'HOMME, Michel	Ph.D.
M.	MARTINUZZI, Robert	Ph.D.

Dedicated to my wife Wen-Qing Liu, my son David Zha and my parents

SOMMAIRE

Le but de cette thèse est de développer des techniques numériques afin de simuler des écoulements transsoniques et tridimensionnels, d'une façon précise et efficace, pour les schémas "Upwind". Deux techniques ont été développées en parallèle: 1) un algorithme URS (Upwind Relaxation Sweeping) très efficace a été suggéré pour calculer, en régime transitoire tridimensionnel, les équations d'Euler et de Navier Stockes. 2) un nouveau schéma FVS (Flux vector Splitting) à faible diffusion a été suggéré pour capturer les ondes de choc et les discontinuités de contact.

Les équations non dimensionnelles d'Euler et de Navier Stockes en trois dimensions, sous la forme conservatrice et en coordonnés cartésiennes, sont présentés ci-dessous.

$$\frac{\partial U}{\partial t}+\frac{\partial F}{\partial x}+\frac{\partial G}{\partial y}+\frac{\partial H}{\partial z}=\alpha\frac{1}{Re}\left[\frac{\partial R}{\partial x}+\frac{\partial S}{\partial y}+\frac{\partial T}{\partial z}\right]$$

Où

$$U=\begin{bmatrix}\rho\\ \rho u\\ \rho v\\ \rho w\\ e\end{bmatrix}\quad F=\begin{bmatrix}\rho u\\ p+\rho u^2\\ \rho uv\\ \rho uw\\ (e+p)u\end{bmatrix}\quad G=\begin{bmatrix}\rho v\\ \rho uv\\ p+\rho v^2\\ \rho vw\\ (e+p)v\end{bmatrix}\quad H=\begin{bmatrix}\rho w\\ \rho uw\\ \rho vw\\ p+\rho w^2\\ (e+p)w\end{bmatrix}$$

$$R=\begin{bmatrix}0\\ \tau_{xx}\\ \tau_{xy}\\ \tau_{xz}\\ R_5\end{bmatrix} \qquad S=\begin{bmatrix}0\\ \tau_{xy}\\ \tau_{yy}\\ \tau_{yz}\\ S_5\end{bmatrix} \qquad T=\begin{bmatrix}0\\ \tau_{xz}\\ \tau_{yz}\\ \tau_{zz}\\ T_5\end{bmatrix}$$

Quand α prend la valeur de 1, il s'agit de l'équation d'Euler pour l'écoulement potentiel et quand α prend la valeur de 0, il s'agit de l'équation de Navier-Stockes. Pour discrétiser les équations utilisantes la méthode des volumes finies, les équations sont solutionnées sous forme d'intégrale.

L'algorithme URS doit exécuter une itération sur la relaxation sur tous les plans verticaux parallèles à l'écoulement, le sens de progression d'un plan à un autre changeant à chaque étape. L'analyse de la stabilité linéaire démontre que l'algorithme URS sans factorisation est inconditionnellement stable. L'algorithme est indépendant du choix global de la direction de balayage. De plus, en choisissant la direction ayant une relative faible variation de gradient comme direction de balayage, l'algorithme peut avoir un degré de stabilité plus grand. Vu que les erreurs introduites ne peuvent être approximées, l'algorithme URS peut atteindre un nombre CFL très grand, jusqu'à l'ordre de 10^6 pour un nombre CFL maximum, et par conséquent le

taux de convergence y est le plus rapide. Les besoins en mémoire sont minimisés car les matrices ne sont stockées que dans le plan de calcul. De plus le temps CPU est sauvé parce qu'un balayage est capable de solutionner toutes les inconnues dans l'ensemble du champs de flux.

La différence finie "Upwind" est utilisée pour les termes convectifs et de pression et la différence finie "centrale" est utilisée pour les termes de flux de chaleur et de cisaillement. La différence finie "Upwind" est effectuée en utilisant le FVS (Flux Vector Splitting) de Van Leer. La différence finie de flux du type MUSCL est utilisée pour évaluer le flux passant à travers l'interface d'une cellule. Il faut tout d'abord déterminer l'état conservative des variables et par la suite, évaluer le flux d'interface. La différence finie exacte peut être augmentée jusqu'au troisième ordre. Pour garder la dominance diagonale et sauver les calculs, la différence finie du premier ordre est utilisée pour les termes implicites et par conséquence la matrice M est penta-diagonale. L'équation de matrice pour les cellules (i,j,k) peut par conséquent être écrite comme suit:

$$B\delta U^{n+1}_{i,j+1,k} + A\delta U^{n+1}_{i,j,k} + C\delta U^{n+1}_{i,j-1,k} + E\delta U^{n+1}_{i-1,j,k} + D\delta U^{n+1}_{i+1,j,k}$$

$$= RHS^{n,\,n+1}_{inviscid} + RHS^{n}_{viscous}$$

Où les coefficients A, B, C, D et E sont des blocs de matrice 5x5.

La ligne d'itération de Gauss-Seidel est employée pour inverser les matrices au bloc composé de cellules avec le même indice k. Deux balayages sont effectués au bloc k, un en avant et l'autre en arrière.

Les équations d'Euler, pour les fluides compressibles et en trois dimensions, sont solutionnées avec l'algorithme URS pour étudier l'écoulement interne d'une tuyère non-axisymétrique connectée à un conduit à transition de section; de section circulaire à une section rectangulaire. Les cas avec et sans tourbillon (Swirl) à l'entrée ont été calculés. Les résultats obtenus concordent bien avec les résultats expérimentaux. Il a été trouvé que, pour un écoulement avec un tourbillon à l'entrée, les lignes de courant transversales se déplacent vers la droite sur la paroi supérieure et vers la gauche sur la paroi inférieure. Les expériences de calcul démontrent que l'algorithme URS dépend des dimensions de la grille. Pour le cas de la tuyère non-axisymétrique avec les réflexions et intersection des ondes de choc, les résultats de calcul concordent également très bien avec les résultats expérimentaux. Un tunnel en trois dimensions avec une structure complexe d'onde de choc a été également calculé. La structure d'onde de choc varie avec les différentes pressions arriéres. La structure de l'onde de choc calculée nèst pas la meme que celles obtenues par les résultats expérimentaux parce qu'un modèle d'écoulement potentiel est utilisé et qu'une pression exacte n'est pas disponible. Les résultats obtenus démontrent que l'algorithme URS est très efficace et robuste.

Cinq tuyères non-axisymétriques convergentes-divergentes aux condition de design sont calculées en solutionnant les équations tridimensionnelles de Navier-Stockes à

l'aide de l'algorithme URS.

De rapides taux de convergence ont été obtenus. Les calculs ont pour l'objet d'étudier l'effet de la configuration du col, en augmentant le rayon de son arc circulaire, sur la performance interne de tuyère. La configuration du col a résulté en un effet positif sur le coefficient de perte mais ne démontre pas d'amélioration significative sur le taux de poussée interne. L'effet moyen de la configuration du col sur la pression statique est négligeable. Tous les résultats numériques comme la distribution de pression statique, le coefficient de perte et le taux de poussée interne ont été comparés aux résultats expérimentaux et ils se concordent bien. Les codes d'ordinateur développés dans cet étude pourront être utilisés plus tard comme utile pour designer les tuyères.

Le nouveau schéma FVS (Flux Vector Splitting) utilise la composante de la vitesse normale à l'interface des volumes de contrôle comme vitesse caractéristique et permet de calculer chaque flux de masse individuel disparaissant au point de stagnation. La dissipation numérique pour les équations de la masse et de la quantité de mouvement disparaît avec le flux de masse. Un des termes diffusifs de l'équation d'énergie ne disparaît pas au point de stagnation. Cependant la diffusion comprend également le degré de l'erreur de troncature. Une diffusion numérique plus faible pour les écoulements visqueux peut être assurée davantage en utilisant l'ordre de la différence finie la plus grande. En conséquence, pour les écoulements visqueux, le présent schéma peut être plus précise que celui de FVS sans dissipation de flux de masse au point de stagnation. Le schéma avec le nombre de Mach polynomiale de degré un, le plus naturel et le plus petit, est très simple et facile à

mettre en oeuvre.

La forme générale du nouveau schéma FVS en trois dimensions est présentée comme suite:

Posons

$$D=|U_n|\begin{bmatrix}\rho\\ \rho u\\ \rho v\\ \rho w\\ e\end{bmatrix}+\begin{bmatrix}0\\ pM_n n_x\\ pM_n n_y\\ pM_n n_z\\ pa\end{bmatrix}$$

La composante normale de l'interface de flux non-visqueux P1 est:

$$P_1 = C + P$$

Où

$$C = U_n\begin{bmatrix}\rho\\ \rho u\\ \rho v\\ \rho w\\ e\end{bmatrix} \qquad P = \begin{bmatrix}0\\ pn_x\\ pn_y\\ pn_z\\ pU_n\end{bmatrix}$$

Pour l'écoulement subsonique,

$$P_{1\frac{1}{2}} = \frac{1}{2}(P_{1_L} + P_{1_R}) - \frac{1}{2}(D_R - D_L)$$

Pour l'écoulement supersonique, c'est la même chose que le schéma FVS.

Le schéma a été testé pour résoudre les équations d'Euler en une, deux et trois dimensions. Les résultats obtenus sont monotones et les profils de l'onde de choc sont bien définis. Pour les problèmes de tubes à choc unidirectionnel avec une onde de choc et une discontinuité de contact, le présent schéma et celui de Roe, en utilisant la différence finie de premier ordre, donnent des résultats plus satisfaisants que ceux obtenus à partir des schémas de Van Leer et l'AUSM de Liou Steffen. Pour les écoulements transsoniques à plus d'une dimension, on obtient des profils monotones et bien définies des ondes de choc ayant pour la plupart une zone de transition. Un problème est apparu au point sonique quand la différence finie du premier ordre est utilisée sur les diffuseurs. Cependant le problème peut être corriger en utilisant une différence finie d'ordre plus grand. Le schéma converge bien pour tous les cas testés. Cette méthode est légèrement plus vite que le schéma d'AUSM mais plus lent que celui de Van Leer. Généralement, pour les écoulements transsoniques testés, les résultats sont semblables à ceux obtenus des schémas d'AUSM et de Van Leer. Toutefois, en utilisant la différence finie du troisième ordre, le présent schéma produit des résultats avec moins d'oscillation près des chocs. Pour une tuyère transsonique, les résultats calculés à partir du présent schéma concordent bien avec les résultats expérimentaux.

ABSTRACT

The purpose of this thesis is to develop numerical techniques to obtain high efficiency and accuracy for the simulation of three-dimensional transonic flows by using upwind schemes. Two parallel techniques have been developed: 1) An efficient Upwind Relaxation-Sweeping (URS) algorithm has been suggested to calculate the three-dimensional time-dependent full Euler and Navier-Stokes equations. 2) A new Flux Vector Splitting scheme with low diffusion to capture crisp shock waves and contact discontinuities has been suggested.

The Upwind Relaxation-Sweeping algorithm is to implement the relaxation iteration on the vertical streamwise plane and then to sweep alternately in span wise direction. The algorithm can reach very high CFL number due to the unfactored relaxation scheme without the approximation error introduced. The memory requirement is greatly reduced because the matrices are only stored in one iterating plane. The linear stability analysis indicates that the URS algorithm is unconditionally stable. The algorithm is independent of the global sweeping direction selection. However, choosing the direction with relatively low variable gradient as the global sweeping direction results in a higher degree of stability. The algorithm has been applied to analyze the internal flow fields of the transonic non-axisymmetric nozzles, including the throat contouring effect, transition ducts. The computational results agree favourably with the experiments.

The new flux vector splitting scheme uses the velocity component normal to the volume interface as the characteristic speed and yields the vanishing individual

mass flux at the stagnation. The numerical dissipation for mass and momentum equations also vanishes with the Mach number approaching zero. The scheme is very simple and easy to implement. The scheme has been applied to solve 1-D and multidimensional Euler equations. The solutions are monotone and the normal shock wave profiles are crisp. For a 1D shock tube problem with the shock and the contact discontinuities, the present scheme and Roe scheme give very similar results, which are the best compared with those from Van Leer scheme and Liou-Steffen's AUSM scheme. For multidimensional transonic flows, the sharp monotone normal shock wave profiles with mostly one transition zone are obtained. The results are compared with those from Van Leer scheme, AUSM scheme and also with the experiment.

ACKNOWLEDGEMENTS

First of all, I would like to express my greatest gratitude to Professor E. Bilgen, the supervisor for my Ph.D. study, for his support to carry out the research work in this thesis.

I would like also to thank Mr. P. Leroux and Mr. V.S. Pachanh, both undergraduate major, for their calculation of geometrical parameters and some computation of the 3D inviscid flow fields by using the URS algorithm. I shall be grateful to Mr. Fan-Ming Meng too for his carrying out some of the computation for the new Flux Vector Splitting scheme.

I would like to thank very much my wife, Wen-Qing Liu, for her understanding and support. Particularly, at the last stage of my Ph.D. study, we have our lovely first baby. Wen-Qing took care of the baby and most of the house work so that I could have time to complete this thesis.

I would also like to extend my special thanks to the people and friends who gave me help and convenience for my Ph.D. study. Among them, Dr. M.-S. Liou in NASA Lewis Research Center is the one to whom I shall be particularly grateful for providing his research papers from which I benefited a lot. I also greatly appreciate the discussion with him and his encouragement to my work.

FCAR of Quebec gorvement is acknowledged for giving me the scholarship to do a part of this work.

Finally, I would like to sincerely thank the professors in my thesis defence jury for their examination of my Ph.D. thesis.

CONTENTS

	SOMMAIRE	v
	ABSTRACT	xii
	ACKNOWLEDGEMENTS	xiv
	CONTENTS	xv
	LIST OF SYMBOLS	xvii
	FIGURE CAPTIONS	xx
	LIST OF TABLES	xxv
	LIST OF APPENDICES	xxvi
	CHAPTER I INTRODUCTION	**1**
1.1	A Review of Time Marching Techniques	1
1.2	A Review of Upwind Schemes	10
	CHAPTER II GOVERNING EQUATIONS	**18**
2.1	The 3D Euler and Navier-Stokes Equations	18
2.2	The Integral Form of the Governing Equations	20
	CHAPTER III SOME POPULARLY USED UPWIND SCHEMES	**23**
3.1	Roe's Flux Difference Splitting Scheme, 1981	23
3.2	Van Leer's Flux Vector Splitting Scheme, 1982	26
3.3	Liou-Steffen's AUSM Upwind Scheme, 1991	28

CHAPTER IV THE UNFACTORED UPWIND RELAXATION-SWEEPING ALGORITHM **31**

4.1 Description of URS Procedure 31

4.2 Stability Analysis 36

4.3 Boundary Conditions and Time Stepping 42

CHAPTER V THE NEW FLUX VECTOR SPLITTING SCHEME **44**

5.1 Construction of the 1D Form of the New FVS Scheme 44

5.2 Numerical Diffusion of the New FVS Scheme 48

5.3 Three-dimensional Form of the New FVS Scheme 51

CHAPTER VI RESULTS AND DISCUSSION **55**

6.1 Results for URS Algorithm 55

6.1.1 Solutions of 3D Euler Equations 55

6.1.2 Solutions of 3D Navier-Stokes Equations 65

6.2 Results for the New FVS Scheme 70

CONCLUSIONS **77**

REFERENCES **80**

APPENDICES **86**

LIST OF SYMBOLS

a	speed of sound, $a = \sqrt{\gamma RT}$
A	Jacobian Matrix of the inviscid flux normal to a cell interface, a single wave amplitude of the round-off error Furier series
C	convective vector of the new flux vector splitting scheme
D	numerical diffusion vector of the new FVS scheme
e	total energy per unit volume
E	convective flux in Liou-Steffen AUSM scheme
F	inviscid flux vector in x-direction
G	inviscid flux vector in y-direction
g	amplification factor of the round-off error amplitude
H	inviscid flux vector in z-direction, total enthalpy
$\mathbf{i}_x$, $\mathbf{i}_y$, $\mathbf{i}_z$	unit vectors in x, y and z-direction
LHS	Left Hand Side
M	Mach number
$\mathbf{M}_n$	Mach number based on the velocity component normal to a cell interface
n	normal outward pointing unit vector
$\mathbf{n}_x$, $\mathbf{n}_y$, $\mathbf{n}_z$	components of vector **n** in x, y and z-direction
P	pressure vector of the new flux vector splitting scheme
p	pressure of the fluid

$\mathbf{P}_1$	inviscid flux normal to a cell interface
$\mathbf{P}_e$	static pressure at the nozzle (or duct) exit
$\mathbf{P}_t$	total pressure of the coming flow
Pr	Prandtl number
Q	volume of a cell, unit matrix, eigenvector matrix
R	viscous flux vector in x-direction, transformed flux for Van Leer scheme
R'	total interface flux of 3D N.S. equations in integral form
$\mathbf{R}_{inv}$	total inviscid flux
Re	Reynolds number
RHS	Right Hand Side
S	viscous flux vector in y-direction, cell surface area
T	viscous flux vector in z-direction, eigenvector matrix of **A**, local rotation matrix for Van Leer scheme, fluid temperature
U	conservative variable vector
$\mathbf{U}_n$	velocity component normal to the cell interface
$\mathbf{U}^-$	conservative variables to determine the split flux with positive eigenvalues
$\mathbf{U}^+$	conservative variables to determine the split flux with negative eigenvalues
u, v, w	velocity components in x, y and z-direction
x, y, z	Cartesian coordinates

Greek symbols

α	α**=1:** Navier-Stokes equations, α**=0:** Euler equations
ϱ	density of the fluid
μ	dynamic viscosity
λ	bulk viscosity, $=-2\mu/3$
τ	shear stress
Λ	eigenvalue matrix of Jacobian matrix **A**
Δ, ∇	forward and backward difference operator

Subscripts

L, R	left side and right side of a cell interface
n	direction normal to a cell interface
m	mass flux
i, j, k	mesh point index in x, y and z-direction

Superscripts

~	Roe's average
+	split individual flux with positive eigenvalues
-	split individual flux with negative eigenvalues

FIGURE CAPTIONS

Fig. 4. (1) The sketch of the sweeping for the URS algorithm 90

Fig. 4. (2) The wall boundary condition treatment for 3D Navier-Stokes equations 90

Fig. 5. (1) Mass flux of the flux vector splitting schemes 91

Fig. 6.1. (1) The sketch of a transition duct with a nozzle 92

Fig. 6.1. (2) The geometry and the grid of the transition duct 1 with the nozzle, grid size 101x31x31. 93

Fig. 6.1. (3) The convergency histories of the transition duct 1 with the nozzle 94

Fig. 6.1. (4) The Mach number distribution along the center line of the duct and the nozzle 94

Fig. 6.1. (5) Pressure distributions of the duct 1 and the nozzle 95

Fig. 6.1. (6) The velocity fields of the cross sections with no entrance swirl . . 96

Fig. 6.1. (7) The velocity fields of the cross sections with entrance swirl 97

Fig. 6.1. (8) The Mach Number Contours of Transition Duct 1 and the Nozzle 98

Fig. 6.1. (9) The spanwise center plane of the duct 2 with the nozzle 98

Fig. 6.1. (10) Pressure distributions of the duct 2 and the nozzle 99

Fig. 6.1. (11) The grid and the geometry of the transonic nozzle 100

Fig. 6.1. (12) Pressure Contours of a Typical Section of the Nozzle 100

Fig. 6.1. (13) Pressure distributions of the nozzle 101

Fig. 6.1 (14) The convergency History of the Transonic Nozzle 102

Fig. 6.1. (15) The grid and the geometry of the 3D channel, grid; 101x31x31 . 103

Fig. 6.1. (16) The experimental Mach number contours of the channel at different spanwise locations 104

Fig. 6.1. (17) The calculated Mach number contours of the channel on the walls, Pe/Pt=0.545 105

Fig. 6.1. (18) Convergency histories of the channel 106

Fig. 6.1. (19) The calculated Mach number contours of the channel at different spanwise locations, Pe/Pt=0.755 107

Fig. 6.1. (20) The three dimensional grid of the nozzles 108

Fig. 6.1. (21) The sketch of a nozzle geometry 109

Fig. 6.1. (22) The streamwise sections of the five nozzles 110

Fig. 6.1 (23) Pressure distributions of nozzle A1, • Experiment, - Calculation 111

Fig. 6.1. (24) Pressure distributions of nozzle A2, • Experiment, - Calculation 112

Fig. 6.1. (25) Pressure distributions of nozzle B1, • Experiment, - Calculation 113

Fig. 6.1. (26) Pressure distributions of nozzle B2, • Experiment, - Calculation 114

Fig. 6.1. (27) Pressure distributions of nozzle B3, • Experiment, - Calculation 115

Fig. 6.1. (28) Calculated lower wall central-line pressure distributions 116

Fig. 6.1. (29) Calculated lower wall central-line pressure distributions 116

Fig. 6.1. (30) Mach number distributions along the nozzle central lines 117

Fig. 6.1. (31) The dischagre coefficients of the nozzles 117

Fig. 6.1. (32) The thrust ratios of the nozzles 118

Fig. 6.1. (33) Spanwise section velocity fields of Nozzle A1 119

Fig. 6.1. (34) Mach number contours at different sections of Nozzle A1 120

Fig. 6.1. (35) Streamwise section velocity field of Nozzle A1 121

Fig. 6.1. (36) Spanwise section velocity field near the exit of Nozzle B2 . . . 121

Fig. 6.1. (37) Convergence Histories of Nozzle A2 122

Fig. 6.2. (1) 1D Shock tube results calculated by using the present scheme, grid size: 201, Temperature and Pressure 123

Fig. 6.2. (2) 1D Shock tube results calculated by using the present scheme, grid size: 201, Density and Velocity 124

Fig. 6.2. (3) 1D Shock tube results calculated by using Roe scheme, grid size: 201, Temperature and Pressure 125

Fig. 6.2. (4) 1D Shock tube results calculated by using Roe scheme, grid size: 201, Density and Velocity 126

Fig. 6.2. (5) 1D Shock tube results calculated by using Van Leer scheme, grid size: 201, Temperature and Pressure 127

Fig. 6.2. (6) 1D Shock tube results calculated by using Van Leer scheme, grid size: 201, Density and Velocity 128

Fig. 6.2. (7) 1D Shock tube results calculated by using Van Leer scheme, grid size: 201, Temperature and Pressure 129

Fig. 6.2. (8) 1D Shock tube results calculated by using Van Leer scheme, grid size: 201, Density and Velocity 130

Fig. 6.2. (9) 1D Shock tube results calculated by using AUSM scheme, grid size: 201, Temperature and Pressure 131

Fig. 6.2. (10) 1D Shock tube results calculated by using AUSM scheme, grid size: 201, Density and Velocity 132

Fig. 6.2. (11) 2D Grid of the Inlet-Diffuser, 101 x 31 133

Fig. 6.2. (12) Mach number distributions along the walls of the inlet-diffuser with grid 101 x 31 134

Fig. 6.2. (13) The pressure contours of the inlet-diffuser calculated by using the first order differencing with grid 101 x 31 135

Fig. 6.2. (14) Mach number distributions along the walls of the inlet-diffuser with grid 101 x 31 136

Fig. 6.2. (15) The pressure contours of the inlet-diffuser calculated by using the second order differencing with grid 101 x 31 137

Fig. 6.2. (16) 3D Grid of the Inlet-Diffuser with grid 101 x 31 x 31. To see the geometry, the bottom of the diffuser is shown at the top 138

Fig. 6.2. (17) Mach number distributions along the walls of the inlet-diffuser with grid 101 x 31 139

Fig. 6.2. (18) The Mach number contours of the inlet-diffuser calculated by using the third order differencing with 101 x 31 x 31 140

Fig. 6.2. (19) Convergence histories of the 3D inlet-diffuser by using the third order differencing 141

Fig. 6.2. (20) Convergence history of the 2D inlet-diffuser by using the present scheme with grid 101 x 31 142

Fig. 6.2. (21) 3D grid of the transonic nozzle with grid 101 x 31 x 31. 143

Fig. 6.2. (22) Mach number distributions along the bottom wall center line of the transonic nozzle with grid 101 x 31 x 31 144

Fig. 6.2. (23) The Mach number contours of the transonic nozzle calculated by using the third order differencing with grid 101 x 31 x 31 145

Fig. 6.2. (24) Pressure distributions of the transonic nozzle at four locations in spanwise directions 146

Fig. 6.2. (25) Convergence histories of the transonic nozzle with grid 101 x 31 x 31 147

LIST OF TABLES

Table 1: Geometric parameters for the transition ducts 57

Table 2: The design geometry parameters for the five nozzles 66

LIST OF APPENDICES

APPENDIX A NONDIMENSIONAL VARIABLES 86

APPENDIX B METHOD OF CALCULATING CIRCULAR-TO-RECTANGULAR TRANSITION SURFACES 88

CHAPTER I INTRODUCTION

1.1 A Review of the Time-Marching Techniques

The time dependent Euler and Navier-Stokes equations are the complete governing equations for the inviscid and viscous compressible flows respectively. The techniques typically used for the solution of the Euler and Navier-Stokes equations are the same, even though there are some major differences in the behaviour of the technique with and without the viscous terms. The time derivatives in the Euler/Navier-Stokes equations are retained, thus making the equations hyperbolic in nature. For the steady state problems, the solutions march in the temporal direction from guessed initial fields and reach the steady solutions when they converge under the steady boundary conditions. The advantage of solving the time dependent equations is that the same code/algorithm is used for the solution of all flow regimes, low subsonic to hypersonic. The computer CPU time required to reach the specified time level or the converged solutions stands for the efficiency of a numerical method.

There are two classes of methods of solving the time-dependent hyperbolic equations: explicit and implicit. Explicit methods, where spatial derivatives are evaluated using the known conditions at the old time level, are simpler and more easily vectorizable. The implementation of the boundary conditions is easier. The

coding can be easily extended to include time-accurate solution. Their major disadvantages lie in the conditional stability dictated by a CFL limit, in which the numerical domain of dependence must contain the physical domain of dependence for hyperbolic equation. For 1D Euler equations, the CFL number can be expressed as: $CFL = \Delta X / [(|u| + a) \bullet \Delta t]$. Unless the interest lies only in the steady-state solution, the convergence is usually slower and requires more computational time than an implicit method. Implementation of multi-grid and vector processing improves convergence and lowers computational time. The widely used explicit methods are as follows:

1) The Lax-Wendroff scheme (Lax & Wendroff 1960 & 1964) is second-order accurate in time and space. This scheme has the advantage of simplicity and robustness and the flow variables need to be stored only at a single time level.

2) The predictor-corrector method due to MacCormack in 1969 (MacCormack 1969) is a modified version of the Lax-Wendroff scheme. It is also second-order accurate in time and space and involves a two-step procedure. Hence, the variables have to be stored in two steps. The method is less complex than the Lax-Wendroff technique. The CFL limit is one for both these schemes (CFL <1).

3) The Runge-Kutta type schemes first suggested by Jameson et al. in 1981 (Jameson & Schmidt & Turkel 1981) have found wide application in both internal

and external flows. The four-stage scheme permits a maximum CFL number of $2\sqrt{2}$ and is a considerable improvement over the two methods listed above. This technique is likely to be employed widely for both the time-accurate (unsteady) and the steady-state solutions.

The advantage and disadvantage of the explicit versus implicit technique depend on the computational efficiency, i.e., the computer time required to achieve a converged and accurate solution. Outside the viscous region, viscous diffusion is not significant, and grid spacings (Δx, Δy) are chosen to resolve only the convection and pressure terms, and moderate time steps can be taken. Inside the viscous layer and near the solid surface, diffusion terms dominate and the fine resolution of the viscous layer may only be resolved with a fine mesh, and small time steps are required in this region. This is one of the major drawbacks of the explicit methods, which requires small time steps to resolve the viscous layer as well as the inviscid shock layers. In earlier computations, a constant time step was used in the entire region, but this is not necessary. If the interest lies only in steady state solution, the scheme can be accelerated by using the time step consistent with the local CFL number for each grid point. Hence the time step can be chosen to vary to keep the CFL number constant over the grid. This procedure is called "variable time step" or "local time step" and significantly increases the convergence rate on highly stretched grids.

The time step limitation of the explicit scheme led to widespread use of implicit techniques which can be unconditionally stable for all time steps. One of the most widely used implicit techniques is the Approximate Factorization method (AF-ADI) suggested by Briley and McDonald in 1976 and Beam and Warming in 1978 (Briley & McDonald 1976, Beam & Warming 1978). Linear stability analysis provide that the schemes are unconditionally stable in two dimensions. Operational CFL numbers in the order of 10 appear to provide the best error damping properties. There is no CFL limit, even though there are some constraints on the time step. As in the explicit techniques, both finite-volume and finite-difference formulations are employed. The major computational effort is expended in inverting the block tri-diagonal matrix system that arises. Pulliam (Pulliam 1986) made some improvements including diagonalization of the blocks in implicit operators, pressure velocity split, grid refinement, improved boundary conditions, variable time step, and multi-gridding. The linear stability analysis indicated that the 3D AF scheme is unstable. Even so, the AF scheme is still widely used for 3D calculation of the nonlinear compressible flow governing equations with the artificial dissipation added to suppress the oscillations. But the stability restriction is more severe in three dimensions and makes it only have the order of CFL number as in explicit schemes. After the beginning of 1980's with the appearance of the flux vector splitting concept, the two-factor scheme based on an lower-upper (LU) factorization proposed by Steger-

Warming (Steger & Warming 1981) and Jameson-Turkel (Jameson & Turkel 1981) became popular as an alternative to the ADI method to solve the 3D flow fields. Even though the LU factorization method is stable, the time step is still limited due to the factorization error. Rai and Chakravarthy (Rai and Chakravarthy 1986) suggested a Newton sub-iteration technique to drive the factorization error to zero at each time step, which makes the LU factorization method have larger time step than the noniterative scheme. This idea was successfully applied to 3D viscous flow fields by Simpson and Whitfield (Simpson & Whitfield 1992). However, the iterative approach needs extra computation which is offset to some extent by the larger time step sizes. Edwards and McRae (Edwards & McRae 1993) developed their nonlinear relaxation solver for 3D viscous flows with the mixture of upwind and central differencing. The method is shown to be efficient, but it is still related to the LU factorization.

Generally, as an implicit scheme, Approximation Factorization method is successfully used to carry out the simulation of different kinds of flow fields. However, the factorization scheme has to introduce an error which is proportional to Δt^3 or Δt^2 and therefore restricts large time steps to be used.

With the appearance of upwind scheme for compressible flow in the early 1980's (Steger & Warming 1981, Roe 1981, Van Leer 1982), a class of efficient

implicit unfactored algorithms were obtained. Chakravarthy in 1984 (Chakravarthy 1984) first suggested the unfactored implicit relaxation method based on using the upwind scheme for the time marching problems. It made a great progress to reach an unconditionally stable condition of the implicit scheme. The time step restraint on AF scheme is broken because the relaxation algorithm does not need the factoratization error. The time step is therefore substantially greater than that of AF-ADI scheme. For the 2D cases reported using Gauss-Seidel iteration (Thomas & Walters 1985, Zha & Liu & Ma 1989, MacCormack 1985), the CFL number reached the order of 10^5. Therefore very rapid convergency rate has been reached. The order of iteration number to get the converged solution can be less than 100 or just 10 for the Newton iteration method which possesses the quadratic convergence rate and is faster than the Gauss-Seidel iteration. This was a great progress. However, the encouraging achievements have been mainly limited to 2D problems. For three dimensional calculations, the achievements are not so impressive. The excessive memory requirement of large quantity of the matrices to be stored hinders the application of the unfactored upwind implicit scheme. Even with the present supercomputer with large memory resources, the application of direct solver to 3D problems in general are not possible (Van Dam & Hafez 1989). Thomas, Vatsa and Nagasu applied upwind schemes to 3D problems by different numerical schemes (Thomas & Van Leer Walters 1990, Vatas & Thomas & Wedan 1987, Thomas &

Walters 1990, Nagasu 1990). But the algorithms are still mainly limited to the approximation factorization method. The advantage of the AF scheme is that it can be completely vectorizable. But it loses the high convergence rate. Hänel and Schwane extended the line Gauss-Seidel iteration to 3D hypersonic calculation (Hänel & Schwane 1987, 1989). The algorithm was mentioned to be efficient with no quantitative proof. But the storage requirement was excessively large. Candler and MacCormack extended MacCormack's 1984 implicit unfactored algorithm to 3D and solved 3D hypersonic flow fields using the Gauss-Seidel line relaxation with alternating sweeps (Candler & MacCormack 1987). MacCormack modified the algorithm by implementing the block tri-diagonal inversions in two directions with Gauss-Seidel relaxation in the third direction to improve the robustness (MacCormack 1990). The rapid convergency rate has been obtained by both the algorithms. One disadvantage for these algorithms is the large computational work per time step, not because of the vectorization difficulty, which is shown to be achievable by McMaster et al. (McMaster & Shang & Gaitonde 1989), but mainly because the Gauss-Seidel iteration for the fully implicit discretization usually needs more than one sweep, often two, in the sweeping direction. Otherwise the "iteration" or " relaxation" may not be built up and the linearization error may not be driven down enough before the time marches to next time step. Only in the cases of supersonic flows, one forward sweep in streamwise direction may be enough. It is

noted that two sweeps for sub- or tran-sonic flows in the global field with one or two block tridiagonal matrix inversions at the local planes are usually CPU time intensive. A different unfactored 3D algorithm is developed by Paoletti et al. using the conjugate gradient squared (CGS) iterative algorithm with ADI as a preconditioner (Paoletti & Vitaletti & Stow 1992). The algorithm is therefore called CGS-ADI. This algorithm uses the spatial central differencing and the artificial dissipation has to be added. An efficient ADI pre-conditioner is necessary for CGS-ADI. Otherwise a large number of CGS iterations may be required for each time step and it would offset the advantages of large time step .

More efforts are needed to develop robust unfactored 3D algorithms for they have theoretically potentials to obtain rapid convergency rate and save CPU time.

In this thesis, a three-dimensional unfactored Upwind Relaxation-Sweeping (URS) algorithm has been developed to aim at keeping the high convergency rate and reducing the memory requirement. URS method is to apply the relaxation algorithm on the vertical streamwise plane and then sweep plane by plane in spanwise direction. Making use of the advantages of the upwind scheme, the algorithm is 11/12 implicit. The 1/12 explicit flux is in the spanwise direction. The advantages of URS scheme are: 1) No approximate factorization error is introduced and therefore the relaxation algorithm can have very large time step. 2) The residual

R, the Jacobians and the δU^{n+1} which take up most of the memory resources are stored only in one iterating-plane like the two dimensions; hence the total memory requirement is greatly reduced. In addition, it only requires one sweep in the global field and therefore the CPU time per time step is saved. The linear stability analysis indicates that the URS algorithm is unconditionally stable. Choosing the direction with relatively low variable gradient as the global sweeping direction will hold higher degree of stability. For the cases tested for 3D Euler and Navier-Stokes equations, the algorithm was proved to be efficient and robust (Zha & Bilgen 1992, Zha & Bilgen 1993, 1994).

1.2 A Review of the Upwind Schemes

Upwind schemes aim at discretizing the hyperbolic governing equations in conservative form in the direction of the information travel to capture the discontinuities based on the characteristic theory. The equations of conservation in integral form are valid for all flows, including the ones with finite jumps such as shock wave and contact discontinuities. The upwind schemes based on the non-conservative governing differential equations, such as Moretti's λ-scheme (Moretti 1987), will not be discussed in this thesis.

In finite volume codes for the Euler and Navier-Stokes equations, a central place is taken by the algorithm that accounts for the inviscid interaction of adjacent fluid cells at their interface. Such an algorithm combines two distinct sets of state quantities, representing the states on both sides of the interface, into one set of fluxes normal to the interface. Physically speaking there is only one correct value for the flux vector. To find it we must solve the Riemann problem governed by the one-dimensional inviscid flow equations

$$u_t + f(u)_x = 0$$

(x measuring distance to the interface) for the initial values

$$u = \begin{cases} u_L & x<0 \\ u_R & x>0 \end{cases}$$

where u_L and u_R are the left and right interface states. The idea of solving a Riemann problem at every mesh interval and at every step is due to Godunov (Godunov 1959). From a numerical point of view, it seems wasteful to exactly solve the Riemann problem at every interface. All the upwind schemes developed later are aimed at solving the approximate solution, tuned to the overall accuracy of the discretization.

The differencing schemes used in the 1960-1970's were mainly based on the central differencing. It evaluates the interface flux as:

$$f(u_L, u_R) = 1/2 \{ f(u_L) + f(u_R) \}$$

This scheme is inherently unstable and needs adding the artificial dissipation to suppress the oscillation near a shock. Artificial dissipation is some even derivatives of the variables with the forms similar to the real dissipation. Their accuracy order is usually equal to or higher than the magnitude order of the differencing truncation errors. Different researchers may use different forms of artificial dissipations. The one suggested by Jameson, Schmidt and Turkel (1981) is widely used. Adding the artificial dissipation could be a difficult job according to different differencing scheme and even different physical problems. Usually the shocks captured by using central differencing schemes will be smeared to several grid zone width. However, since such schemes do not have the numerical dissipation, they are usually good at the accuracy for the boundary layer resolution.

The characteristic-based upwind schemes blossomed in the late 1970s and usually are classified into two groups, **Flux Vector Splitting** (FVS) schemes and **Flux Difference Splitting** (FDS) schemes. All the upwind schemes inherently possess numerical dissipations to suppress the oscillations near a shock, and therefore, no artificial dissipation is needed. The numerical dissipation discussed in Section 5.2 is an example. This makes the computation of the flow fields more independent of the human factors. However, the numerical dissipations may also distort the real dissipation if the former is too large, which has been a hot issue for these years.

Steger and Warming pioneered the flux vector splitting scheme in 1979 (Steger & Warming 1981). They split the flux vectors into subvectors whose associated eigenvalues are of the same sign, which allows use of one-side (upwind) operators according to the information travel direction. But the numerical dissipation of this scheme is too large and does not vanish in any discontinuities, such as shock waves and contact surfaces. The discontinuities will be smeared out and the viscous solutions will be distorted. The scheme is not continuously differentiable at the eigenvalue sign changes, such as at the sonic and the stagnation point, which may yield a glitch at that points. In 1982, Van Leer suggested another flux vector splitting scheme (Van Leer 1982). Van Leer's scheme has an eigenvalue equal to zero in the subsonic region and leads to a crisp shock profile with at most two transition zones which is sharper than that of the Steger-Warming scheme. Van Leer's scheme is also better than Steger-

Warming scheme at the smooth eigenvalue sign changes and the faster convergence rate due to larger allowable CFL number used (Anderson & Thomas & Roe & Newsome 1987). The MUSCL-type differencing suggested by Van Leer can also cure the non-smoothness of Steger-Warming's scheme at the eigenvalue sign changes (Anderson & Thomas & Roe & Newsome 1987). Generally, Van Leer's scheme can obtain very good representations of the inviscid flow fields. However, Van Leer scheme has the same problem for large numerical dissipations as that of Steger-Warming's scheme. The accuracy of the boundary layer resolution will be influenced by the too large numerical dissipation. The flux difference splitting scheme suggested by Roe (Roe 1981) overcomes the drawbacks of the flux vector splitting schemes. Roe created a special parameter average technique for the matrix of the numerical dissipation vectors. If an eigenvalue of the Jacobian matrix vanishes, the corresponding eigenvalue of the dissipation matrix vanishes too. This leads to a crisp representation -- with at most one interior state-- of steady shocks and contact discontinuities, if aligned with an interface. Van Leer et al. (Van Leer & Thomas & Roe & Newsome 1987) made a significant comparison in 1987 for the available differencing schemes to study the accuracy of each scheme for the viscous flows. They tested a hypersonic flow over a cone with a cone angle of 10^0 and compared the results with the analytical solution. They concluded that Roe's scheme is the most accurate scheme for both shock and boundary layer resolution; Van Leer scheme is

good at shocks but broaden the boundary layer due to the large dissipation; Steger-Wrming's scheme is even worse at both shock and contact discontinuities; MacCormack's scheme based on the central differencing is accurate for the viscous flows, but the shock is wider than those obtained by Roe and Van Leer scheme. For higher order differencing, the accuracy of Van Leer scheme is recovered.

Even though Roe's scheme is accurate, it has some drawbacks. Roe's scheme does not satisfy the entropy low and may admit the nonphysical solutions, such as expansion shock waves (Harten & Lax & Van Leer 1983). With the applications of Roe's scheme, the shortcoming of its robustness has been revelled. The typical problem is the supersonic blunt body flow for which Roe's scheme gives non-physical solutions (Liou & Steffen 1991, Bergamini & Cinnella 1993). The flow field structure of the problem calculated by Roe's scheme changes with the density of the grid and the scheme fails to converge when the Mach number is high. The other shortcoming of Roe's scheme is its setup cost which requires $O(n^2)$ operations per grid point in each iteration due to the dissipation matrix operation in its formulation, where n is the number of equations. Thus a heavy price is paid for the accuracy obtained. Efforts for reducing the computational cost has been pursued and the modification is called the "Harten-Lax/Roe Flux" (Harten & Lax 1981, Roe 1984). Unfortunately, the scheme suffers from a stability problem in which the residual of the L_2 norm is difficult to be driven down (Coirier & Van Leer 1991).

Compared with the Roe's flux difference splitting scheme, the flux vector splitting schemes are remarkably simple without the matrix operation. From the numerical efficiency point of view, the flux vector splitting schemes are superior to FDS, particularly for Van Leer's scheme which can obtain very rapid convergency rate (Thomas & Walters 1985, 1987, Zha & Liu & Ma 1989, Hänel & Schwane 1989, Zha & Liu 1990, Zha & Bilgen 1992). Efforts to develop and modify FVS are necessary because of three reasons: 1. The formulations are relatively simple. 2. The split fluxes are easy to linearize, for the benefit of implicit marching schemes. 3. The extension to real gases is relatively straightforward.

The reason that the flux vector splitting schemes do not give the accurate results for viscous flows is that the individual mass flux of the sub-vectors does not vanish with the velocity approaching zero (Coirier & Van Leer 1991). Therefore, to make the mass flux vanish becomes a direction to improve the accuracy of the flux vector splitting schemes. The High Order Polynomial Expansions (HOPE) scheme of Liou and Steffen (Liou & Steffen 1991) and the Low Diffusion FVS of Van Leer (Coirier & Van Leer 1991) aimed at building up the pure FVS schemes with vanishing mass diffusion. They did achieve the required split mass flux. But the instability and non-monotonicity of the schemes are not acceptable for practical calculations. Efforts have been also attempted to improve the original Van Leer scheme by using some techniques borrowed from flux-difference splitting. First

suggested by Hänel and then extended by Van Leer (Hänel & Schwane 1989, Coirier & Van Leer 1991), the "Van Leer/Hänel 90" scheme using the net mass flux and one side velocity and total enthalpy for the transverse momentum and energy equations obtained an accurate temperature profile for the supersonic conical viscous flow. However, a pressure glitch is accompanied with that scheme (Van Leer 1990). A successful and promising scheme was suggested by Liou and Steffen for their Advection Upstream Splitting Method (AUSM) (Liou & Steffen 1991). They introduced an advective Mach number by combining the split-Mach number contributions from original Van Leer mass splitting. The AUSM scheme is remarkably simple and yields vanishing numerical diffusivity at the stagnation. In a variety of 2D Euler and Navier-Stokes calculations presented in (Liou & Steffen 1991), the scheme was as accurate and convergency as good as Roe's splitting scheme, which was considered as the most accurate by then. AUSM scheme does not need the matrix operation required by Roe scheme and only possesses O(n) operations per grid point instead of $O(n^2)$ for Roe's scheme. Furthermore, AUSM scheme performed very well for a 2D supersonic flow over a circular blunt body for which Roe scheme gave anomalous solutions. However, the AUSM scheme also has its imperfectness. The scheme tends to oscillate for some solutions of the inviscid and viscous flows (Bergamini & Cinnella 1993). It may be because AUSM scheme recovers to central differencing at the stagnation and the instability caused by the

central differencing may spread near the stagnation. Therefore, the efforts to develop the new upwind schemes merit attention.

In this thesis, a new flux vector splitting scheme is suggested to aim at obtaining the vanishing individual split mass flux with the Mach number reaching zero and keeping the advantages of the FVS, such as being able to capture the crisp shock profile, the simplicity and the efficiency (Zha & Bilgen 1993). The interface flux is divided into two parts according to the eigenvalues, the convective vector and pressure vector. The elements of the vectors are even simpler than AUSM scheme. The eigenvalues of the convective terms, the velocity component normal to the volume interface, are used as the characteristic speeds to attain the goal. The form of the formulations is natural and therefore the simplest. It works soundly to capture the crisp monotone shock wave. Moreover, the present scheme leads to the vanishing numerical dissipation at the stagnation for the mass and momentum equations. Even though one of the diffusive terms of the energy equation does not vanish, the numerical diffusion is within the magnitude order of truncation error and the small diffusion may be further ensured by using higher order differencing.

CHAPTER II GOVERNING EQUATIONS

2.1 The 3D Euler and Navier-Stokes Equations

The 3D time-dependent, conservation of mass, Navier-Stokes and energy equations are the governing equations solved numerically in this thesis. The nondimensional equations for compressible ideal gas in the absence of external forces, in conservation law form and in Cartesian coordinates are given below

$$\frac{\partial U}{\partial t}+\frac{\partial F}{\partial x}+\frac{\partial G}{\partial y}+\frac{\partial H}{\partial z}=\alpha\frac{1}{Re}[\frac{\partial R}{\partial x}+\frac{\partial S}{\partial y}+\frac{\partial T}{\partial z}] \tag{1}$$

where

$$U=\begin{bmatrix}\rho\\ \rho u\\ \rho v\\ \rho w\\ e\end{bmatrix}\quad F=\begin{bmatrix}\rho u\\ p+\rho u^2\\ \rho uv\\ \rho uw\\ (e+p)u\end{bmatrix}\quad G=\begin{bmatrix}\rho v\\ \rho uv\\ p+\rho v^2\\ \rho vw\\ (e+p)v\end{bmatrix}\quad H=\begin{bmatrix}\rho w\\ \rho uw\\ \rho vw\\ p+\rho w^2\\ (e+p)w\end{bmatrix} \tag{2}$$

$$R=\begin{bmatrix}0\\ \tau_{xx}\\ \tau_{xy}\\ \tau_{xz}\\ R_5\end{bmatrix}\quad S=\begin{bmatrix}0\\ \tau_{xy}\\ \tau_{yy}\\ \tau_{yz}\\ S_5\end{bmatrix}\quad T=\begin{bmatrix}0\\ \tau_{xz}\\ \tau_{yz}\\ \tau_{zz}\\ T_5\end{bmatrix} \tag{3}$$

$$\tau_{xx}=2/3\mu(2\frac{\partial u}{\partial x}-\frac{\partial v}{\partial y}-\frac{\partial w}{\partial z}) \tag{4}$$

$$\tau_{yy}=2/3\mu(2\frac{\partial v}{\partial y}-\frac{\partial u}{\partial x}-\frac{\partial w}{\partial z}) \tag{5}$$

$$\tau_{zz}=2/3\mu(2\frac{\partial w}{\partial z}-\frac{\partial u}{\partial x}-\frac{\partial v}{\partial y}) \tag{6}$$

$$\tau_{xy}=\tau_{yx}=\mu(\frac{\partial u}{\partial y}+\frac{\partial v}{\partial x}) \tag{7}$$

$$\tau_{xz}=\tau_{zx}=\mu(\frac{\partial w}{\partial x}+\frac{\partial u}{\partial z}) \tag{8}$$

$$\tau_{yz}=\tau_{zy}=\mu(\frac{\partial v}{\partial z}+\frac{\partial w}{\partial y}) \tag{9}$$

$$R_5=u\tau_{xx}+v\tau_{xy}+w\tau_{xz}+\frac{\mu}{(\gamma-1)Pr}\frac{\partial a^2}{\partial x} \tag{10}$$

$$S_5=u\tau_{xy}+v\tau_{yy}+w\tau_{yz}+\frac{\mu}{(\gamma-1)Pr}\frac{\partial a^2}{\partial y} \tag{11}$$

$$T_5 = u\tau_{xz} + v\tau_{yz} + w\tau_{zz} + \frac{\mu}{(\gamma-1)Pr}\frac{\partial a^2}{\partial z} \tag{12}$$

When α is 0, Eq. (1) is the Euler equations for the inviscid flow, and when α is 1, Eq. (1) is the Navier-Stokes equations. The velocities are u, v, w, and e is the total energy per unit volume. The molecular viscosity μ is determined by the Sutherland law and Stokes hypothesis is used for the bulk viscosity $\lambda = -2\mu/3$. The Reynolds and Prandtl numbers are denoted as Re and Pr. Finally, the pressure p is determined by the ideal-gas law

$$p = (\gamma-1)[\, e - \rho(u^2 + v^2 + w^2)/2 \,] \tag{13}$$

where γ is the ratio of specific heats, taken as $\gamma = 1.4$.

The detailed nondimensional variables are given in Appendix A.

2.2 The Integral Form of the Governing Equations

To discretize the equations using finite volume method, the equations should be written in the integral form. Let

$$R' = (F - \frac{\alpha}{Re}R)\cdot i_x + (G - \frac{\alpha}{Re}S)\cdot i_y + (H - \frac{\alpha}{Re}T)\cdot i_z \tag{14}$$

Using the Gauss theorem, the integral form of Eq. (1) is

$$\int_Q \frac{\partial U}{\partial t} dQ + \int_S R' \cdot n dS = 0 \tag{15}$$

where Q is the volume bounded by the surface S and n is the outward pointing unit vector normal to the surface expressed as:

$$n = n_x i_x + n_y i_y + n_z i_z \tag{16}$$

The equations are discretized in the physical domain on the arbitrary body-fitted grid. The flux crossing an interface of two adjacent cells is the normal component of vector R' given in Eq. (14). Let P_1 be the inviscid normal component of R_{inv} passing through unit interface.

where

$$R_{inv} = F i_x + G i_y + H i_z \tag{17}$$

Thus

$$P_1 = R_{inv} \cdot n = F n_x + G n_y + H n_z$$

$$= U_n \begin{bmatrix} \rho \\ \rho u \\ \rho v \\ \rho w \\ e \end{bmatrix} + \begin{bmatrix} 0 \\ pn_x \\ pn_y \\ pn_z \\ pU_n \end{bmatrix} \tag{18}$$

where $\mathbf{U_n}$ is the normal component of the velocity expressed as:

$$U_n = un_x + vn_y + wn_z \tag{19}$$

Upwind schemes will be used to evaluate $\mathbf{P_1}$ at the volume interface.

CHAPTER III SOME POPULARLY USED UPWIND SCHEMES

In this chapter, three upwind schemes widely used are described. It includes the Roe scheme, Van Leer scheme and Liou-Steffen's AUSM scheme. All these schemes are applied to evaluate the inviscid interface flux of a control volume in this thesis. To be general, only the three-dimensional forms of the schemes are presented.

3.1 Roe's Flux Difference Scheme, 1981

Roe proposed his scheme in 1D form (Roe 1981). The inviscid flux P_1 in 3D form given in Eq. (18) may be evaluated as the following:

The interface flux can be written as the exact solution to an approximate Riemann problem

$$P_{1_{i+\frac{1}{2}}} = \frac{1}{2}\{ P_1(U_L) + P_1(U_R) - |\tilde{A}| \, (U_R - U_L) \}_{i+\frac{1}{2}} \tag{20}$$

where U_L and U_R are the state variables to the left and right of the cell interface and

$$A = \frac{\partial P_1}{\partial U} = T\Lambda T^{-1} \tag{21}$$

$$|A| = T|\Lambda|T^{-1} \tag{22}$$

The diagonal matrix Λ is the matrix of eigenvalues of A containing the eigenvalues $[\, U_n - a,\ U_n + a,\ U_n,\ U_n,\ U_n \,]$; and $\mathbf{T}, \mathbf{T}^{-1}$ are diagonalizing matrices, all evaluated at Roe-averaged values such that

$$P_1(U_R) - P_1(U_L) = \tilde{A}[U_R - U_L] \tag{23}$$

is satisfied exactly. The diagonalizing matrix T is formed by the right eigenvectors of the matrix A,

$$T = (T_1\ ,\ T_2\ ,\ T_3\ ,\ T_4\ ,\ T_5) \tag{24}$$

The expression of these eigenvectors given by Liou and Hsu (Liou & Hsu 1989) is:

$$T_1 = \begin{bmatrix} 1 \\ u - an_x \\ v - an_y \\ w - an_z \\ H - aU_n \end{bmatrix} \qquad T_2 = \begin{bmatrix} 1 \\ u + an_x \\ v + an_y \\ w + an_z \\ H + aU_n \end{bmatrix} \qquad T_3 = \begin{bmatrix} n_x \\ un_x \\ vn_x + \rho n_z \\ wn_x - \rho n_y \\ kn_x + \rho(vn_z - wn_y) \end{bmatrix} \tag{25.1}$$

$$T_4 = \begin{bmatrix} n_y \\ un_y - \rho n_z \\ vn_y \\ wn_y + \rho n_x \\ kn_y + \rho(wn_x - un_z) \end{bmatrix} \qquad T_5 = \begin{bmatrix} n_z \\ un_z + \rho n_y \\ vn_z - \rho n_x \\ wn_z \\ kn_z + \rho(un_y - vn_x) \end{bmatrix} \tag{25.2}$$

where the kinetic energy $\mathbf{k} = (\mathbf{u}^2 + \mathbf{v}^2 + \mathbf{w}^2)/2$.

To obtain the dissipation matrix $\tilde{A}$, all the variables substituted into Eq. (21) should be evaluated by using the Roe's average technique. That is:

$$\tilde{\rho} = \sqrt{\rho_R \, \rho_L} \tag{26}$$

$$\tilde{u} = (u_L + u_R\sqrt{\rho_R / \rho_L})/(1 + \sqrt{\rho_R / \rho_L}) \tag{27}$$

$$\tilde{v} = (v_L + v_R\sqrt{\rho_R / \rho_L})/(1 + \sqrt{\rho_R / \rho_L}) \tag{28}$$

$$\tilde{w} = (w_L + w_R\sqrt{\rho_R / \rho_L})/(1 + \sqrt{\rho_R / \rho_L}) \tag{29}$$

$$\tilde{H} = (H_L + H_R\sqrt{\rho_R / \rho_L})/(1 + \sqrt{\rho_R / \rho_L}) \tag{30}$$

$$\tilde{a}^2 = (\gamma - 1)[\tilde{H} - (\tilde{u}^2 + \tilde{v}^2 + \tilde{w}^2)/2] \tag{31}$$

3.2 Van Leer's Flux Vector Splitting Scheme, 1982

The splitting of Van Leer was originally developed for Cartesian coordinates (Van Leer 1982). For supersonic flow, $|M_x| > 1$,

$$F^+ = F, \quad F^- = 0, \qquad M_x > 1, \tag{32}$$

$$F^- = F, \quad F^+ = 0, \qquad M_x < -1, \tag{33}$$

and for subsonic flow, $|M_x| < 1$,

$$F_m^{\pm} = \begin{bmatrix} f_m^{\pm} \\ f_m^{\pm} \cdot \dfrac{(\gamma-1)u \pm 2a}{\gamma} \\ f_m^{\pm} \cdot v \\ f_m^{\pm} \cdot w \\ f_m^{\pm} \cdot \left\{ \dfrac{[(\gamma-1)u \pm 2a]^2}{2(\gamma^2-1)} + \dfrac{1}{2}(v^2+w^2) \right\} \end{bmatrix} \tag{34}$$

where

$$f_m^{\pm} = \pm\rho a[\frac{1}{2}(M_x \pm 1)]^2 \tag{35}$$

a is the local sound speed and M_x is the local Mach number based on u.

To split $\mathbf{P}_1$ in a general 3D form given in Eq. (18), $\mathbf{P}_1$ is first transformed into $\mathbf{R}$ by a local rotation matrix $\mathbf{T}$

$$T = \begin{bmatrix} 1 & 0 & 0 & 0 & 0 \\ 0 & n_x & n_y & n_z & 0 \\ 0 & -\frac{n_y}{r'} & \frac{n_x}{r'} & 0 & 0 \\ 0 & \frac{n_x n_y}{r'} & \frac{n_y n_z}{r'} & -r' & 0 \\ 0 & 0 & 0 & 0 & 1 \end{bmatrix} \tag{36}$$

$$R = T \cdot P_1 = \begin{bmatrix} \rho U_n \\ p+\rho U_n^2 \\ \rho U_n V \\ \rho U_n W \\ (e+p)U_n \end{bmatrix} \tag{37}$$

where

$$r' = \sqrt{n_x^2 + n_y^2} \tag{38}$$

$$V = -\frac{un_y}{r'} + \frac{vn_x}{r'} \tag{39}$$

$$W = \frac{un_x n_z}{r'} + \frac{vn_y n_z}{r'} - wr' \tag{40}$$

The transformed flux **R** is of the same form as the Cartesian flux vector and thus can be split using Van Leer's splitting.

$$R = R^+ + R^- \tag{41}$$

Then

$$P_1 = T^{-1} \cdot R = T^{-1} \cdot (R^+ + R^-) = P_1^+ + P_1^- \tag{42}$$

Thus the splitting formulation for the interface flux has been obtained.

3.3 Liou-Steffen's AUSM Upwind Scheme, 1991

Liou-Steffen's AUSM scheme has a very simple expression. Extension of this scheme from 1D to 3D is straightforward and no transformation is needed. For the supersonic flow, it is the same as the Van Leer scheme (or standard upwind scheme) given by Eq.32 and 33. For subsonic flow, AUSM scheme is as the following:

The interface flux $\mathbf{P}_1$ given in Eq. (18) can be written as

$$P_1 = U_n \begin{bmatrix} \rho \\ \rho u \\ \rho v \\ \rho w \\ \rho H \end{bmatrix} + \begin{bmatrix} 0 \\ pn_x \\ pn_y \\ pn_z \\ 0 \end{bmatrix} = M_n \begin{bmatrix} \rho a \\ \rho ua \\ \rho va \\ \rho wa \\ \rho Ha \end{bmatrix} + \begin{bmatrix} 0 \\ pn_x \\ pn_y \\ pn_z \\ 0 \end{bmatrix} \tag{43}$$

where the **H** is the enthalpy expressed as $H = (e + p)/\rho$.

For subsonic flow, the flux at the interface is given as follows:

Let

$$E = \begin{bmatrix} \rho a \\ \rho ua \\ \rho va \\ \rho wa \\ \rho Ha \end{bmatrix} \tag{44}$$

$$P_{1\frac{1}{2}} = M_{n\frac{1}{2}} \cdot \frac{1}{2}[E_L + E_R] - \frac{1}{2}|M_{n\frac{1}{2}}|\Delta_{\frac{1}{2}}E + \begin{bmatrix} 0 \\ (p_L^+ + p_R^-)n_x \\ (p_L^+ + p_R^-)n_y \\ (p_L^+ + p_R^-)n_z \\ 0 \end{bmatrix} \tag{45}$$

where

$$M_{n\frac{1}{2}} = M_{n_L}^{+} + M_{n_R}^{-} \tag{46}$$

The Van Leer's splitting is used to evaluate $M_n^{\pm}$. That is $M_n^{\pm} = \pm\frac{1}{4}(M_n \pm 1)^2$

where $\Delta_{\frac{1}{2}}E$ means $\Delta_{\frac{1}{2}}E = E_R - E_L$

There are two choices for the pressure splitting. The first one is the third order polynomial of M_n and is expressed as:

$$p^{\pm} = \frac{p}{4}(M_n \pm 1)^2(2 \mp M_n) \tag{47}$$

The second one is the simplest possible form of the lowest order:

$$p^{\pm} = \frac{p}{2}(1 \pm M_n) \tag{48}$$

The choice 2 can give a monotone shock profile and the choice 1 may yield oscillations near the shock.

CHAPTER IV UNFACTORED UPWIND RELAXATION-SWEEPING (URS) ALGORITHM

4.1 Description of URS Procedure

The concept of Upwind Relaxation-Sweeping is to select a direction with relatively smaller variable gradients as the global sweeping direction and to implement the local relaxation iteration on the block in the main flow direction (Zha & Liu 1990, Zha & Bilgen 1992). The flow field is calculated by a series of global alternating outward/inward sweeps in the sweeping direction with the local forward/backward Gauss-Seidel iteration on each stream wise plane, one global sweep per time step. The global sweeping is also the time marching procedure.

Upwind differencing is used for the convective and pressure terms and central differencing for the shear stress and heat flux terms. The upwind differencing is carried out by using Van Leer's flux-vector splitting (Van Leer 1982). The formulations from Eqs. (32) to (42) are used.

MUSCL- type flux differencing (Anderson & Thomas Van Leer 1986) is used to evaluate the flux passing through the interface of a cell. For instance, the inviscid flux crossing interface $S_{k+1/2}$ is determined by

$$P_{1_{i,j,k+1/2}} = P_1^+(U^-_{i,j,k+1/2}) + P_1^-(U^+_{i,j,k+1/2}) \tag{49}$$

It is to determine the $\mathbf{U}^-$ and $\mathbf{U}^+$ first and then evaluate the P_1^+ and P_1^-. The conserved state variables on the upwind side of the interface are obtained by an upwind-biased interpolation.

$$U^-_{ijk+\frac{1}{2}} = U_{ijk} + \frac{1}{4}\phi[(1-\varphi)\nabla + (1+\varphi)\Delta\ ]U_{ijk} \tag{50}$$

$$U^+_{ijk+\frac{1}{2}} = U_{ijk+1} - \frac{1}{4}\phi[(1+\varphi)\nabla + (1-\varphi)\Delta\ ]U_{ijk+1} \tag{51}$$

The symbols Δ and ∇ denote the forward and backward difference operators:

$$\Delta U_{ijk} = U_{ijk+1} - U_{ijk} \qquad \nabla U_{ijk} = U_{ijk} - U_{ijk-1} \tag{52}$$

The switch ϕ is zero for first-order differencing and unity for higher-order differencing; φ =-1 corresponds to the fully upwind second-order scheme and φ =1/3 to the upwind-biased third-order scheme.

Suppose the sweeping direction is in z-direction with the index k increasing. Discretize the governing equations (15) nearly fully implicitly for the inviscid terms and explicitly for the viscous terms, we have:

$$\frac{U_{i,j,k}^{n+1}-U_{i,j,k}^{n}}{\Delta t}Q_{i,j,k} + (P^{+n+1}_{1_{i+\frac{1}{2},j,k}}+P^{-n+1}_{1_{i+\frac{1}{2},j,k}})\bullet S_{i+\frac{1}{2}} + (P^{+n+1}_{1_{i-\frac{1}{2},j,k}}+P^{-n+1}_{1_{i-\frac{1}{2},j,k}})\bullet S_{i-\frac{1}{2}}$$

$$+(P^{+n+1}_{1_{i,j+\frac{1}{2},k}}+P^{-n+1}_{1_{i,j+\frac{1}{2},k}})\bullet S_{j+\frac{1}{2}} + (P^{+n+1}_{1_{i\,j-\frac{1}{2}\,k}} + P^{-n+1}_{1_{i\,j-\frac{1}{2}\,k}})\cdot S_{j-\frac{1}{2}}$$

$$+ (P^{+n+1}_{1_{i,j,k+\frac{1}{2}}}+P^{-n}_{1_{i,j,k+\frac{1}{2}}})\bullet S_{k+\frac{1}{2}}+(P^{+n+1}_{1_{i,j,k-\frac{1}{2}}}+P^{-n+1}_{1_{i,j,k-\frac{1}{2}}})\bullet S_{k-\frac{1}{2}} = RHS^{n}_{viscous} \qquad (53)$$

It is noted that $P^{-n}_{1_{i,j,k+\frac{1}{2}}}$ is discretized explicitly. To make the solution independent of the time step size, the implicit terms should be changed to Delta-form. To construct the implicit operator for Gauss-Seidel iteration, the Delta-form is only implemented for the terms with the same k index.

One implicit term left on the LHS is moved to RHS. Eq. (53) is then changed to:

$$[\frac{I}{\Delta t}Q + \sum\{ (\frac{dP^{+}}{dU})_k + (\frac{dP^{-}}{dU})_k \}]\delta U^{n+1} = RHS^{n,n+1}_{inviscid} + RHS^{n}_{viscous} \quad (54)$$

where:

$\delta U^{n+1} = U^{n+1} - U^{n}$, $\Delta t^{n} = t^{n+1} - t^{n}$ and n is the iteration index,

$$RHS^{n,n+1}_{inviscid} = - [(P^{+n}_{1_{i+\frac{1}{2},j,k}} + P^{-n}_{1_{i+\frac{1}{2},j,k}})\bullet S_{i+\frac{1}{2}} + (P^{+n}_{1_{i-\frac{1}{2},j,k}}+P^{-n}_{1_{i-\frac{1}{2},j,k}})\bullet S_{i-\frac{1}{2}}$$

$$+ (P^{+n}_{1_{i,j+\frac{1}{2},k}} + P^{-n}_{1_{i,j+\frac{1}{2},k}}) \bullet S_{j+\frac{1}{2}} + (P^{+n}_{1_{i\,j-\frac{1}{2}\,k}} + P^{-n}_{1_{i\,j-\frac{1}{2}\,k}}) \cdot S_{j-\frac{1}{2}}$$

$$+ (P^{+n}_{1_{i,j,k+\frac{1}{2}}} + P^{-n}_{1_{i,j,k+\frac{1}{2}}}) \bullet S_{k+\frac{1}{2}} + (P^{+n+1}_{1_{i,j,k-\frac{1}{2}}} + P^{n}_{1_{i,j,k-\frac{1}{2}}}) \bullet S_{k-\frac{1}{2}} \;] \qquad (55)$$

To keep the diagonal dominance and save computational work, first order differencing is used for the implicit terms and therefore the matrix M is penta-diagonal. The matrix equation for the cell (i,j,k) therefore can be written as:

$$B\delta U^{n+1}_{i,j+1,k} + A\delta U^{n+1}_{i,j,k} + C\delta U^{n+1}_{i,j-1,k} + E\delta U^{n+1}_{i-1,j,k} + D\delta U^{n+1}_{i+1,j,k}$$

$$= RHS^{n,\,n+1}_{inviscid} + RHS^{n}_{viscous} \qquad (56)$$

where the coefficients A, B, C, D and E are 5x5 block matrices.

The line Gauss-Seidel iteration is employed to inverse the matrix at the block composed of the cells with the same k index. Two sweeps are implemented at the local block k, one forward and the other backward. Implementation of only two sweep iterations is an approximation. An inner iterative approach such as that suggested by Taylor et al. (Taylor III & Ng & Walters 1992) to drive down the error at the local block to tolerable value may allow larger time steps. Such inner iteration approach is however not employed in this paper. After two local sweeps, the global iteration proceeds to the next block at k+1. The global sweeping starts with the inner solid wall with increasing k index. The variables are updated at each block soon after the two local sweeps for Gauss-Seidel iteration are completed. When the global iteration sweeps up to the outside solid wall, all the variables at time level n+1 are

obtained and then the sweeping direction is reversed with decreasing k index to continue the iteration for the next time step. It is believed that the iteration with forward and backward sweeps at the local block, and outward and inward globally is beneficial for the information travelling through the entire flow field three-dimensionally and therefore rapidly. It is noted that $RHS_{inviscid}^{n,\,n+1}$ in Eq. (55) is not evaluated completely by using the variables at time level n and contains one term, $P_{1_{i,j,k-\frac{1}{2}}}^{+n+1}$, which is available due to the completion of the iteration at the k-1 block.

When the global iteration sweeps in the direction with the decreasing k index , the explicit term in Eq. (53) is $P_{1_{i,j,k-\frac{1}{2}}}^{+n}$ instead of $P_{1_{i\,j\,k+\frac{1}{2}}}^{-n}$; the implicit term at time level n+1 in Eq. (55) is $P_{1_{i\,j\,k+\frac{1}{2}}}^{-n+1}$ instead of $P_{1_{i\,j\,k-\frac{1}{2}}}^{+n+1}$. Supposing each interface sub-flux has the same weight, the URS method is thus 11/12 implicit and 1/12 explicit. Fortunately, the 1/12 explicit discretization weakens little the unconditionally stable stability for the fully implicit scheme. The gain from the 1/12 explicit discretization is large: 1) the Jacobians and δU^{n+1} are only stored in one plane on which Gauss-Seidel iteration is implemented and therefore the whole storage is greatly reduced;

2) only one global sweep per time step is needed to solve all the unknowns in a time level and therefore the CPU time per time step is saved.

It can be seen from Eqs. (53) to (55) that, globally, the URS algorithm is also like a Gauss-Seidel iteration, but it is not. The updated variables are used soon after they are available. The difference is that the process of the global sweeping is also a time marching process in the sweeping direction. For the standard Gauss-Seidel iteration, the RHS residual is only evaluated using the variables at time level n. Usually, multiple sweeps, at least two sweeps, are needed in the global sweeping direction.

The $RHS_{inviscid}^{n,\,n+1}$ of Eq. (55) or (56) is evaluated by using a third order biased-upwind differencing. The accuracy of the converged solution is controlled by RHS. Therefore the algorithm possesses third order accuracy for inviscid steady state flows. But because central differencing is used for the viscous terms, the general accuracy of the solution for the 3D Navier-Stokes equations is second order.

The disadvantage of URS algorithm is that it is not fully conservative for a given time level because variables at time level n and n+1 are used at the same time to evaluate the residual. Therefore it may be inappropriate to use URS algorithm for unsteady problem.

4.2 Stability Analysis

Von Neumann stability analysis is carried out for the linear scalar model convection equation:

$$U_t + uU_x + vU_y + wU_z = 0 \tag{57}$$

This equation can be rewritten using the split characteristic values with non-negative and non-positive signs as:

$$U_t + (u^+ + u^-)U_x + (v^+ + v^-)U_y + (w^+ + w^-)U_z = 0 \tag{58}$$

where

$$u^+ = \frac{u + |u|}{2} \geq 0, \quad u^- = \frac{u - |u|}{2} \leq 0 \tag{59}$$

$$v^+ = \frac{v + |v|}{2} \geq 0, \quad v^- = \frac{v - |v|}{2} \leq 0 \tag{60}$$

$$w^+ = \frac{w + |w|}{2} \geq 0, \quad w^- = \frac{w - |w|}{2} \leq 0 \tag{61}$$

Suppose the global sweeping is in the direction with the increasing k index. Using first order upwind differencing to discretize the model equation, that is: backward differencing for the positive characteristic values and forward differencing for the negative characteristic values, we obtain the following 11/12 implicitly discretized equation:

$$\frac{U_{ijk}^{n+1} - U_{ijk}^{n}}{\Delta t} + u^+ \frac{U_{ijk}^{n+1} - U_{i-1jk}^{n+1}}{h} + v^+ \frac{U_{ijk}^{n+1} - U_{ij-1k}^{n+1}}{k}$$

$$+ w^{+}\frac{U^{n+1}_{i\,j\,k} - U^{n+1}_{i\,j\,k-1}}{l} + u^{-}\frac{U^{n+1}_{i+1\,j\,k} - U^{n+1}_{i\,j\,k}}{h} + v^{-}\frac{U^{n+1}_{i\,j+1\,k} - U^{n+1}_{i\,j\,k}}{k}$$

$$+ w^{-}\frac{U^{n}_{i\,j\,k+1} - U^{n+1}_{i\,j\,k}}{l} = 0$$

by rearranging the terms, we have:

$$U^{n+1}_{i,j,k}(1+\alpha^{+}+\beta^{+}+\gamma^{+}-\alpha^{-}-\beta^{-}-\gamma^{-}) + \alpha^{-}U^{n+1}_{i+1,j,k}-\alpha^{+}U^{n+1}_{i-1,j,k}$$

$$+\beta^{-}U^{n+1}_{i,j+1,k}-\beta^{+}U^{n-1}_{i,j-1,k}-\gamma^{+}U^{n+1}_{i,j,k-1}-U^{n}_{i,j,k}+\gamma^{-}U^{n}_{i,j,k+1} = 0 \qquad (62)$$

where:

$$\alpha^{+} = \frac{u^{+}\Delta t}{h} \geq 0, \quad \alpha^{-} = \frac{u^{-}\Delta t}{h} \leq 0 \qquad (63)$$

$$\beta^{+} = \frac{v^{+}\Delta t}{k} \geq 0, \quad \beta^{-} = \frac{v^{-}\Delta t}{k} \leq 0 \qquad (64)$$

$$\gamma^{+} = \frac{w^{+}\Delta t}{l} \geq 0, \quad \gamma^{-} = \frac{w^{-}\Delta t}{l} \leq 0 \qquad (65)$$

h, k and l are the grid intervals in x, y and z directions.

Obviously, we have :

$$|1+ \alpha^{+} + \beta^{+}+ \gamma^{+}- \alpha^{-} -\beta^{-} -\gamma^{-}| > |\alpha^{-}|+|-\alpha^{+}|+|\beta^{-}|+|-\beta^{+}|+|-\gamma^{+}| \qquad (66)$$

Thus Eq. (62) is diagonally dominant and satisfies the convergence conditions for iterative method. It is noted that the diagonal dominance is stronger than the fully

implicit scheme because the 1/12 explicit term does not make contributions to the off diagonal elements. However, only when the amplification factor of the round-off error is proven to be less than unity, the time marching procedure can be stable.

Suppose the round-off error function is E(x,y,z,t) which can be expressed by the Fourier series as :

$$E(x,\ y,\ z,\ t) = \sum_{m=1}^{M-1}\sum_{n=1}^{N-1}\sum_{j=1}^{J-1} Ae^{imk_1x}e^{ink_2y}e^{ijk_3z} = \sum_{m=1}^{M-1}\sum_{n=1}^{N-1}\sum_{j=1}^{J-1} Ae^{iax}e^{iby}e^{icz} \qquad (67)$$

where A is the amplitude of the single wave which is a function of time; $a=mk_1$, $b=nk_2$ and $c=jk_3$ are the wave number in x, y and z direction within 2π length. Since the model equation is linear, superposition can be used and we may examine the behaviour of a single term of the series. Consider a single term:

$$e(x,\ y,\ z,\ t) = Ae^{iax}e^{iby}e^{icz} \qquad (68)$$

The error function satisfies the discretized equation with the same form for U due to the linearity of the model equation. Substitute the single term, Eq. (68), into Eq.(62) and rearrange the terms. We obtain the amplification factor:

$$g = \frac{A^{n+1}}{A^{n}}$$

$$= \frac{1 - \gamma^{-}e^{i\varphi}}{1+\alpha^{+}+\beta^{+}+\gamma^{+}-\alpha^{-}-\beta^{-}-\gamma^{-}+\alpha^{-}e^{i\theta}-\alpha^{+}e^{-i\theta}+\beta^{-}e^{i\phi}-\beta^{+}e^{-i\phi}-\gamma^{+}e^{-i\varphi}} \qquad (69)$$

where $\theta = ah$, $\phi = bk$, $\varphi = cl$ are the difference of wave phase angles

of two neighbouring grid points in x, y and z directions.

From Eq. (69), we have

$$g^2 = [1 - 2\gamma^- \cos\varphi + (\gamma^-)^2] \,/\, \{ [1+(\alpha^+-\alpha^-)(1-\cos\theta)+(\beta^+-\beta^-)(1-\cos\phi)$$

$$+\gamma^+(1-\cos\varphi)-\gamma^-]^2+[(\alpha^++\alpha^-)\sin\theta+(\beta^++\beta^-)\sin\phi+\gamma^+\sin\varphi]^2 \} \tag{70}$$

where

$$\cos\theta \le 1, \quad \cos\phi \le 1, \quad \cos\varphi \le 1 \tag{71}$$

$$|\sin\theta| \ge 0, \quad |\sin\phi| \ge 0, \quad |\sin\varphi| \ge 0 \tag{72}$$

by taking the limits, with:

$$\cos\theta = 1, \quad \cos\phi = 1, \quad \cos\varphi = 1 \tag{73}$$

$$\sin\theta = 0, \quad \sin\phi = 0, \quad \sin\varphi = 0 \tag{74}$$

the numerator of Eq. (70) reaches the maximum and the denominator reaches the minimum. Therefore the amplification factor obtains the maximum value:

$$g^2_{max} = \frac{(1-\gamma^-)^2}{(1-\gamma^-)^2} = 1 \tag{75}$$

Thus we have:

$$g^2 \le g^2_{max} = 1 \tag{76}$$

Therefore, we conclude that, for the linear model equation, the URS algorithm with

$$|g| \le 1 \tag{77}$$

first order differencing is unconditionally stable. Eqs. (66) and (77) still apply when the global sweeping is in the direction with the decreasing k index due to the symmetry of the model equation. Therefore the stability is independent of the selection of the global sweeping direction.

It can be seen from Eq. (69) that, if $\gamma^- \to 0$, $\Delta t \to \infty$, the amplification factor $|g| \to 0$. That is the maximum dumping occurs when $\gamma^- \to 0$, $\Delta t \to \infty$. These conditions are weaker than the fully implicit unfactored scheme for which the maximum dumping occurs when $\Delta t \to \infty$. The extra condition, $\gamma^- \to 0$, is due to the 1/12 explicit discretization. $|\gamma^-|$ to be small means that the convection speed $|w^-|$ is small when a time step size and grid spacing are fixed. That is, even though the URS is unconditionally stable and independent of the global sweeping direction, if we choose the direction with relatively lower variable gradients as the global sweeping direction, the URS can hold higher degree of stability. This is the theoretical base of the URS scheme.

It should be reminded that the above conclusions are all based on discretization using first order differencing on both LHS and RHS. In this thesis, higher order differencing is employed for the evaluation of RHS to obtain higher order accuracy solutions. The advantages using first order differencing on LHS are:

1) the diagonal dominance of the coefficient matrix is retained and therefore the iteration convergency conditions are satisfied; 2) CPU time can be saved to solve the implicit operator since only the block tridiagonal matrixes need be inversed. If a higher order differencing is used for the LHS, the diagonal dominance will be lost and therefore the under-relaxation must be used. Block penta-diagonal matrixes must be solved for a higher order differencing and therefore more computational work is necessary. The disadvantage of the inconsistent differencing order for LHS and RHS is that the convergency rate will be reduced compared with the consistent discretization.

4.3 Boundary Conditions and Time Stepping

The wall boundary treatment for 2D flow suggested by Zha et. al (Zha & Liu & Ma 1989) is extended to the present 3D calculation. For viscous flow, on the wall, the solution point is put on the surface of the wall instead of the center of the cell like the internal point (see Fig. 2). For the cell in the corner, the solution point is just located on the point of the corner.

The no-slip conditions are set as

$$u=v=w=0,\ p_1 = p_2 \text{ as } \partial p/\partial n = 0 \tag{78}$$

$$T_1 = T_2 \quad \text{for the adiabatic wall} \tag{79}$$

The wall boundary conditions are treated explicitly. The high convergence rate can still be reached due to the accurately imposed no-slip conditions.

The time step is determined by the following formulation:

$$\Delta t = C \cdot (\Delta y + \Delta z)/(v + w + 2a) \tag{80}$$

where a is the speed of sound. The formulation is very effective for the highly stretched grid in y and z directions.

For inviscid flows, the conditions for slip and adiabatic wall are used on the solid surfaces. The flux on the wall is

$$Z_W = [\ 0 \quad p_w n_w \quad p_w n_y \quad p_w n_z \quad 0\ ]^T \tag{81}$$

The pressure is first order extrapolated from the inner points. On the implicit side,

$$\delta Z_W^{n+1} = \frac{\partial Z_W}{\partial U} \delta U^{n+1} \tag{82}$$

where $\frac{\partial Z_W}{\partial U}$ is the Jacobian matrix and incorporated into the matrix equations. At the inlet and the exit, the number of the variables determined from the inner points is based on the characteristic theory and the variables are first order extrapolated. For subsonic flow at the inlet, total temperature T^*, total pressure P^* and inlet flow angle are given. One parameter is extrapolated from the internal field. At the exit, if the flow is subsonic, static back pressure is given. The rest of the parameters are extrapolated; if the flow is supersonic, all the parameters are extrapolated.

CHAPTER V THE NEW FLUX VECTOR SPLITTING SCHEME

5.1 Construction of the 1D Form of the New FVS Scheme

At the beginning, we would like to take the 1D Euler equations as an example to explain how the scheme is constructed. The 1D Euler equations expressed in Cartesian coordinates and conservation form are

$$U_t + F_x = 0 \tag{83}$$

where the vectors U and F are given by

$$U = \begin{bmatrix} \rho \\ \rho u \\ e \end{bmatrix} \quad , \quad F = \begin{bmatrix} \rho u \\ p+\rho u^2 \\ (e+p)u \end{bmatrix} \tag{84}$$

Let

$$A = \frac{\partial F}{\partial U} \tag{85}$$

where A is a 3 x 3 Jacobian matrix. It is already well known that the matrix has three real eigenvalues, **u, u +** a **, u -** a , where a is the sound speed.The following equation can be derived by splitting the diagonal eigenvalue matrix to two parts

$$F = AU = Q\Lambda Q^{-1}U$$

$$= Q \begin{bmatrix} u & 0 & 0 \\ 0 & u & 0 \\ 0 & 0 & u \end{bmatrix} Q^{-1}U + Q \begin{bmatrix} 0 & 0 & 0 \\ 0 & a & 0 \\ 0 & 0 & -a \end{bmatrix} Q^{-1}U \quad = C+P \tag{86}$$

where C and P represent the convective and pressure terms:

$$C = u \begin{bmatrix} \rho \\ \rho u \\ e \end{bmatrix} \quad , \quad P = \begin{bmatrix} 0 \\ p \\ pu \end{bmatrix} \tag{87}$$

Obviously, the eigenvalues of the Jacobian of C and P are (**u, u, u**) and (0, a , - a) respectively. This suggests that the information of the convective terms propagate uniformly in the same direction as the velocity vector u goes and the information of the pressure terms travels with the convective terms at the speed u and propagate in every direction at the sound speed a . The present scheme is contrived to evaluate the interface flux $F_{i+\frac{1}{2}}$ at locations such as (i + 1/2 Δx) according to the information travel directions of vector C and P respectively. The following is the details of the present scheme :

$$F_{i+\frac{1}{2}} = F_L^+ + F_R^- \tag{88}$$

For subsonic flow, $|\mathbf{u}| < a$, the pressure terms are determined by

$$P_{i+\frac{1}{2}} = P_L^+ + P_R^- \qquad where \qquad P^{\pm} = \frac{1}{2}\begin{bmatrix} 0 \\ p(1\pm M) \\ p(u\pm a) \end{bmatrix} \tag{89}$$

The convective terms are

$$if \quad a>u\geq 0, \quad C_{i+\frac{1}{2}} = C_L^+ + C_R^- \quad where \quad C_L^+ = C_L, \quad C_R^- = 0 \tag{90}$$

$$if \quad -a<u<0, \quad C_{i+\frac{1}{2}} = C_L^+ + C_R^- \quad where \quad C_L^+ = 0, \quad C_R^- = C_R \tag{91}$$

$$F_L^+ = C_L^+ + P_L^+ \tag{92}$$

$$F_R^- = C_R^- + P_R^- \tag{93}$$

Thus, Eq. (88) can be written as the following general and simple form:

$$F_{i+\frac{1}{2}} = \frac{1}{2}(F_L + F_R) - \frac{1}{2}\left[\left[|u| \begin{bmatrix} \rho \\ \rho u \\ e \end{bmatrix} + \begin{bmatrix} 0 \\ pM \\ pa \end{bmatrix} \right]_R - \left[|u| \begin{bmatrix} \rho \\ \rho u \\ e \end{bmatrix} + \begin{bmatrix} 0 \\ pM \\ pa \end{bmatrix} \right]_L \right] \tag{94}$$

For supersonic flow, it is the same as the standard upwind differencing scheme. That is

$$F_{i+\frac{1}{2}} = F_L^+ + F_R^- \tag{95}$$

$$if \quad u \geq a, \quad F^+ = F_L \qquad F^- = 0 \tag{96}$$

$$if \quad u \leq -a, \quad F_L^+ = 0, \quad F_R^- = F_R \tag{97}$$

It can be proven that the eigenvalues of P^+ and P^- are non-negative and non-positive for the flows with $\gamma \geq 1$. The pressure splitting for momentum equation is taken from Liou-Steffen's AUSM scheme. The pressure power term in the energy equation is split using the similar idea. The whole pressure splitting is based on the acoustic propagation speeds $(u \pm a)$ or their weights $(M \pm 1)$ for average. This may represent the pressure propagation characteristics.

It is clear that the split flux is continuous everywhere. It leads to standard upwind scheme in the supersonic region. The mass flux is the same as the natural one and therefore also continuously differentiable everywhere. As shown in Fig. 23, the individual mass flux vanishes with the Mach number approaching zero while those of Van Leer's FVS and Steger-Warming's FVS do not vanish. However, the individual split flux for pressure term is not continuously differentiable across the sonic point. When a first order differencing is used this will cause a glitch at the

sonic point similar to that by Steger-Warming scheme. Fortunately, this glitch can be removed automatically by using higher order differencing. Liou and Steffen (Liou & Steffen 1991) reported that this pressure splitting could get smoother transition across the sonic point than the continuously differentiable one with the higher order polynomial. This may be true only when higher order differencing is used. The advantage of this pressure splitting is that it can obtain the monotone shock profile even when the second order differencing is used. At the stagnation point, unlike the Steger-Warming scheme, the present scheme is continuously differentiable.

Except the low numerical diffusion, one obvious advantage of the present scheme is its simplicity. Similarly to Van Leer and Liou-Steffen AUSM schemes, it does not need the matrix operations required by Roe scheme. The formulations are polynomial in M (Mach number) and of degree one, which is the lowest possible degree. The implementation of this scheme is even easier than AUSM scheme. Though AUSM scheme is already very simple, its interface Mach number containing both left and right side variables is not so convenient to get the Jacobian matrix when implicit discretization is to be implemented. The interface flux of present scheme is composed of the vectors with the pure left side variables and the pure right side variables like Van Leer scheme. It is straightforward to construct the implicit operator.

5.2 Numerical Diffusion of the New FVS Scheme

From Eq. (94), it is seen that the present flux vector splitting scheme can be exactly written as a central differencing plus the diffusive terms. For supersonic flow, the

diffusion is the same as the standard upwind scheme. The focus here is concentrated in the subsonic region.

Let

$$D = |u| \begin{bmatrix} \rho \\ \rho u \\ e \end{bmatrix} + \begin{bmatrix} 0 \\ pM \\ pa \end{bmatrix} \tag{98}$$

the diffusive vector, namely D_{dif} , can be expressed as

$$D_{dif} = \frac{1}{2}(D_R - D_L) \tag{99}$$

Eq. (94) then can be rewritten as

$$F_{i+\frac{1}{2}} = \frac{1}{2}[\ F_L + F_R\ ] - D_{dif} \tag{100}$$

For the extrapolation schemes with different order accuracy, the accuracy order of D_{dif} is also different. D_{dif} is equivalent to adding the following derivatives into Euler equations if central differencing is used.

For first order fully upwind extrapolation

$$D_{dif} = \frac{1}{2}\frac{\partial^2 D}{\partial x^2}\Delta x \tag{101}$$

For second order fully upwind extrapolation

$$D_{dif} = -\frac{1}{4}\frac{\partial^4 D}{\partial x^4}\Delta x^3 \tag{102}$$

For third order upwind-biased extrapolation

$$D_{dif} = -\frac{1}{12}\frac{\partial^4 D}{\partial x^4}\Delta x^3 \tag{103}$$

From Eq. (98), it can be seen that almost all the diffusive terms vanish at the stagnation except only one term, pa , in the energy equation. The vanishing terms may ensure that their diffusion is small. Even though pa does not vanish, the dissipation is within the magnitude order of the truncation error. As Eqs. (102) and (103) show, if a higher order differencing is used, the low diffusion may be furthermore ensured by the higher order derivatives and the higher power of the grid spacing. The diffusion generated by pa , $-\frac{1}{4}\frac{\partial^4 pa}{\partial x^4}\Delta x^3$ or $-\frac{1}{12}\frac{\partial^4 pa}{\partial x^4}\Delta x^3$, may also be expected to remain small.

In many cases, the gradient of pa near the solid wall may be small.

Particularly for some practical cases, when the sound speed is only considered as the function of temperature as the ideal gas, if the wall is adiabatic and the pressure gradient normal to the wall is zero or small enough to be treated as zero, the diffusion of pa will disappear by cancellation and therefore the total diffusion will disappear on the wall no matter which order of differencing is used.

For the ability of the present scheme to capture shock waves, it is not proven here by analysis how sharp the shock wave profile will be. But the computational experiments presented later show that the normal shock captured is as crisp as that obtained by using the Roe scheme and is at most two transition zones.

5.3 Three-Dimensional Form of the New FVS Scheme

$\mathbf{P}_1$ will be evaluated by using the present flux vector splitting scheme. The extension of the scheme from 1D to 3D is straightforward. $\mathbf{P}_1$ in Eq. (18) can be written as:

$$P_1 = C + P \tag{104}$$

where

$$C = U_n \begin{bmatrix} \rho \\ \rho u \\ \rho v \\ \rho w \\ e \end{bmatrix} \qquad P = \begin{bmatrix} 0 \\ pn_x \\ pn_y \\ pn_z \\ pU_n \end{bmatrix} \tag{105}$$

C and P still stand for the convective and pressure terms. Similarly to the 1D case, the eigenvalues of the Jacobian matrix of the convective vector are ($\mathbf{U}_n$, $\mathbf{U}_n$, $\mathbf{U}_n$, $\mathbf{U}_n$, $\mathbf{U}_n$). The eigenvalues for the pressure term matrix are still (0, 0, 0, $+a$ $-a$).

Using the eigenvalues of the convective term Jacobian matrix as the characteristic speed, the three-dimensional form of this flux vector splitting scheme can be expressed as the following

$$P_1 = P_{1_L}^{+} + P_{1_R}^{-} \tag{106}$$

For subsonic flow, $|\mathbf{U}_n| < a$, the pressure terms are

$$P_{i+\frac{1}{2}} = P_L^{+} + P_R^{-} = \frac{1}{2}\begin{bmatrix} 0 \\ p(1+M_n)n_x \\ p(1+M_n)n_y \\ p(1+M_n)n_z \\ p(U_n+a) \end{bmatrix}_L + \frac{1}{2}\begin{bmatrix} 0 \\ p(1-M_n)n_x \\ p(1-M_n)n_y \\ p(1-M_n)n_z \\ p(U_n-a) \end{bmatrix}_R \tag{107}$$

The convective terms are

$$\text{if} \quad a>U_n\geq 0, \quad C_{i+\frac{1}{2}} = C_L^{+} + C_R^{-} \quad \text{where} \quad C_L^{+}=C_L, \quad C_R^{-}=0 \tag{108}$$

$$\text{if} \quad -a<U_n<0, \quad C_{i+\frac{1}{2}} = C_L^{+} + C_R^{-} \quad \text{where} \quad C_L^{+}=0, \quad C_R^{-}=C_R \tag{109}$$

$$P_{1_L}^{+} = C_L^{+} + P_L^{+} \tag{110}$$

$$P_{1_R}^- = C_R^- + P_R^- \tag{111}$$

Let

$$D = |U_n| \begin{bmatrix} \rho \\ \rho u \\ \rho v \\ \rho w \\ e \end{bmatrix} + \begin{bmatrix} 0 \\ pM_n n_x \\ pM_n n_y \\ pM_n n_z \\ pa \end{bmatrix} \tag{112}$$

The general form of the present scheme in 3D is given as:

$$P_{1\frac{1}{2}} = \frac{1}{2}(P_{1_L} + P_{1_R}) - \frac{1}{2}(D_R - D_L) \tag{113}$$

For supersonic flow

$$if \quad U_n \geq a, \quad P_{1_L}^+ = P_{1_L} \quad , \quad P_{1_R}^- = 0 \tag{114}$$

$$if \quad U_n \leq -a, \quad P_{1_L}^+ = 0, \quad P_{1_R}^- = P_{1_R} \tag{115}$$

The Mach number M_n is based on the normal component of the velocity, $M_n = U_n/a$. The diffusion terms corresponding to Eqs. (100) to (102) are changed now to the following forms:

For first order fully upwind extrapolation

$$D_{dif} = \frac{1}{2}\frac{\partial^2 D}{\partial n^2}\Delta n \tag{116}$$

For second order fully upwind extrapolation

$$D_{dif} = -\frac{1}{4}\frac{\partial^4 D}{\partial n^4}\Delta n^3 \tag{117}$$

For third order upwind-biased extrapolation

$$D_{dif} = -\frac{1}{12}\frac{\partial^4 D}{\partial n^4}\Delta n^3 \tag{118}$$

where n is the direction normal to the cell interfaces

CHAPTER VI RESULTS AND DISCUSSION

6.1 The Results for URS algorithm

To validate the URS algorithm, it is applied to solve 3D Euler and laminar Navier-Stokes equations. The computational cases chosen are all internal flows involving mainly transonic duct flows due to current interest in nonaxisymmetric exhaust nozzles.

Unless indicated, the first order differencing for the LHS and the third order differencing for the RHS were used. All the calculations started from the rest initial fields, u=v=w=0, with pressure and temperature set everywhere to their total values.

6.1.1 Solutions of 3D Euler Equations

Case 1: transition ducts with a nonaxisymmetric transonic nozzle.

A transition duct is needed to connect the axisymmetric engine to the nonaxisymmetric nozzle through a smooth progression of geometrically similar cross sections which is a series of superellipse. Figure 6.1. (1) shows a sketch of such geometry. Two transition ducts with a nonaxisymmetric transonic nozzle designed and tested experimentally by Burley et al. (Burley & Bangert & Carlson 1986) are calculated. Figure 6.1. (2) shows the geometry of the first duct and the grid with the

size of 101x31x31. The characteristic geometric parameters for the transition ducts are given in Table 1:

Table 1. Geometric parameters for the transition ducts

Duct	L/D	α_1, deg	α_2, deg
Duct 1	1.0	42.7^0	25.9_0
Duct 2	1.0	31.6	17.9

where L/D is the ratio of the transition duct length to the entrance diameter, α_1 the maximum slope angle of transition along the sidewall, α_2 the maximum slope angle of transition along top or bottom walls. The two ducts have the same constant cross-sectional area, A_{cs} = 20.1408 in^2. The method of calculating circular-to-rectangular transition surfaces is given in Appendix B. The transition duct must be as short as possible to minimize the weight of the propulsion system installation. It must also be long enough to prevent any flow separation, which could adversely affect performance and create severe wall cooling problems. The cooling problem arises because most turbojet engines rely on a thin film of cool air injected parallel to the walls to maintain temperatures within thermal limits. Flow separation causes the cool air to mix with the hot gases from the engine and then magnifies the problem by concentrating the hot gases at one or more stagnation. To prevent flow separation,

α_1 and α_2 are chosen to be less than 45^0 as suggested by Stevens et al. (Stevens & Thayer Fullerton 1981). Therefore with little probability of separation, the Euler equations may predict well the general feature of the flow field. In the experimental study (Burley & Bangert & Carlson 1986), the entrance flows with and without swirl were tested. The swirl flow is considered to be able to alleviate some flow separation by imparting a radial component to the velocity vectors. More importantly, they can be used to reduce the noise associated with the jet exhaust. In the experiment, the swirl flow was induced by installing 12 vanes with 20^0 angle inclined to the axis. Both flows with and without entrance swirl were calculated in this thesis. The wall shape functions of duct 1 are third order curves which ensure smooth connection with the nozzle. Duct 2 has the straight or linear wall shape whose derivative at the connection with the nozzle is not continuous. The results of duct 1 with the nozzle in detail is first presented as the following .

To test the dependence of the convergence rate on the grid size, 51x21x21 and 101x31x31 grid sizes were calculated. The flow with entrance swirl is presented here, a case with a lower convergency rate. The maximum CFL number used is 500 for the grid 51x21x21 and 540 for 101x31x31. Single precision is used and the residuals are driven down to machine zero by using 320 iterations for the coarse grid and 581 iterations for the fine grid shown in Fig.6.1. (3). It is seen that the convergency rates are rapid. However, they depend on the grid size and are slower for the finer. Figure 6.1. (4) is the Mach number distribution along the center line which is from subsonic to supersonic. Figure 6.1. (5) presents the calculated pressure distributions along the side and bottom wall center-lines compared with the

experiments with and without entrance swirl flow. The result with no swirl flow in Fig. 6.1. (5) (a) and (b) agrees very well with the experiment. The computational result almost goes through the experimental points. The pressure has a sharp rise at the throat due to the short compression right after the sonic line and goes down soon after the throat due to the supersonic acceleration. For the case with entrance swirl flow, experimental data are only available for the transition duct shown in Fig.6.1. (5) (c) and (d). It is seen that the pressure values are higher than the experimental data near the end of the transition duct. The main reason may be that it is not easy to simulate the entrance swirl flow accurately. We assumed that the entrance flow had a uniform swirl angle at the entrance plane. The experimental swirl device produces wakes behind the vanes and vane shaft and the flow entering the transition duct is not uniformly swirled. We also assumed that the swirl at the inlet of the duct is 20^0. For the experiment, the swirl vanes have a distance from the duct inlet. The swirl flow may not be kept exactly at 20^0 when it approaches the inlet of the duct due to the influence of the wall boundary layers and the wakes. In fact, our computational experiments showed that the inlet boundary condition had quite a strong influence on the results. Despite such approximations, the computational result generally agrees quite well with the experiment as shown in Fig. 6.1. (5).

It is interesting to see the transverse flow caused by the entrance swirl flow. To exclude the effect of the geometry, first see the cross flow without the entrance swirl shown is Fig. 6.1. (6). The section with the superelliptic shape is in the part of transition duct and the rectangular section in the supersonic part of the nozzle after the throat. It is seen that the cross flow is symmetric about the horizontal and vertical

planes. On the two sides of the top and bottom wall center points, the flow goes towards two different sides. We may define the two points as the transverse flow division points. There is no vortex flow in the flow field. The transverse flow is completely produced by the three-dimensional geometry of the transition duct. When there is an entrance swirl, the transverse flow structure is changed quite much as shown in Fig. 6.1. (7). Fig. 6.1. (7) is the entrance section with the flow uniformly swirled. The cross flow circulates in one direction induced by the swirl vanes. Such a flow picture retains for a short distance after the inlet. With the flow going in and the cross section changing to superellipse, the circulation is split and the typical cross flow becomes as shown in Fig. 6.1. (7) (b). The flow is not symmetric any more. The division point on the top wall moves to the right and the one on the bottom wall to the left. A vortex is kept around the center of the section. Such a cross flow field structure is maintained along the nozzle from the subsonic part to the supersonic part till the exit of the nozzle. Most of the flow on the top half goes to the left and on the lower half goes to the right. The flow velocity near the two side extremes has some tangent components and the magnitude is slightly higher than the one with no entrance swirl. It is what the designers want to keep the flow attached on the side walls which may have large divergence angles. Figure 6.1. (7) also shows the different locations of the stream division points at different sections which form the transverse stream division lines on the upper and lower walls. Such stream division line locations were not identified before. Perhaps, care should be taken to study if these transverse stream division lines cause flow separation problems. More information may be obtained however by studying such flow field structures by solving the 3D Navier-

Stokes equations.

Figure 6.1. (8) demonstrates the Mach number contours of the flow field with the entrance swirl flow. It shows that the variation of the Mach number in spanwise direction is large in the transition duct part and becomes relatively more uniform in the nozzle part. But the flow field in the nozzle part is still highly three-dimensional for the flow with and without entrance swirl as shown by the transverse velocity field in Fig. 6.1. (6) and 6.1. (7) even though the geometry is two-dimensional. There is no shock waves in this flow although it is transonic.

The general flow field feature of duct 2 with the nozzle is similar to that of duct 1 and would not be presented here in detail. The significant difference is that the linear wall shape has the connection with the nozzle which is not continuously differentiable as shown in Fig. 6.1. (9). Such unsmooth connection will cause the flow parameter jump due to the abrupt compression on the top and bottom wall and expansion on the side walls. Fig. 6.1. (10) presents the pressure distributions showing the jump at the location of connection. The advantage of the linear wall shape is its simplicity to build. However, the unsmooth parameter distributions may cause flow separations.

Case 2: nonaxisymmetric transonic nozzle

This case is only a nonaxisymmetric transonic nozzle with no transition duct, which is chosen for a preliminary test of the flow with shock waves. Figure 6.1. (11) shows the geometry calculated which is only a quarter of the whole nozzle due to symmetry. The flow generally is two dimensional because of the rectangular section.

Figure 6.1. (12) is the pressure contours of a typical streamwise section. Oblique shock waves exist after the throat. The shock waves are weak because the Mach number is only slightly greater than one after the throat. The two shock waves extending from the lower and upper wall intersect at the center-line of the nozzle and then reach the wall of the other side. After approaching the wall, the oblique shock waves reflect. These reflections intersect and reflect again until the flow approaches the exit of the nozzle. It can be seen from Fig. 6.1. (12) that the intensity of the shock waves becomes weaker with repeated intersections and reflections. This can be also quantitatively seen from the pressure distributions given in Fig. 6.1. (13). Fig. 6.1. (13) (a), (b), (c) are at the bottom wall with different locations from the center-line (Z/L=0.) to the one near the side wall (Z/L=0.875). Fig.6.1. (13) (d) is the pressure distribution along the side wall center-line. Most of the computational points agree very well with the experiment (Mary et al. 1980) except the point at the first shock reflection. The first reflection calculated seems to be not strong enough. The maximum CFL number used for this case was 130. Figure 6.1. (14) shows the convergency history which reaches the machine zero rapidly. It is interesting to note that the maximum CFL number was greater than 10^6 when this case was tested by solving the 3D Navier-Stokes equations using the same algorithm. Such a high CFL number was possible because the algorithm can sustain very highly stretched grid near the solid wall. The results are presented in next section.

Case 3: three-dimensional channel

This channel is designed by Benay, et al. (Benay & Delery & Pot 1986) for

an experimental study. Figure 6.1. (15) shows the geometry and the grid with 101x31x31 size. The channel has three flat walls and a humped lower wall. The upstream part of the hump is a ramp, inclined approximately at 7 degree from the horizontal. This ramp is followed by convex circular surfaces of 100 and 180 mm radius defined to ensure slope continuity everywhere. The angle formed by the hump crest and line, and the channel axis is equal to 60 degree. The maximum height of the hump is 20 mm and the channel section is 120 mm wide and 100 mm high at the inlet. In the experiment made at ONERA, this channel yielded complex 3D flow field produced by the shock wave/boundary layer interaction. Figure 6.1. (16) shows the experimental Mach number contours. The back pressure was not obtained due to some experimental difficulties. Therefore, different back pressures were tested in the calculation to match the flow field structure. Figure 6.1. (17) shows the Mach number contours on the walls corresponding to a dimensionless back pressure of 0.545, defined as the ratio of the back pressure to total pressure. This value is taken from Cambier and Escande (1990) who solved the Reynolds averaged Navier-Stokes equations and obtained qualitative agreement with the experiment. The shock wave structure calculated in this paper is obviously different from the experimental one and is very complex. It can be seen from Figs. 6.1. (16) and (17) that the calculated starting point location of the shock agrees quite well with the experiment. The experimental shock wave is also oblique in the lower half of the channel and becomes normal above the channel center-line. The calculated shock wave keeps the same oblique angle up to the upper wall. The transverse shock location is not normal to the axis of the channel. Near the right side wall, the oblique shock is reflected on the

upper wall and then on the bottom wall. Across the channel, two shock waves interact and λ-shape shock wave forms. The upstream root of the λ shock has a weak reflection on the upper wall. The downstream root of the λ shock has quite strong reflections on both upper and left walls. The intensity of the shock wave becomes stronger near the right side wall. This agrees with the experiment. Because of the very complex shock wave structure, the computational convergence is usually difficult and the problem represents a good case to test the convergency behaviour of the URS algorithm. To study the convergency rate under the influence of the different order differencing used for the LHS and the RHS, both the first order and the third order differencing were tested for the RHS. Figure 6.1. (18) shows the convergency histories. It is seen that the convergency rate with the first order on the LHS the third order on the RHS is slower than with first order differencing used on both sides. There are two reasons for this outcome. Firstly, the inconsistent differencing order used for the LHS and the RHS will reduce the convergency rate as mentioned in the section of stability analysis. Secondly, when the third order is used for the RHS, the numerical diffusion is less and the shock waves are sharper than those captured by using the first order differencing. The crisp shock wave profiles make the convergence more difficult than by using the first order differencing. The second reason for the slower convergency rate is considered to be more important. It is interesting to note from Fig. 6.1. (18) that most of the iterations are in the high residual level and used to form the shock waves. After overcoming the large residuals from the shock waves, they go down very sharply to the machine zero and never go up again. The CFL number for this case is largely reduced

compared with the previous two cases. With the first order differencing on the RHS, the maximum CFL number is 32, with the third order on the RHS is 24. The case with 0.645 dimensionless back pressure gave a very similar flow field structure. When the back pressure is 0.755, only one normal shock wave exists in the flow field which is shown in Fig. 6.1. (19). In this case, the convergency rate is faster due to a simpler shock wave structure in the flow field. Even though the back pressure ratio of 0.755 gives a normal shock which is similar to the experimental results, this agreement does not mean that 0.755 is the correct back pressure. Actually, this shock location is ahead of the experimental one and the shock wave shape is also quite different. The reason for not having a similar flow field structure with 0.545 back pressure to those experimental and theoretical (Cambier & Escande 1990), may be due to nonexistence of wall boundary layers. The strong shock wave/boundary layer interaction on the lower wall will cause a flow separation and make the shock less oblique. The incidence shock may almost normally interact with the upper wall boundary layer with no reflection. No-slip wall boundary conditions for viscous flows could weaken the shock reflection. On the contrary, the slip wall boundary conditions for the Euler equations could make the shock reflection easier when the shock has an oblique angle. The observed deviation of the flow field structure for this case may be mainly because the Euler model has been used. For such complex shock wave structures, the Navier-Stokes model would give better results. The other possibility of the observed deviation may be because the back pressure has been assumed to be uniform, which is usually not true even though this assumption has produced qualitative agreement with the experimental results (Cambier & Escande 1990). The

back pressure is a key factor to determine the shock wave structure. A more accurate back pressure selection would result in a better solution. Despite the shortcomings, the efficiency and robustness of the URS algorithm has been still demonstrated for this case.

6.1.2 Solutions of 3D Navier-Stokes Equations: Effect of Throat Contouring on Nonaxisymmetric Nozzles

Five nonaxisymmetric converging-diverging nozzles named as A1, A2, B1, B2 and B3 (Mary et al. 1980) were calculated at the design conditions by solving 3D laminar Navier-Stokes equations using URS method. The purposes are to test URS algorithm for 3D Navier-Stokes equations and to study the internal-performance effect of throat contouring, the result of increasing the circular-arc throat radius. The flow fields of the nozzles are supposed to be symmetric about the center plane in y and z- direction. Therefore only the lower half or 1/4 part of a nozzle shown as Fig.6.1. (20) is calculated to reduce the computational work. Nozzle A1 and B1 are the baseline nozzle geometries with the same circular-arc throat radius. Nozzle A2, B2 and B3 are modified from the baseline designs by increasing the circular-arc throat radius while keeping all geometric parameters constant except for Θ and ϵ shown in Fig.6.1. (21). The design parameters which vary in this calculation are presented in Table 2.

Table 2. The Design Geometry Parameters for the Five Nozzles

Parameter	A1	A2	B1	B2	B3
Ae/At	1.09	1.09	1.80	1.80	1.80
L, cm	11.56	11.56	11.56	11.56	12.25
r_c	0.68	2.74	0.68	2.74	2.74
Θ, deg	20.84	22.33	20.84	22.33	20.42
ϵ, deg	1.21	1.21	10.85	11.24	10.85

Figure 6.1. (22) shows the five streamwise sections of the lower half parts of the nozzles. All the five nozzles have the same throat area. Nozzle A1 and A2 were calculated for half of the nozzles with the grid size of 101x31x51 and Nozzle B1,B2 and B3 for a quarter of the nozzles with the grid size of 67x31x31. Figs. 6.1. (23) to (27) are the pressure distributions of each nozzles at different locations, where L is the width of the nozzles. The calculated results compare well with the experiments. The pressures rise sharply in the vicinity of the throats. It is the tendency for the flow separation. But the flows do not separate for the five nozzles at the design conditions. The computational pressure distributions for A1 and A2 on the left and right walls

are almost exactly the same. This means that the flow field is symmetric about the center plane in the span wise direction. The span wise section velocity vector fields shown later also give this symmetry. It accords with the speculation. But the experimental data on the left and right side walls are not so symmetric near the throat as shown in Fig. 6.1. (23) and Fig. 6.1. (24). The reason is unknown yet. The effects of contouring occur in the upstream of the nozzle throat. Static pressures near the throat are generally higher for the contoured nozzles than for the baseline nozzles as shown in Figs. 6.1. (28) and (29). Figure 6.1. (30) is the Mach number distributions along the center lines of the nozzles which indicates that all the nozzles are choked at the throats. Contouring at the nozzle throat by increasing the circular-arc radius has a positive effect on the discharge coefficient. Figure 6.1. (31) shows that the discharge coefficients of A2 and B2 nozzles are higher than those of A1 and B1. The experimental discharge coefficient of B3 is less than that of B2 although they have the same value of throat radius. The inconsistency in the effect of throat radius on discharge coefficient is not yet understood. Comparison of calculated internal thrust ratio with the experimental F/Fi results is given in Fig. 6.1. (32) which indicates that throat radius, and therefore throat contouring, has no significant effect on thrust ratio. The average effect of throat contouring on the internal static pressure is negligible.

The flow fields are highly three-dimensional in the vicinities of the corners due to the boundary layer interaction between the side walls and the lower or upper walls, particularly after the throat, where the main flows are supersonic. At the design conditions, with the increase of the nozzle divergence angle, the secondary flow becomes weaker. Fig. 6.1. (33) shows the spanwise section velocity vector fields for

nozzle A1. Nozzle A1 is the same nozzle as the case 2 previously presented for the results of Euler equations. There are oblique shocks and reflections in the flow field. Fig. 6.1. (33) indicates that there is very weak secondary flow before the throat where the flow is subsonic and the secondary flow becomes much stronger after the throat where the flow is supersonic. Fig. 6.1. (33) (b), (c) , (d) and (e) show that the cross velocity vector fields are different at different locations. The cross flow is at the corners for Fig. 6.1. (33) (b) where the oblique shock wave after the throat just grows up. Fig. 6.1. (33) (c) shows that there exist cross flow near the center plane in y-direction. It is made by the shock wave and side wall boundary layers interactions, where the shocks from lower and upper wall intersect. After the shock intersection, the cross flow is again concentrated in the corners as shown in Fig. 6.1. (33) (d). Fig. 6.1. (34) presents the Mach number contours at different locations in z-direction. In the middle plane (Z/L=0.0), the shock wave and reflections are clearly seen. Near the two side walls, the shock intensity becomes weaker. Nozzle A1 is the only one containing shock waves in its flow field among the five nozzles. Fig. 6.1. (35) is a streamwise section velocity profile. There is no flow separation in the flow field. The transverse flows of nozzle A1 and A2 are stronger than those of B1, B2 and B3. This phenomenon can be seen from Fig. 6.1. (36) which shows the flow of a cross section of nozzle B2.

To test if the algorithm is grid size independent, two grid sizes of 51x21x21 and 101x31x51 were tested for Nozzle A2. The grids are highly stretched to test how tolerable the algorithm can be for the stretched grid. The maximum aspect ratio of the mesh for the grid of 51x21x21 is 1.2016×10^4 and for grid of 101x31x51 is 4.703×10^3. The program can stand even higher aspect ratios. The maximum CFL numbers used for grid 1 are $CFL_x = 7.1526 \times 10^3$, $CFL_y = 1.043 \times 10^7$ and $CFL_z =$

3.4785×10^4. For grid 2, $CFL_x = 2.679 \times 10^3$, $CFL_y = 1.8034 \times 10^5$, $CFL_z = 8.1857 \times 10^3$. CFL_x, CFL_y and CFL_z are the CFL numbers in x, y and z direction respectively. Fig. 6.1. (37) shows the convergence histories which indicate that similar convergence rates are obtained for the two cases. It seems that the algorithm is not grid size dependent. It may be true only for this case with simple geometry. As indicated in case 1 for the Euler equations, the URS algorithm is grid size dependent. 86 iterations are enough for the solution of grid 1 to be converged and 98 iterations are needed for grid 2. With the highly stretched grid 101x31x51, there exists at least 10 points in the boundary layer in the y direction and 7 points in the z direction. All the five cases have similar CFL number and convergency rate.

All the calculations are conducted on an IBM RISC 6000, Server 520. Due to the computer power limitation, the maximum grid size that can be used was about 101x31x51=159681. This grid size may still not be fine enough to analyze the 3D viscous flow fields in detail.

6.2 Results for the Flux Vector Splitting Scheme

To judge the viability of the new flux vector splitting scheme, 1D, 2D and 3D Euler equations were solved.

Case 1: 1D shock tube

Case 1 is a one-dimensional shock-tube flow. As a model problem, consider a tube of large extent in which a diaphragm separates a perfect gas at rest with different static pressures but at a uniform temperature. With the rupture of the diaphragm, an expansion propagates into the high-pressure gas, while a shock wave, followed by a contact discontinuity, propagates into the low-pressure gas. Details of this flow are described in standard texts (John 1984). In the present calculations, the initial pressure ratio across the diaphragm is taken as 10 to 1. The initial location of the diaphragm is taken at X/L = 7.0. To compare the present scheme with the others, Roe's flux difference splitting scheme, Van Leer's flux vector splitting scheme and Liou-Steffen's AUSM scheme were also used to solve the same 1D problem. All the solutions were calculated by using the explicit first order accuracy differencing. Figs. 6.2 (1) and (2) are the solutions of the present scheme with the CFL number 0.95. The solutions are monotone. A crisp shock profile is seen, while the contact discontinuity is composed of more grid zones. It is seen that the present scheme also gives good agreement with the exact solution for the expansion waves. The solutions of Roe's scheme are shown in Figs. 6.2. (3) and (4). The shock wave and the contact discontinuity profiles show no distinguishable difference between the solution of the present scheme and the Roe scheme. In comparing the results, the front of the expansion waves calculated by the present scheme is sharper than that of Roe's

scheme. It is noted however that the results of the both schemes agree well with the exact solution. Figs. 6.2. (5) and (6) show the results of Van Leer scheme when the CFL number is 0.95. The profiles of the shock and the discontinuity are basically the same as those of the present scheme and Roe scheme. But there are large spikes at the tail of the expansion waves for all the parameters. The computational experiments indicated that the spikes became less when the CFL number was decreased. The spikes basically disappeared when the CFL number was down to 0.45 at a loss of sharp shock profiles as can be seen in the Figs. 6.2. (7) and (8). Figs. 6.2. (9) and (10) present the results of the AUSM scheme. It was noted that the CFL number for AUSM scheme could not be greater than 0.4 for this 1D shock tube problem, otherwise the iteration became unstable. The maximum CFL number used in our calculation for the AUSM scheme was 0.35. Similarly, with Van Leer scheme when the CFL number was 0.45 as shown in Figs. 6.2. (7) and (8), both the shock and the contact discontinuities were somewhat diffused because the CFL number was far from the upper limit of the explicit scheme, CFL=1. As indicated in a text book by Hoffmann (1989), this is a common phenomenon for most of the differencing schemes. Among these four schemes tested for this 1D shock tube problem, only the present scheme and the Roe's scheme gave the most satisfactory results.

Case 2: transonic inlet-diffuser

Case 2 is a 2D transonic Inlet-diffuser shown in Fig. 6.2. (11) designed and studied by Bogar et al. (Bogar & Sajben & Kroutil 1981). It is a 3D diffuser that can also be treated as 2D. It contains a normal shock wave in the downstream of its throat. The calculation was implemented first using first order differencing on the streamwise plane as a two dimensional case. The explicit two-stage method (Liou &

Hsu 1989) was used for the present scheme and AUSM scheme and the 2D implicit upwind-relaxation method for the Van Leer scheme (Zha & Liu & Ma 1989). Because the implicit operator with the first order differencing was used for the Van Leer scheme, the calculation only converged for the RHS with first and third order accuracy differencing. Therefore the results of Van Leer scheme will be presented only for the first and third order differencing. Fig.6.2. (12) shows the Mach number distributions along the bottom and top walls. It is seen that the shock profiles are very sharp. The Mach number transition from the supersonic peak to the subsonic bottom takes only one grid width for both the present and the AUSM scheme. The Van Leer scheme needs two transition zones. All these three shock profiles are monotone without oscillations, overshoots or undershoots. But as mentioned before, because the pressure splitting is not continuously differentiable at the sonic point for the present and the AUSM scheme, a glitch appears at the sonic point position as Fig.6.2. (12) shows. In contrast, the Van Leer scheme obtains the smooth transition at the sonic point. Fortunately, this drawback can be removed automatically by using higher order differencing as it will be seen later. Fig. 6.2. (13) presents the pressure contours of the flow field. The present and the AUSM scheme gives the sharper normal shock than the Van Leer scheme. The glitch at the sonic point was not revealed in the report of Liou and Steffen (Liou & Steffen 1991) who used the AUSM scheme with a second order differencing, except one case with a first order differencing, which was quasi two-dimensional. The latter was not suitable to show the glitch.

In the next step, to see the performance of the present scheme for higher order differencing, calculations were carried out using a second order differencing.

MUSCL- type flux differencing (Anderson & Thomas & Van Leer 1986) is used to evaluate the flux passing through the interface of a cell for the higher order differencing. Again the explicit two-stage method was used for both the present and the AUSM scheme. Fig.6.2. (14) shows the Mach number distributions using the fully upwind second order scheme. It is seen that both the present and the AUSM scheme obtains the smooth transition at the sonic point and the glitch disappears. Furthermore, the shock profiles remain monotone without using any smooth limiters. The shock transition is almost in one zone at the top but it is two transition zones at the bottom. Fig.6.2. (15) shows the pressure contours of the flow fields obtained by using the two schemes. It is seen that two pressure fields are almost indistinguishable and the shocks are sharp at the top and also at the bottom but with two zones.

To see the results with still higher order differencing, computations were carried out with third order biased upwind schemes. These results are obtained from the three-dimensional solver using the URS algorithm with the nonuniform grid in the 3D inlet-diffuser as shown in Fig.6.2. (16). The computations were carried out in 3D, however the results are presented only for the central plane since the section is rectangular in spanwise direction and the results are nearly the same. In Fig.6.2. (16), the bottom of the diffuser is shown at the top so that the geometry can be seen better. The lower figure shows the typical section in streamwise direction. The Mach number distributions along the top and bottom walls are presented in Fig.6.2. (17). It can be observed that with all three schemes, oscillations appear in the vicinity of shock as expected (Anderson & Thomas & Van Leer 1986). The oscillation amplitude of present scheme (Z/B) is the smallest among the three schemes and those of the AUSM and Van Leer are almost the same. The smaller oscillation

amplitude of the present scheme may be due to the fact that the present scheme is a Mach number polynomial of degree one, the lowest degree. The other two schemes are necessarily of degree two. The oscillations may be removed by using some smooth limiters to switch the scheme to lower differencing order at the shock location as many researchers have done in the past (Anderson & Thomas & Van Leer 1986, Liou & Hsu 1989). Such work is not done in this thesis. Once again, it can be seen in Fig.6.2. (17) that a smooth transition at the sonic point is obtained by using a third order differencing and one transition zone shock profiles are obtained for all three schemes. In fact, the results of the present scheme completely agree with those from Van Leer and AUSM except for the shock oscillations. The Mach number contours of the flow fields are presented in Fig. 6.2. (18). It is seen that all three look very similar with sharp shock waves. In comparison with Figs.6.2. (13) and (15), some closed iso-Mach number lines appear at the top just before the shock waves, which are caused by the oscillations near the shock. It is also clear that the Van Leer scheme with third order differencing produces sharper shock wave than the one with a first order differencing in Fig. 6.2. (13). Fig. 6.2. (19) is the convergency histories for the three-dimensional calculations of the inlet-diffuser. Single precision was used for the 3D calculations and the residuals were reduced to 10^{-6}. It is seen that the convergence rate of the Van Leer scheme is the best showing its advantage. Those of the present and AUSM schemes are almost the same, with time steps double that of the Van Leer scheme. For this case, the present scheme is a little faster than AUSM scheme. To see the convergence history with a third order accuracy in a 2D case, calculations were also carried out by using the upwind-relaxation algorithm for the two-dimensional grid shown in Fig.6.2. (11). Double precision was used and the residual was reduced to machine zero as shown in Fig. 6.2. (20). It is seen that after

10^{-5} accuracy, the residual decreases continuously, which shows the present scheme converges without computational difficulties for this case.

Case 3. Transonic Nozzle

Case 3 is a study on a rectangular converging-diverging nozzle shown in Fig. 6.2. (21). Due to symmetry, it is sufficient to study a one quarter of the nozzle shown in the figure. Although this nozzle is three dimensional, it behaves almost like a 2D case for the variation in the spanwise direction is small. However, it is again a case solved by using three dimensional Euler equations and the results can be compared to experimental ones, in particular pressure distributions at various planes (Mary et al. 1980). It is noted that there is no shock for this case. The computations were carried out by using the URS algorithm with third order differencing for all three schemes and the results are compared. The Mach number distributions along the center-line of the nozzle are presented in Fig. 6.2. (22) and the Mach number contours on the central plane in Fig. 6.2. (23). Fig. 6.2. (22) shows again that the present scheme completely agrees with Van Leer and AUSM scheme and the sonic transition is smooth. Fig. 6.2. (23) shows that the Mach contours are very similar with no discernible differences. Fig. 6.2. (24) is the pressure distributions of the nozzle at different spanwise locations. First three figures on the top are on the bottom wall of the nozzle and the last at the center-line as indicated in Fig. 6.2. (24). The results generally agree favourably with the experiment (Mary et al. 1980). The pressure distributions at and near the central plane (Z/L = 0.0 and 0.45) agree with the experiment better than that at Z/L = 0.875. It may be because the real flow near the central plane mainly behaves as two-dimensional flow. When it is near the side wall (Z/L = 0.875), the interactions of the side wall boundary layers cause a strong

three-dimensional effect, which can not be captured by using the 3D Euler equations. The disagreement is mainly at the throat where the flow has the tendency to separation. Similar results is seen on the last figure in Fig. 6.2. (24), which illustrates the pressure distribution along the side wall center-line. Fig. 6.2. (25) shows the convergency histories of the transonic nozzle with the grid of 101 x 31 x 31. It is seen that for this case the present scheme is about 15% faster than AUSM and 70% slower than Van Leer scheme.

CONCLUSIONS

An Upwind Relaxation-Sweeping (URS) algorithm for three dimensional compressible Euler and Navier-Stokes equations has been developed in this thesis. The linear stability analysis shows that the unfactored Upwind Relaxation-Sweeping algorithm is unconditionally stable. The algorithm is independent of the global sweeping direction selection. Further, by choosing the direction with relatively low variable gradient as the global sweeping direction, the algorithm can have a higher degree of stability. Because of no approximation error introduced, the URS algorithm can reach very high CFL number,up to the order of 10^6 for the maximum CFL number, and therefore obtain very rapid convergence rate. The memory requirement is greatly reduced since the Jacobians are only stored in one iterating plane. In addition, the CPU time per time step is saved because one global sweep is able to solve all the unknowns in the entire flow field.

The three-dimensional compressible Euler equations are solved by the URS algorithm to study the internal flows of a non-axisymmetric nozzle with a circular-to-rectangular transition ducts. The cases with and without entrance swirl flow were calculated. The results agree well with the experiments. It is found that transverse stream division lines move to the right on the upper wall and to the left on the lower wall for the flow with entrance swirl. The computational experiments show that the URS algorithm is grid size dependent. For the case of a non-axisymmetric nozzle with shock reflections and intersections, the computational results also agree well with the experiment. A 3D channel with complex shock wave structures has also been calculated. The shock wave structure varies with different back pressures. The

calculated shock wave structure has deviations from the experimental results mainly because an inviscid flow model is used and an accurate back pressure is not available. The results show that the URS algorithm is efficient and robust.

Five nonaxisymmetric converging-diverging nozzles at design conditions were calculated by solving the three-dimensional Navier-Stokes equations using the URS algorithm. Rapid convergency rates have been obtained for the calculations. The calculations are to study the nozzle internal-performance effect of throat contouring as a result of increasing the circular-arc throat radius. Throat contouring resulted in a positive effect on discharge coefficient but showed no significant improvement in internal thrust ratio. The average effect of throat contouring on the internal static pressures is negligible. All the computational results presented as static-pressure distributions, discharge coefficients and internal thrust ratios have been compared with the experiments and they are in good agreement. The computer code developed in the study can be used as an effective tool for the nozzle design.

A new flux vector splitting scheme with low numerical diffusion has been suggested in this thesis. This scheme uses the velocity component normal to the volume interface as the characteristic speed and yields the vanishing individual mass flux at the stagnation. The numerical dissipation for the mass and momentum equations vanishes with the mass flux. One of the diffusive term of the energy equation does not vanish at the stagnation. But the diffusion is within the magnitude order of truncation error. The low numerical diffusion for viscous flows may be ensured further by using higher-order differencing. Consequently, for the viscous flows, the present scheme may be more accurate than the flux vector splitting schemes without the mass flux vanishing at the stagnation. The scheme with the Mach number polynomial of degree one, the natural and lowest degree, is very

simple and easy to be implemented.

The scheme has been tested to solve 1D, 2D and 3D Euler equations. The solutions are monotone and the normal shock wave profiles are crisp. For a 1D shock tube problem with the shock and the contact discontinuities, the present and Roe schemes using the first order differencing gave the most satisfactory results compared with those from Van Leer and Liou-Steffen's AUSM schemes. For the multidimensional transonic flows, the sharp monotone normal shock wave profiles with mostly one transition zone are obtained. A glitch appears at the sonic point when the first order differencing is used for the transonic inlet-diffuser. But the glitch can be automatically removed by using a higher order differencing. The scheme converges well for the tested cases, slightly faster than AUSM scheme and slower than Van Leer scheme. Generally, for the tested transonic flows, the results agree completely with the AUSM scheme and Van Leer scheme. However, using a third order differencing, the present scheme produces results with least oscillations near the shock. For a transonic nozzle, the results calculated from the present scheme agree well with the experiment.

REFERENCES

ANDERSON, W.K., THOMAS, J.L., and VAN LEER, B., 1986, " Comparison of Finite Volume Flux Vector Splittings for the Euler Equations", AIAA Journal, Vol. 24, No.9, pp. 1453-1460

BERRIER, Bobby L., PALCZA, J. Lawrence and RICHEY, G. Keith, 1977, " Nonaxisymmetric Nozzle Technology Program, An Overview", AIAA Paper 77-1225

BRILEY, W.R. and MCDONALD, H., 1976, " Solution of the Multidimensional Compressible Navier-Stokes Equations by a Generalized Implicit Mehtod." Journal of Computational Physics, Vol. 24, pp. 372-385

BEAM, R.M., and WARMING, R.F., 1978 " An Implicit Factored Scheme for the Compressible Navier-Stokes Equations", AIAA Journal, Vol. 16, No.4, pp. 393-402

BERGAMINI, L., and CINNELLA, P., 1993, " A Comparison of "New" and " Old" Flux-Splitting Schemes for the Euler Equations " AIAA Paper 93-0876

BENAY, R., DÉLERY, J. and POT, T., 1986, " Etude Expérimentale d'une interaction onde de choc-couche limite en canal tridemensionnel. Propriétés du champ moyen., ONERA Rapport Technique no 70/7078 AN

BEYER, William H., ed. 1978, " CRC Standard Mathematical Tables", 25th ed. CRC Press, Inc.

BOGAR, T.J., SAJBAN, M. and KROUTIL, J.C., 1981, "Characteristic Frequency and Length Scales in Transonic Diffuser Flow Oscillations", AIAA Paper 81-1291

BURLEY, II, J.R., BANGERT, L. S., and CARLSON, J. R., 1986 " Static Investigation of Circular-to- Rectangular Transition Ducts for High-Aspect-Ratio Nonaxi-Symmetric Nozzles", NASA Technical Paper 2534

CANDLER, G.V., and MACCORMACK, R. W., 1987," Hypersonic Flows Past 3-D Configurations," AIAA Paper 87-0480

CHAKRAVARTHY, S.R., 1984, "Relaxation Methods for Unfactored Implicit Schemes," AIAA Paper 84-0165

COIRIER, W. J. and VAN LEER, B., 1991 "Numerical Flux Formulas for the Euler and Navier-Stokes Equations: II. Progress in Flux-Vector Splitting", AIAA Paper 91-1566-CP

CAMBIER, L. and ESCANDE, B., 1990 " Calculation of a Three-Dimensional Shock Wave-Turbulent Boundary-Layer Interaction", AIAA Journal No. 11, pp. 1901-1908

EDWARDS J. R., and MCRAE D. S., 1993 " Nonlinear Relaxation Navier-Stokes Solver for Three-Dimensional, High-Speed Internal Flows", AIAA Journal, Vol. 31, No. 7, pp. 1222-1228

GODUNOV, S.K., 1959 " A Finite Difference Method for the Numerical Computation of discoutinuous Solutions of the Equations of Fluid Dynamics", Mat. Sb. 47: 271-306

HANEL, D., SCHWANE, R., 1987, " Computation of hypersonic Viscous Flow", 1st Joint Europe-US Short Course on Hypersonics, Dec. 7-11, 1987, Paris- France.

HANEL, D and SCHWANE, R., 1989, " An Implicit Flux-Vector Splitting Scheme for the Computation of Viscous Hypersonic Flow", AIAA Paper 89-0274

HARTEN, A., LAX, P.D. and VAN LEER, B., 1983, "On Upstream Differencing and Godunov-Type Schemes for Hyperbolic Conservation Laws", SIAM Review, Vol. 25, No. 1, pp. 35-61

HARTEN, A. and LAX, P., 1981 " A Random Choice Finite Difference Scheme for Hyperbolic Conservation Laws," SIAM J. Numer. Anal., Vol. 18, pp. 289-315

HART, John F., CHENEY, E. W., LAWSON, Charles L, MAEHLY, Hans J., MESZTENYI, Charles K., RICE, John R., THACHER, Henry G., Jr., and WITZGALL, Christoph, 1968, " Computer Approximations", John Wiley & Sons, Inc., pp. 130-136

HOFFMANN, Klaus A., 1989, " Computational Fluid Dynamics for

Engineers", Engineering Education System™

JAMESON, A., SCHMIDT, W., and TURKEL, E., 1981, " Numerical Solutions of the Euler Equations by Finite Volume Method Using Runge-Kutta Time Stepping Schemes", AIAA Paper 81-1259

JAMESON, A. and TURKEL,E., 1981, " Implicit Schemes and the LU Decompositions", Mathematics and Computation, Vol. 37, pp. 385-390

JOHN, James E. A., 1984, " Gas Dynamics", Allyn and Bacon, Inc.

LAX, P.D. and WENDROFF, B., 1960 " Systems of Conversation Laws," Comm. Pure. App. Math.. Vol. 13, pp. 217-237

LAX, P.D. and WENDROFF, B., 1964, " Difference Schemes for Hyperbolic Equations with High Order Accuracy," , Comm. Pure. App. Math.. Vol. 17, pp. 381-398

LIOU, M.-S., and STEFFEN, C. J., 1991, "A New Flux Splitting Scheme", NASA TM 104404

LIOU, M.S. and STEFFEN Jr, C., 1991, "High Order Polynomial Expansions for Flux Vector Splitting", Proceedings of the International Conference on Computational Engineering Science

LIOU, M.-S. and HSU, A.T., 1989, " A Time Accurate Finite Volume High Resolution Scheme for 3D Navier-Stokes Equations", AIAA Paper 89-1994,

MACCORMACK, R.W., 1969, " The Effect of Viscoscity in Hypervelocity Impact Catering", AIAA Paper 69-345

MACCORMACK, R. W., 1985, " Current Status of Numerical Solutions of the Navier-Stokes Equations," AIAA Paper 85-0032

MACCORMACK, R. W., 1990, " Solution of the Navier-Stokes Equations in Three Dimensions", AIAA Paper 90-1520

MCMASTER, D.L., Shang, J.S., and Gaitonde, D., 1989, " A Vectorized Gauss-Seidel Line Relaxation Scheme for Solving 3D Navier-Stokes Equations", AIAA Paper 89-1948-CP

MORETTI, G., 1987, " Computation of Flows with Shocks", Annual Review

of Fluid Mechanics, vol.19, pp. 313-337

MASON, Mary L., PUTNAM, Lawrence E. and RE, Richard J., 1980, " The Effect of Throat Contouring on Two-Dimensional Converging-Diverging Nozzles at Static Conditions", NASA TP-1704

NAGASU, H and FUJII, K, 1990, " Computationtal Methods in Viscous Aerodynamics", Chapter 9, Elservier Science Publishers BV

PAOLETTI, S., VITALETTI, M., and STOW, P., 1992, " An Unfactored Implicit Scheme for 3D inviscid Transonic Flows", AIAA Paper 92-2668

PULLIAM, T., 1986, " Efficient Solution Methods for the Navier-Stokes Equations", Numerical Techniques For Viscous Flow Computations in Turbomachinery Bladings, VKI LS-86

RAI, M. M., and CHAKRAVARTHY, S. R., 1986, " An Implicit Form for the Osher Upwind Scheme", AIAA Journal, Vol. 24, No.5, 735-743

ROE, P.L., 1981, "Approximate Riemann Solvers, Parameter Vectors, and Difference Scheme." Journal of Computational Physics, Vol. 43, pp. 357-372

ROE, P., 1984,"Generalized Formulation of TVD Lax-Wendroff Schemes." NASA CR 172478

STEGER, J. L., WARMING, R. F., 1981 " Flux Vector Splitting of the Inviscid Gasdynamic Equations with Applicstion to Finit Difference Methods", Journal of Computational Physics, Vol. 40, pp. 263-293

SIMPSON, L. B., and WHITFIELD, D. L., 1992 " Flux-Difference Split Algorithm for Unsteady Thin-Layer Navier-Stokes Solutions", AIAA Journal, Vol.30, No.4, pp. 914-922

STEVENS, H.L., THAYER, E.B., and FULLERTON, J. F., 1981 " Development of the Multi-Function 2-D/C-D Nozzle. AIAA Paper 81-1491

TAYLOR III, A. C., NG, W.-F., and WALTERS, R. W., 1992 " Upwind Relaxation Methods for the Navier-Stokes Equations Using Inner Iterations ", Computational Physics, Vol. 99, pp. 68-78

THOMAS, J.L., and WALTERS, R.W., 1985, " Implicit Flux-Split Scheme for the Euler Equations", AIAA Paper 85-1680

THOMAS, J.L., and WALTERS, R.W., 1987, " Upwind Relaxation Algorithms for the Navier-Stokes Equations", AIAA Journal, Vol. 25, No.4, pp. 527-534

THOMAS, J.L., VAN LEER, B. and WALTERS, R.W., 1990, "Implicit Flux-Split Schemes for the Euler Equations", AIAA Journal, Vol. 28, No. 6, 973-974

THOMAS, J.L. and WALTERS, R.W., 1990, " Computational Methods in Viscous Aerodynamics ", Chapter 5, Elsevier Science Publishers BV

VAN DAM, C.P.,and HAFEZ, M, 1989, " Comparison of Iterative and Direct Solution Methods for Viscous Flow Problems", AIAA Journal Vol. 27, No. 10, pp. 1459-1461

VATSA,V.N., THOMAS,J.L., and WEDAN, B.W., 1987, " Navier-Stokes Computation of Prolate Spheroids at Angle of Attack", AIAA Paper 87-2627

VAN LEER, B., 1982, " Flux-vector splitting for the Euler equations", Lecture Note in Physics, Vol. 170, pp. 507-512

VAN LEER,B., Thomas, J.L., Roe, P.L. and Newsome, R.W, 1987, " A Comparison of Numerical Flux Formulas for the Euler and Navier-Stokes Equations", AIAA Paper 87-1104

VAN LEER, B., 1990, "Flux Vector Splitting for the 1990's", Invited Lecture, NASA Lewis Research Center

ZHA, G.C., LIU,D.Z., and MA,T.U., 1989, "An Efficient Upwind/Relaxation Algorithm for the Euler and Navier-Stokes Equations", International Journal for Numerical Methods in Fluids, Vol. 9, No.5, pp. 517-529

ZHA, G.C. and BILGEN, E., 1992, "Effect of Throat Contouring on Two-Dimensional Converging-Diverging Nozzles Using URS Method" AIAA Paper 92-2659

ZHA,G.C. and BILGEN, E., 1992, " An Efficient Upwind Relaxation-Sweeping Algorithm for Three-Dimensional Navier-Stokes Equations" AIAA Paper 92-0023

ZHA,G.C. and LIU, D.Z., 1990, " An Efficient Upwind Relaxation-Sweeping Algorithm for Three-Dimensional Euler Equations", AIAA Paper 90-0129

ZHA,G.C, and BILGEN, E., 1993, " Nnmerical Study of Three-Dimensional Using Unfactored Upwind-Relaxation Sweeping Algorithm " (Submitted to Journal of Computational Physics)

ZHA,G.C, and BILGEN, E., 1994, " Nnmerical Simulation of Three-Dimensional Inviscid Internal Flows Using Unfactored Upwind-Relaxation Sweeping Algorithm " AIAA Paper 94-0396

ZHA, G.C. and BILGEN, E., 1993, " A New Flux Vector Splitting Scheme", CASI 4th Aerodynamics Symposium, Toronto, Canada, May 4-5

ZHA, G.-C. and BILGEN, E., 1993, " Numerical Solutions of Euler Equations by Using a New Flux Vector Splitting Scheme", International Journal for the Numerical Methods in Fluids, Vol. 17, pp. 115-144

APPENDIX A NONDIMENSIONAL VARIABLES

The normalization of the governing equation (1) is obtained by using the following nondimensional variables:

$$\bar{x}=\frac{x}{L} \quad , \quad \bar{y}=\frac{y}{L} \quad , \quad \bar{p}=\frac{p}{\rho_\infty u_\infty^2} \quad , \quad \bar{e}=\frac{e}{\rho_\infty u_\infty^2} \quad ,$$

$$\bar{u}=\frac{u}{u_\infty} \quad , \quad \bar{v}=\frac{v}{u_\infty} \quad , \quad \bar{w}=\frac{w}{u_\infty} \quad , \quad \bar{\rho}=\frac{\rho}{\rho_\infty} \quad ,$$

$$\bar{t}=t\frac{u_\infty}{L} \quad , \quad \bar{T}=C_p\frac{T}{u_\infty^2} \quad ,$$

To keep the state equation the same form, the gas constant and the specific heats also have to be normalized:

$$\bar{C}_p=\frac{C_p}{C_p} \quad , \quad \bar{C}_v=\frac{C_v}{C_p} \quad , \quad \bar{R}=\frac{R}{C_p}$$

The normalization of the viscous terms are as the following:

$$\bar{\tau}_{xx}=\frac{\tau_{xx}}{\rho u_\infty^2} \quad , \quad \bar{\tau}_{yy}=\frac{\tau_{yy}}{\rho u_\infty^2} \quad , \quad \bar{\tau}_{zz}=\frac{\tau_{zz}}{\rho u_\infty^2} \quad ,$$

$$\bar{\tau}_{xy}=\frac{\tau_{xy}}{\rho u_\infty^2} \quad , \quad \bar{\tau}_{yz}=\frac{\tau_{yz}}{\rho u_\infty^2} \quad , \quad \bar{\tau}_{xz}=\frac{\tau_{xz}}{\rho u_\infty^2} \quad ,$$

$$\bar{\mu}=\frac{\mu}{\mu_\infty} \quad , \quad \bar{\lambda}=-\frac{2}{3}\bar{\mu}$$

$$Re=\frac{u_\infty L \rho_\infty}{\mu_\infty} \quad , \quad Pr=\frac{C_p \mu_\infty}{k}$$

To express the variables conveniently, the bars representing the nondimensional parameters are omitted in the governing equations from Eq. 1 to 13 in Chapter II.

APPENDIX B METHOD OF CALCULATING CIRCULAR-TO-RECTANGULAR TRANSITION SURFACES

The method of calculating circular-to-rectangular transition surfaces give by Burley (Burley & Bangert & Carlson 1986) is presented here for reference.

A circle, an ellipse, and a rectangle are all specific cases of superellipses. The locus of points which make up a superellipse is defined by the equation

$$\left(\frac{y}{a}\right)^{\eta} + \left(\frac{z}{b}\right)^{\eta} = 1 \qquad \text{(A1)}$$

The area enclosed by the superellipse A_{cs} can be computed from the following equation (Beyer 1978):

$$A_{cs} = \frac{\Gamma(1/\eta)^2 4ab}{(\Gamma(2/\eta)\cdot 2\eta)} \qquad \text{(A2)}$$

where Γ refers to the " gamma function" and is defined as

$$\Gamma(\eta) = \int_0^{\infty}(e^{-t}t^{\eta-1})dt \qquad (\eta > 0) \qquad \text{(A3)}$$

Calculation of the gamma function is addressed by Hart et al (1968)

With A_{cs} , a and b defined as continuous analytic functions of x (axis distance from the entrance), the transition surface is determined by iteratively computing $\eta(x)$

from Eq. (A2). For practical applications, a rectangle ($\eta = \infty$) can be accurately approximated with $\eta \geq 50$. In this thesis, $\eta \geq 100$ is used to represent a rectangle.

The axes for duct 1 are determined by the following equations

$$a(x) = r - (r-w)(x/l)^2[3-2(x/l)] \tag{A4}$$

$$b(x) = r - (r-h)(x/l)^2[3-2(x/l)] \tag{A5}$$

where r is the radius of entrance circle, w the width and h the hight of exit rectangle, l the transition duct length. These equations have zero first derivatives with respect to x at x=0 and x=l; therefore, a smooth transition is formed.

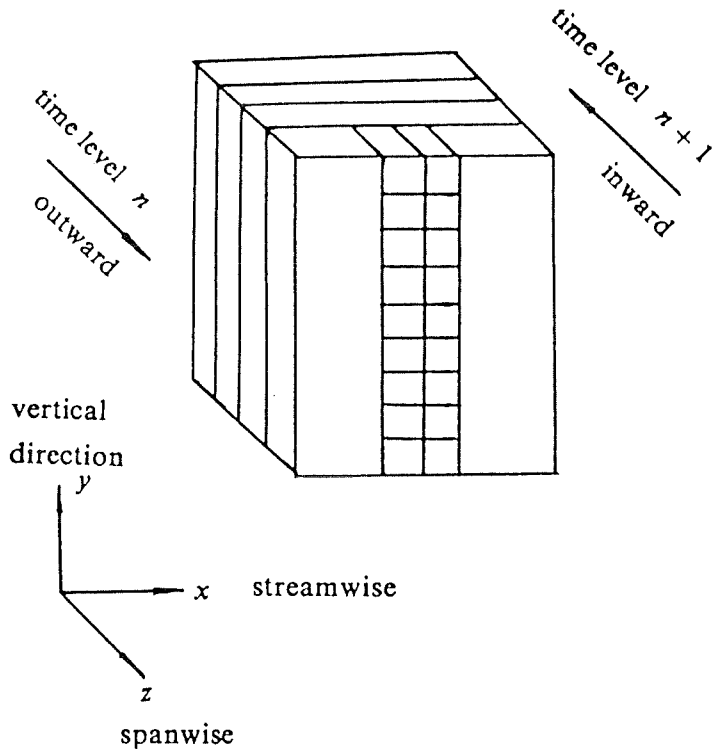

Fig. 4. (1) The sketch of the global sweeping for URS algorithm

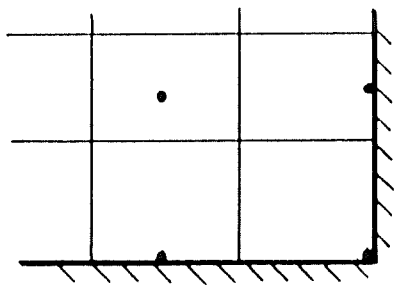

Fig. 4. (2) The wall boundary condition treatment for 3D Navier-Stokes equations

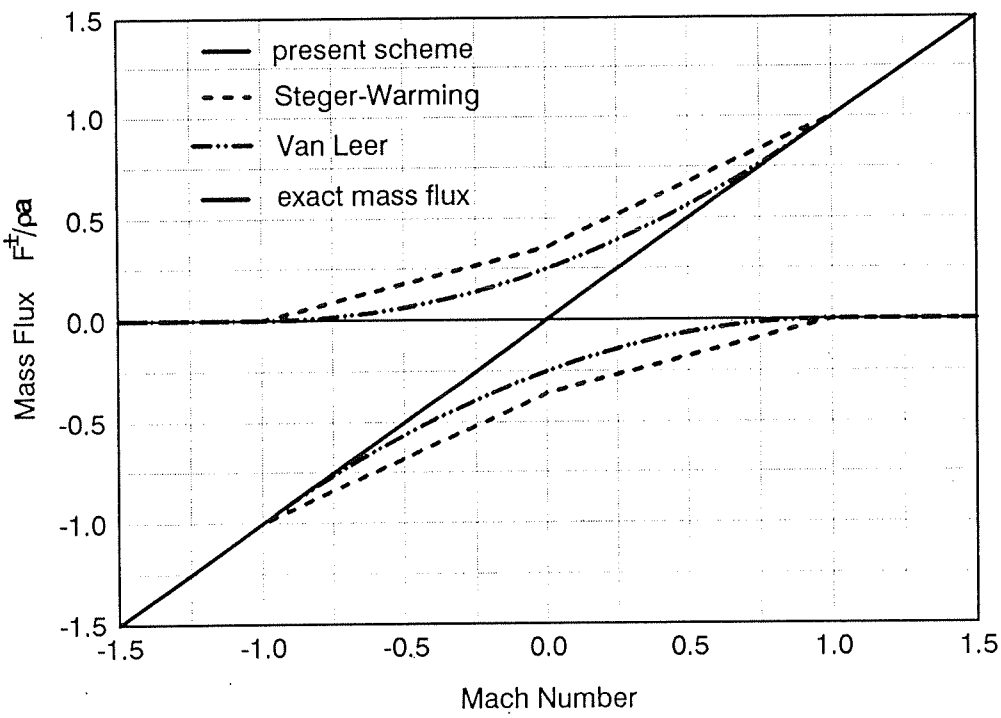

Fig. 5. (1) Mass flux of the flux vector splitting schemes

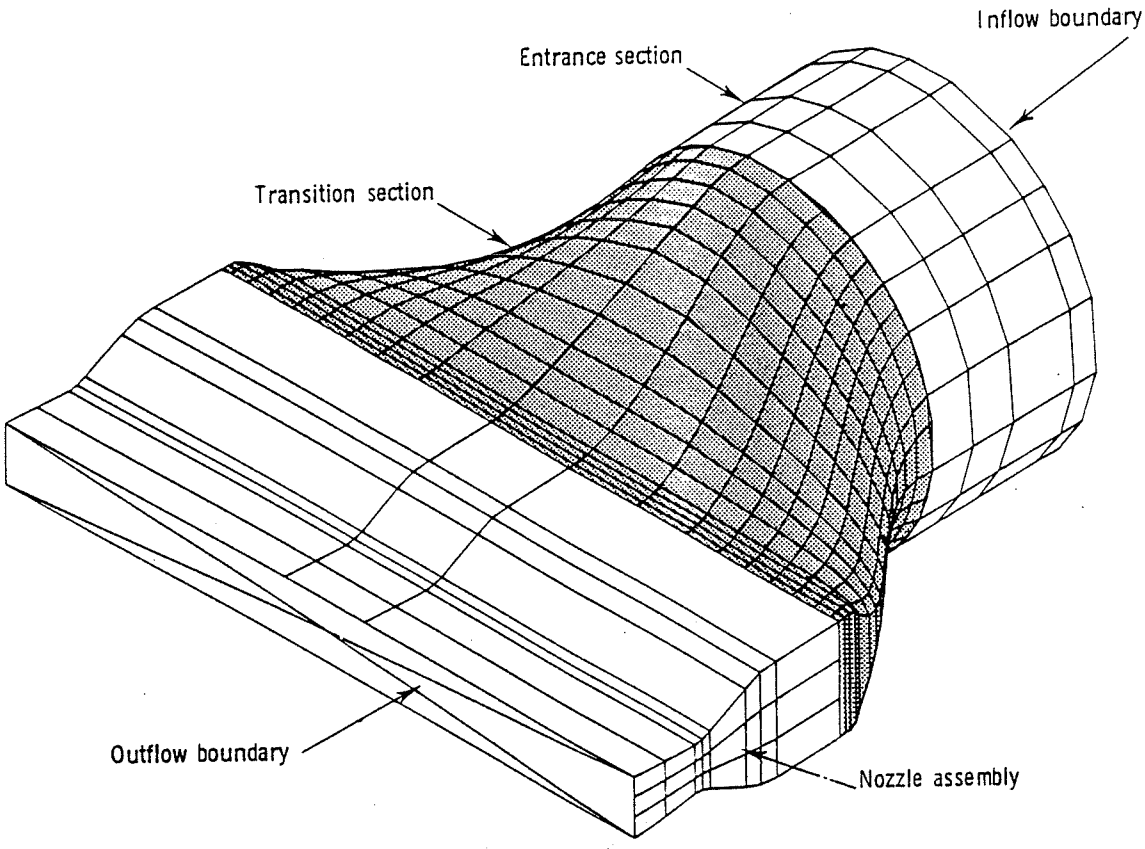

Fig. 6.1. (1) The sketch of a transition duct with a nozzle

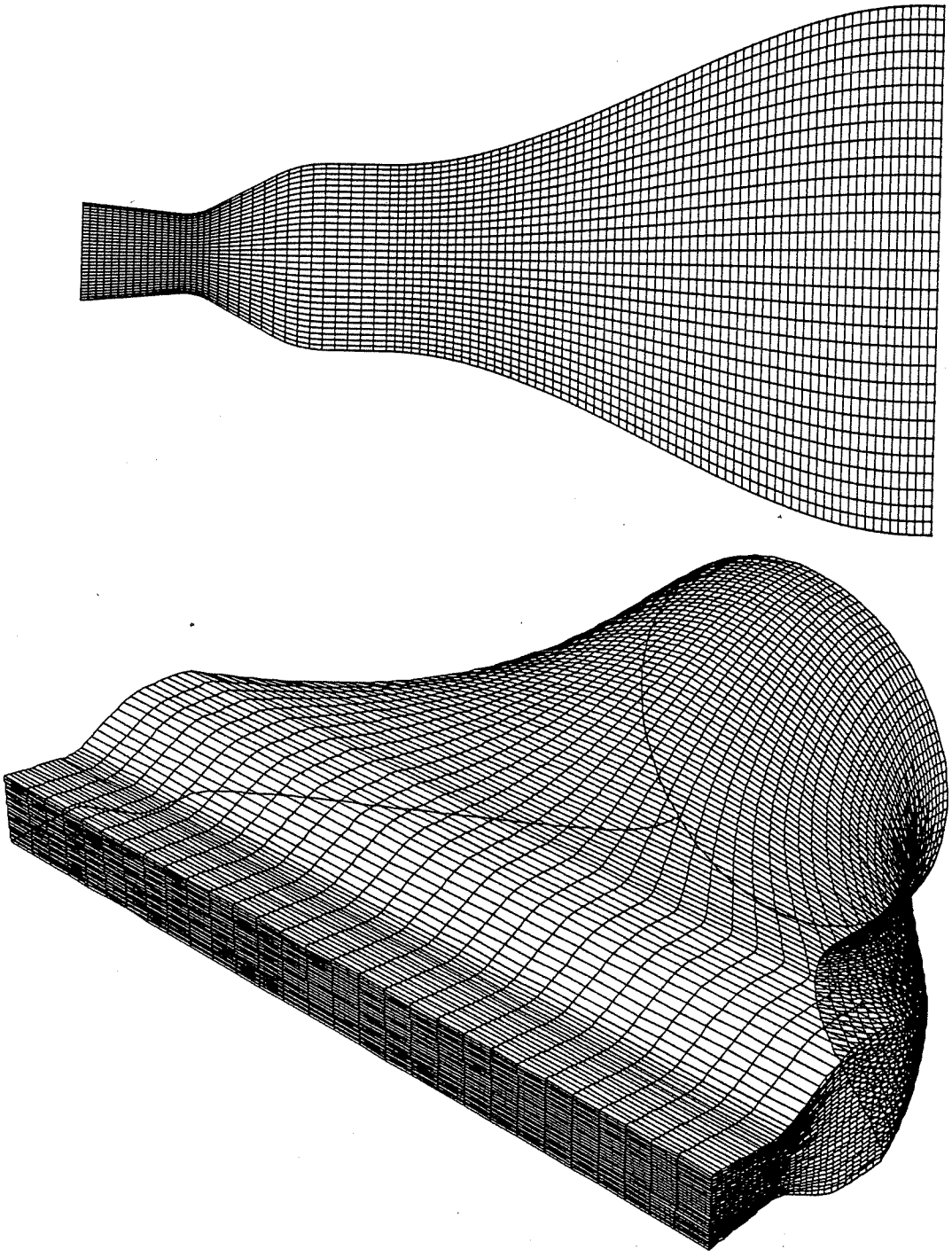

Fig. 6.1. (2) The geometry and the grid of the transition duct 1 with the nozzle, grid size 101x31x31.

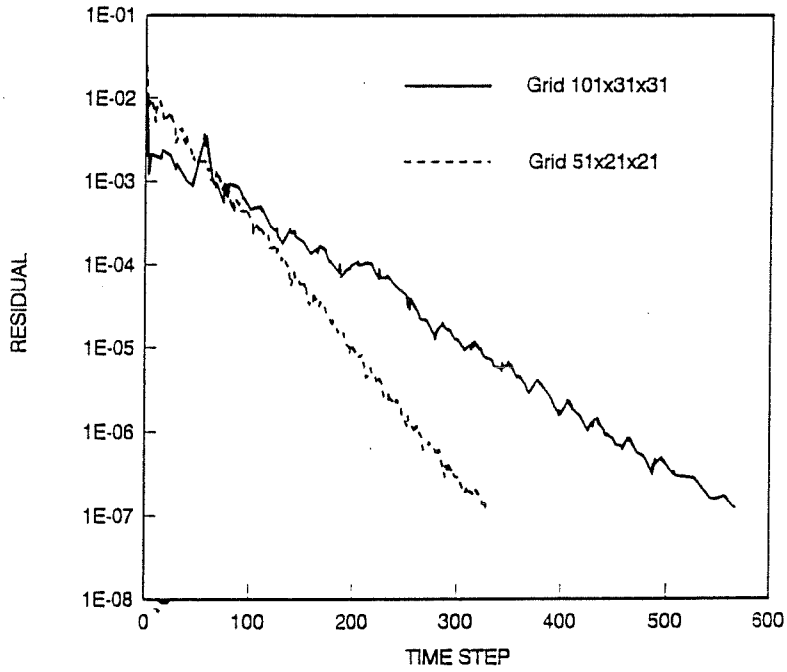

Fig. 6.1. (3) The convergency histories of the transition duct 1 with the nozzle

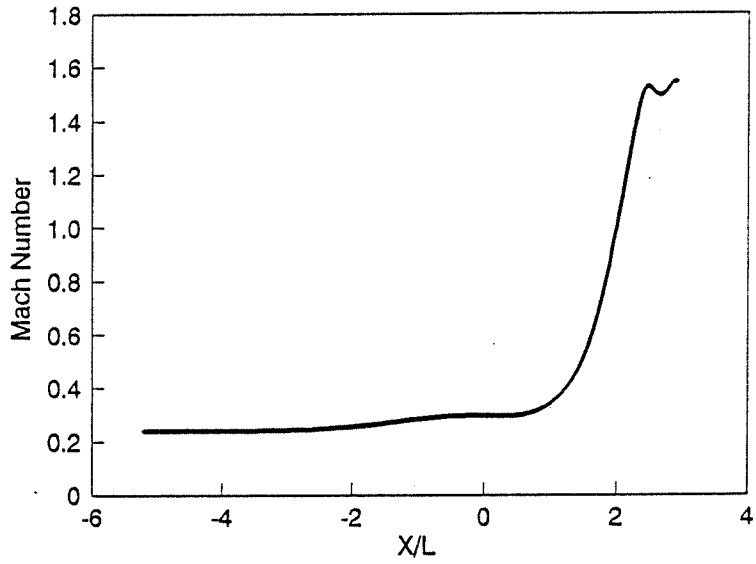

Fig. 6.1. (4) The Mach number distribution along the center line of the duct and the nozzle

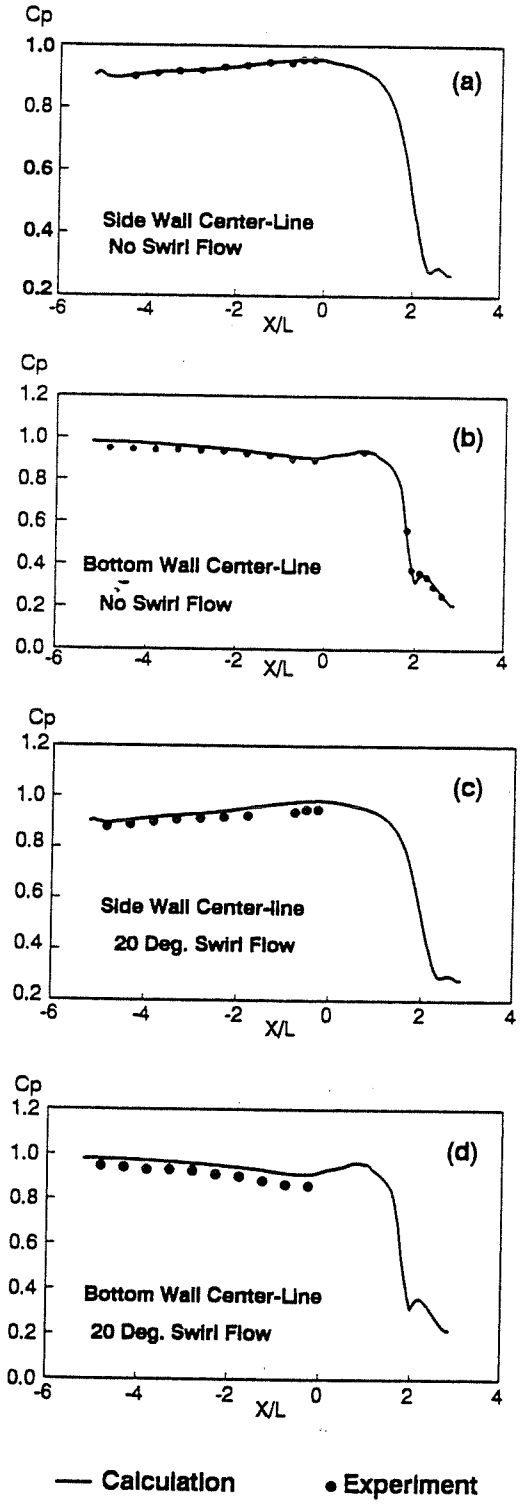

Fig. 6.1. (5) Pressure distributions of the duct 1 and the nozzle

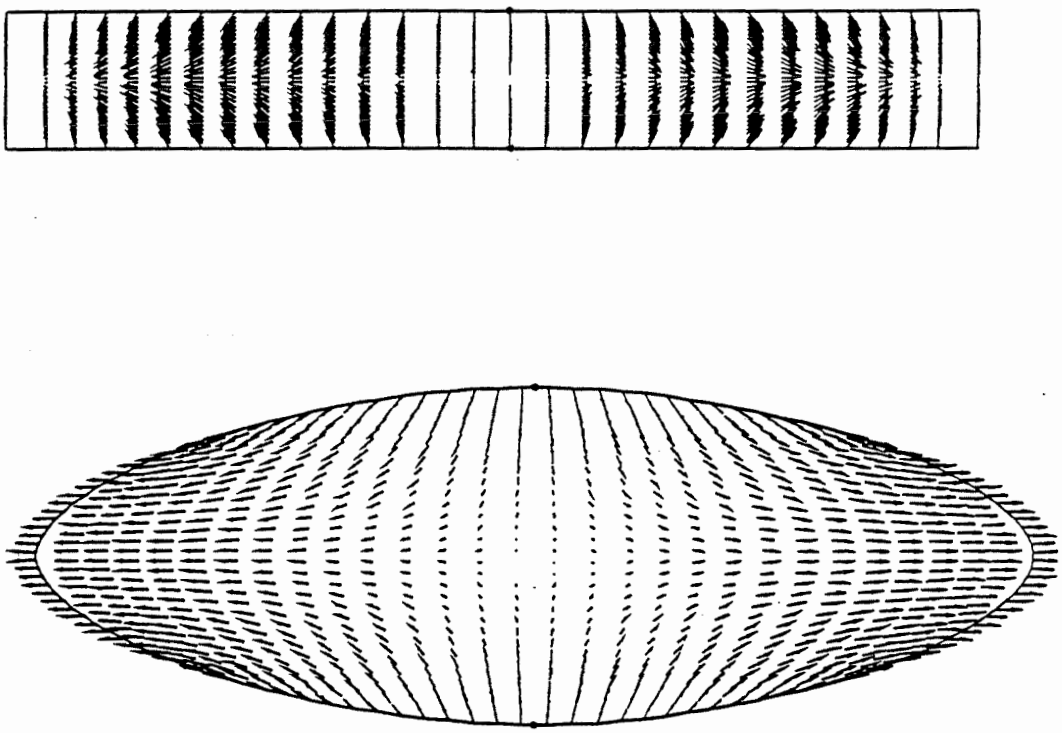

Fig. 6.1. (6) The velocity fields of the cross sections with no entrance swirl

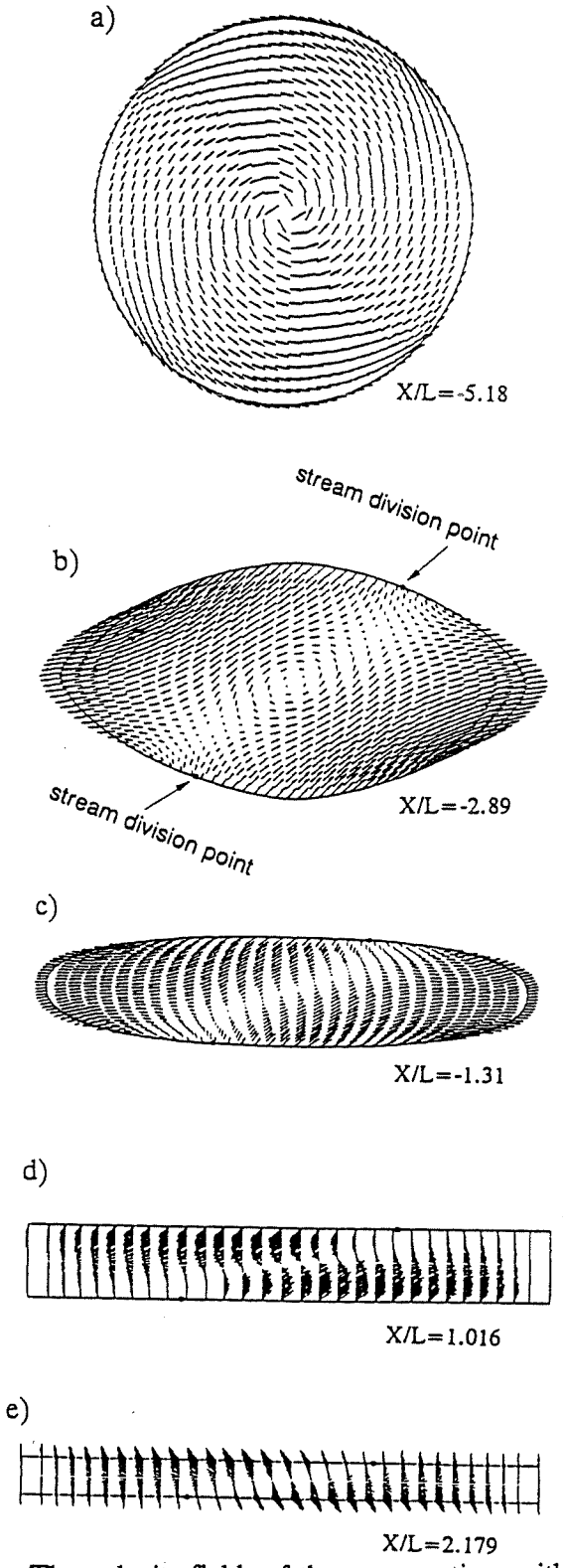

Fig. 6.1. (7) The velocity fields of the cross sections with entrance swirl

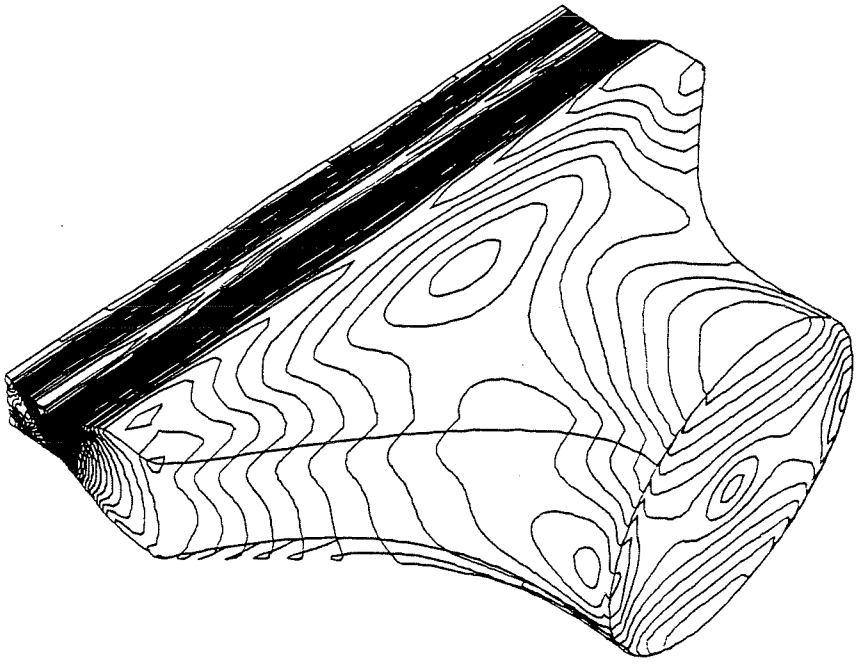

Fig. 6.1. (8) The Mach number contours of transition duct 1 and the nozzle

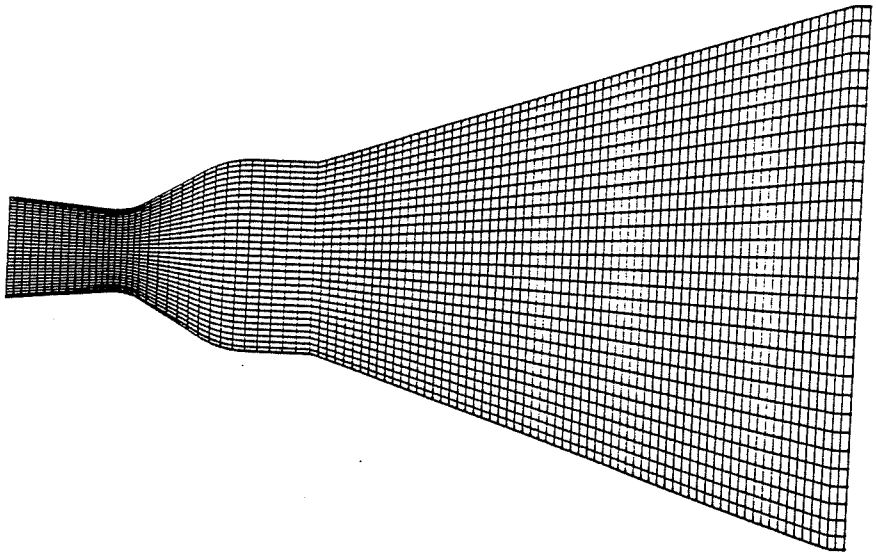

Fig. 6.1. (9) The spanwise center plane of the duct 2 with the nozzle

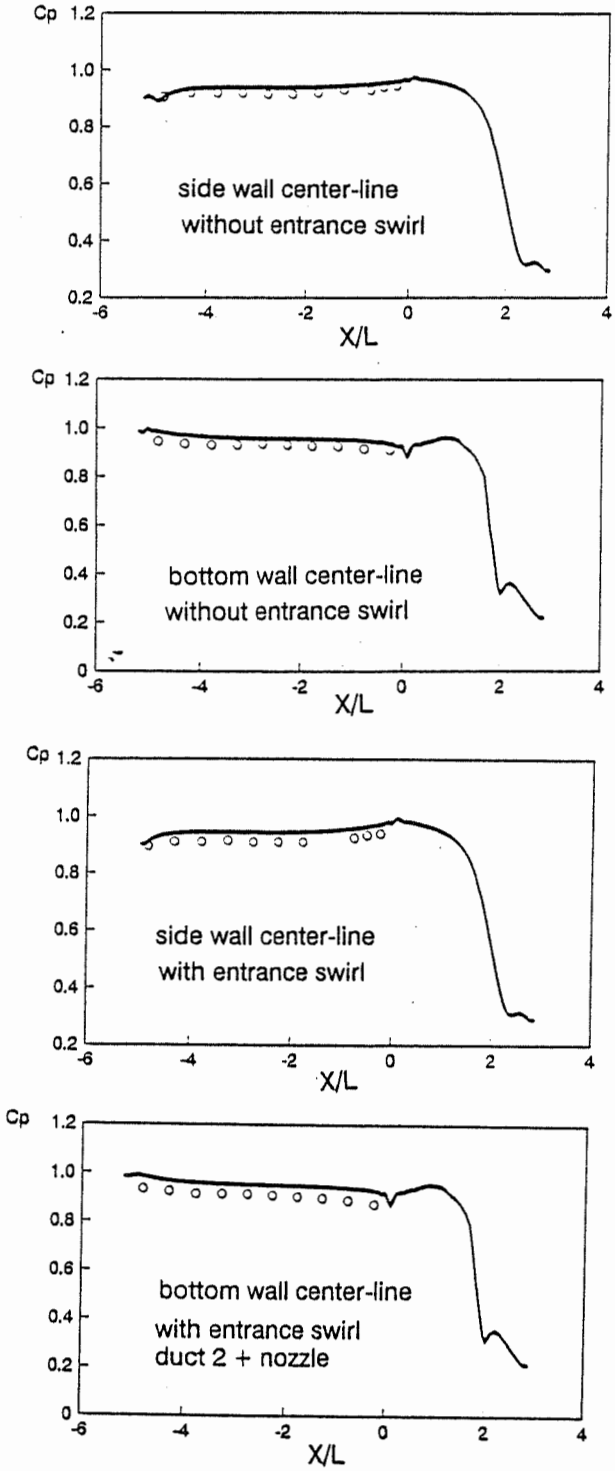

Fig. 6.1. (10) Pressure distributions of the duct 2 and the nozzle

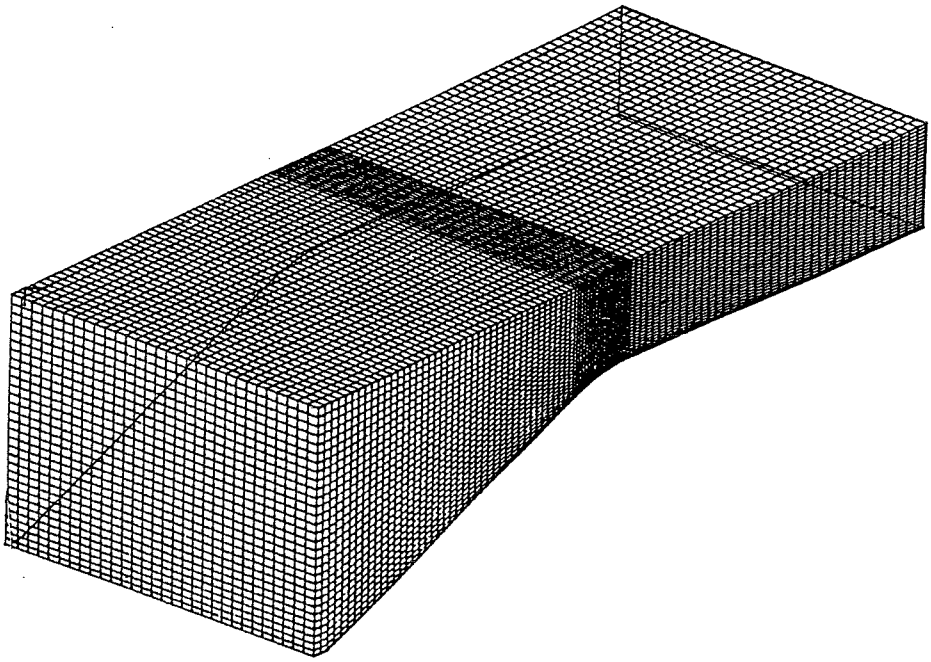

Fig. 6.1. (11) The grid and the geometry of the transonic nozzle

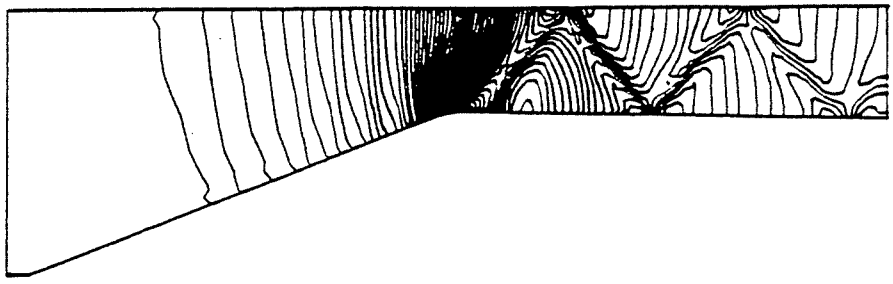

Fig. 6.1. (12) Pressure Contours of a Typical Section of the Nozzle

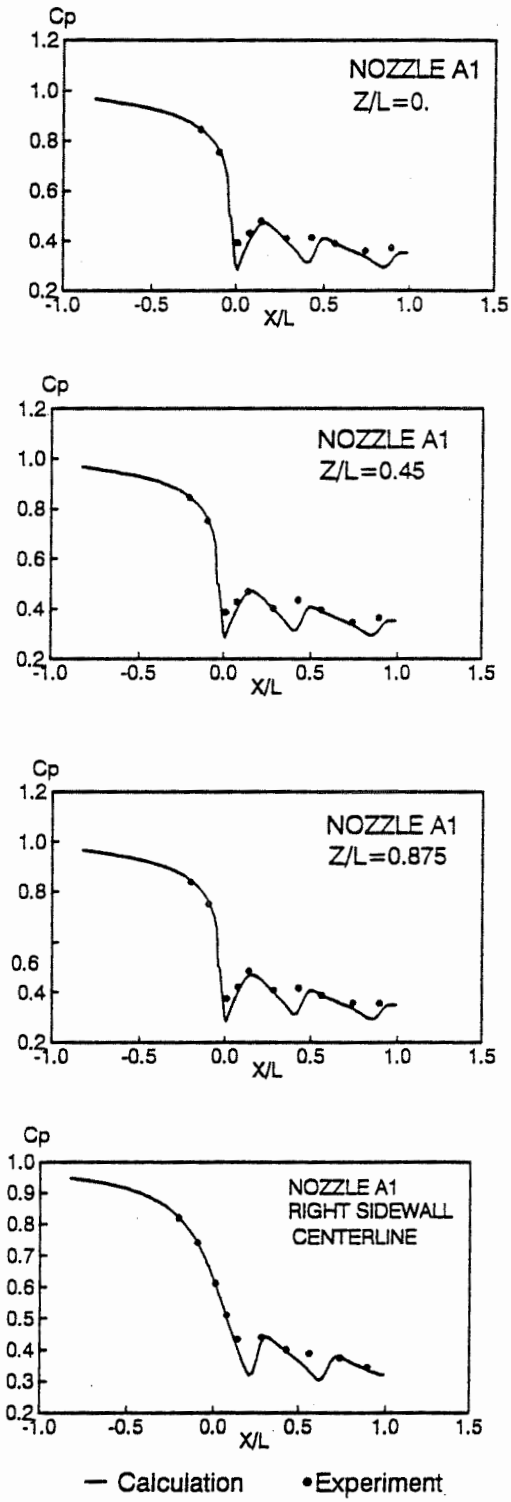

Fig. 6.1. (13) Pressure distributions of the nozzle

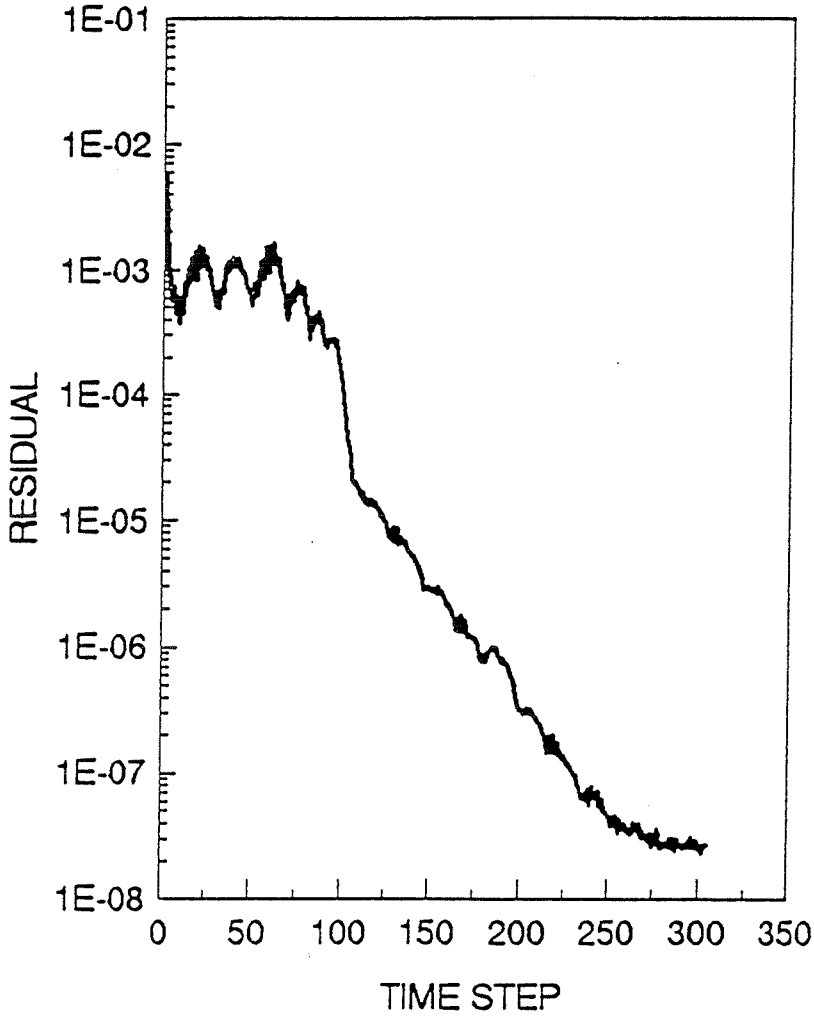

Fig. 6.1 (14) The convergency History of the Transonic Nozzle

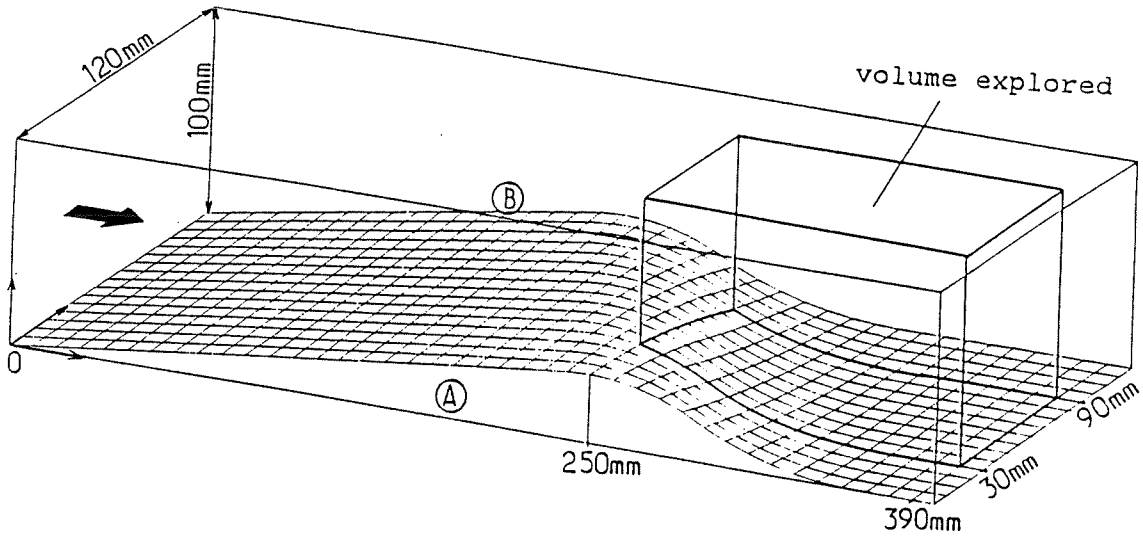

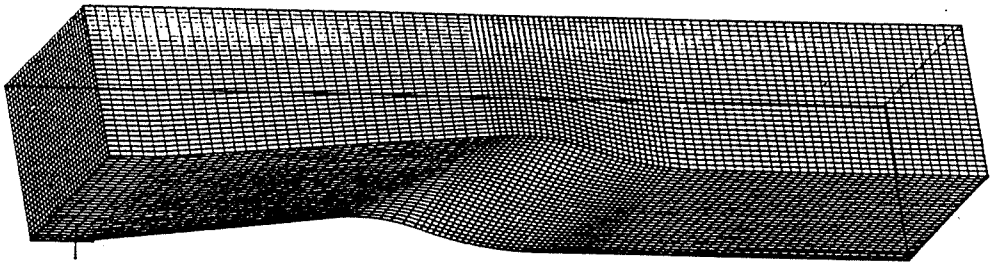

Fig. 6.1. (15) The grid and the geometry of the 3D channel, grid; 101x31x31

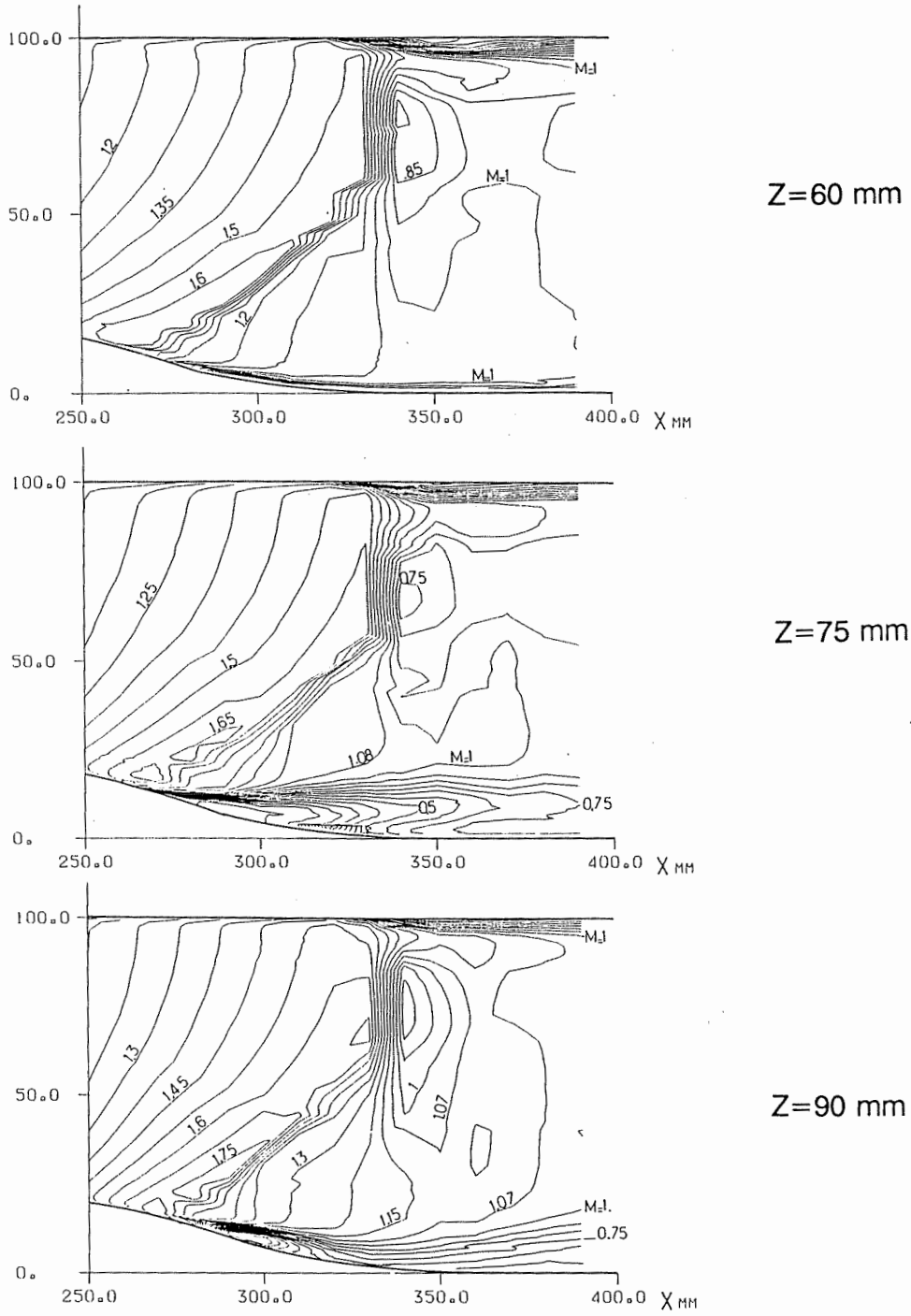

Fig. 6.1. (16) The experimental Mach number contours of the channel at different spanwise locations

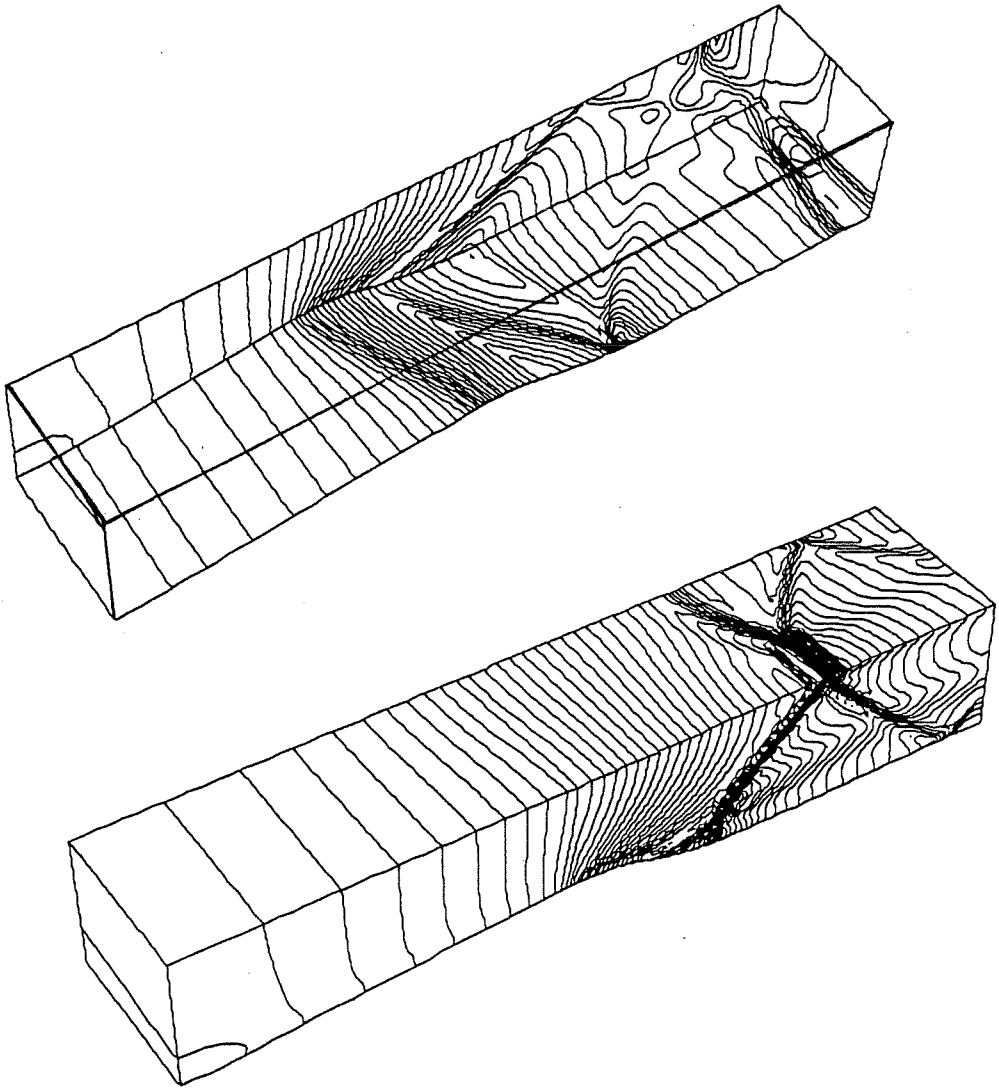

Fig. 6.1. (17) The calculated Mach number contours of the channel on the walls, Pe/Pt=0.545

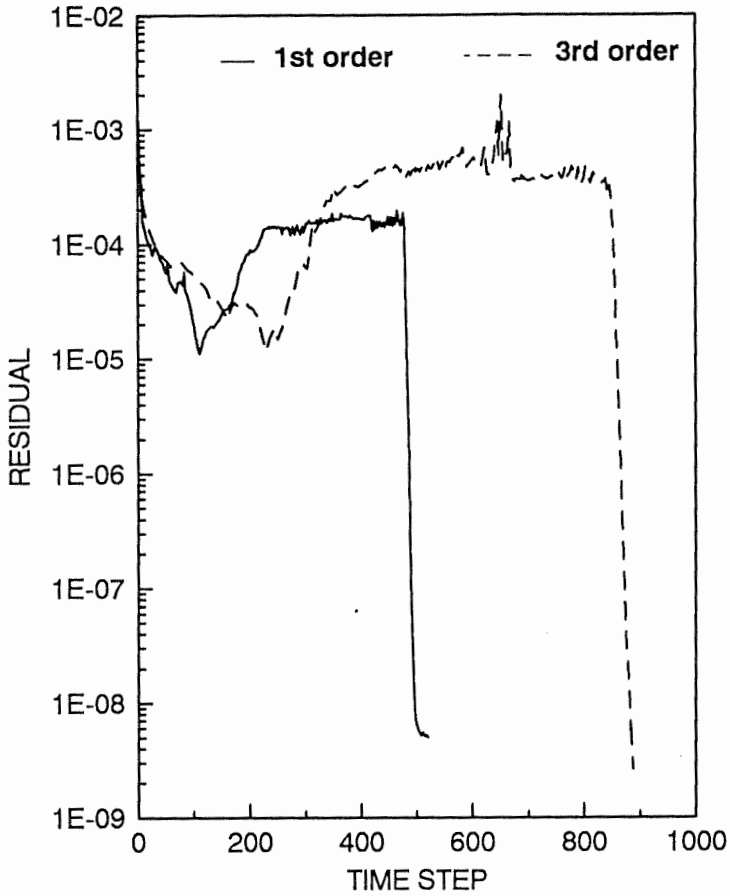

Fig. 6.1. (18) Convergency histories of the channel

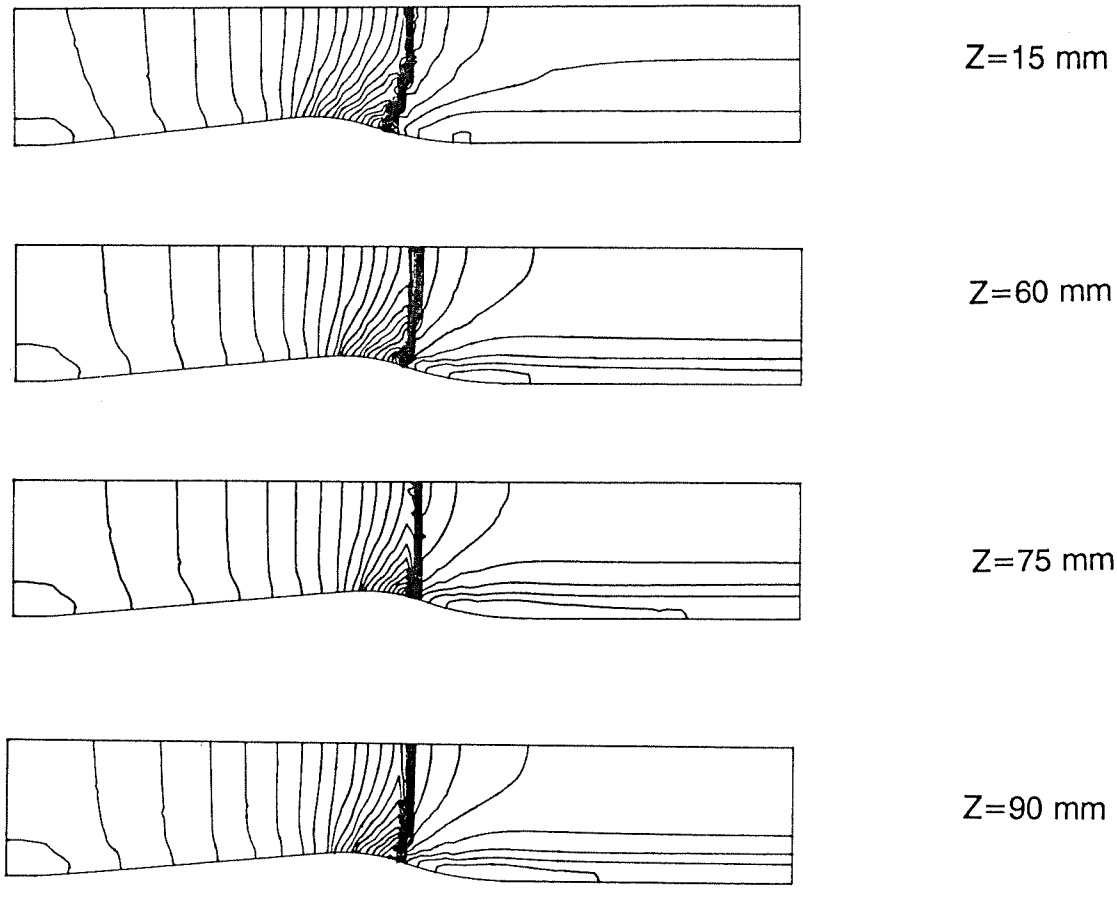

Fig. 6.1. (19) The calculated Mach number contours of the channel at different spanwise locations, Pe/Pt=0.755

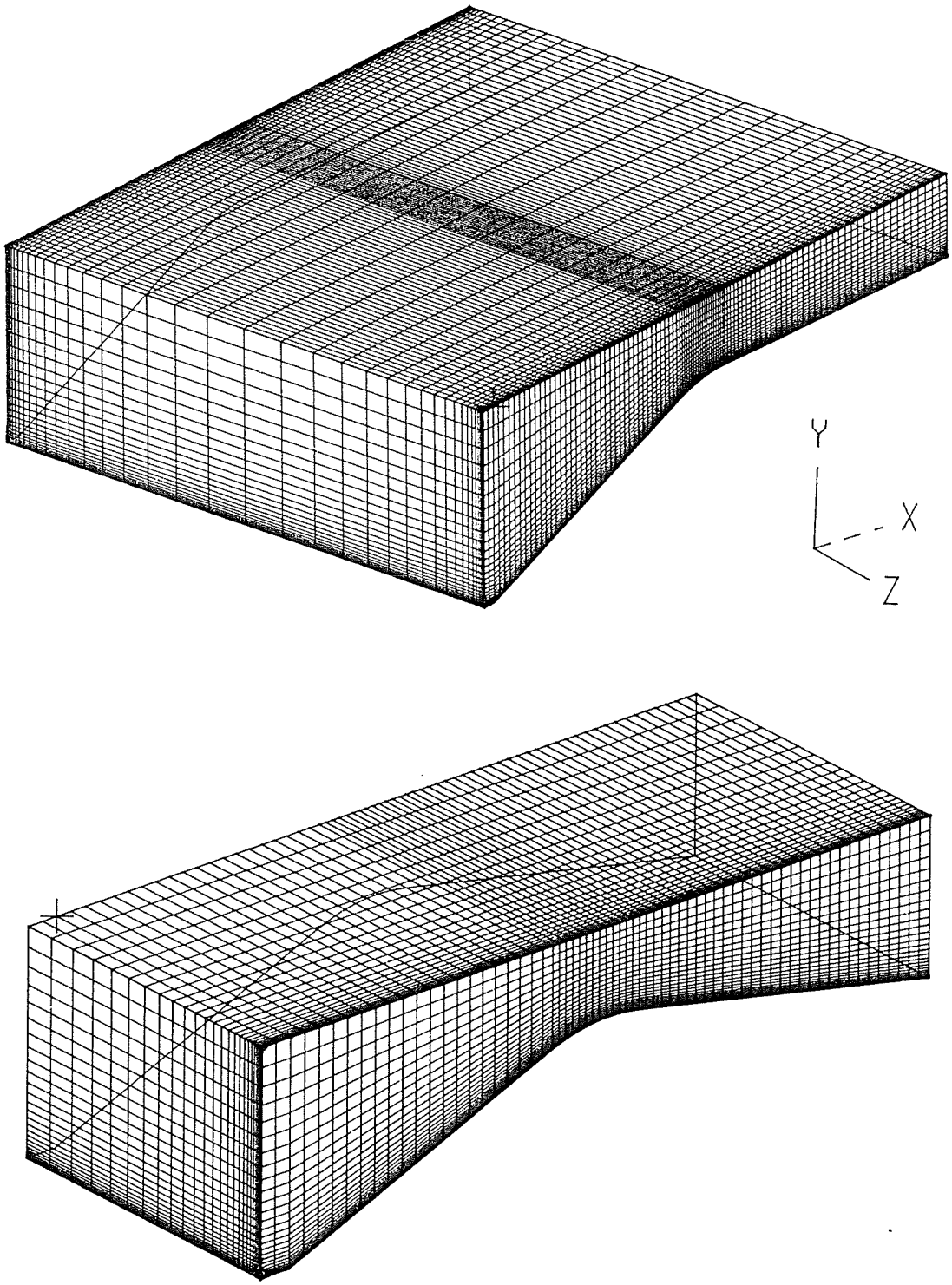

Fig. 6.1.(20) The three dimensional grid of the nozzles

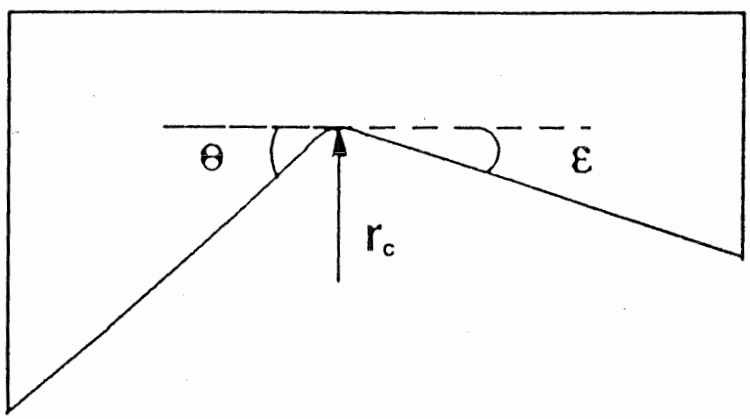

Fig. 6.1. (21) The sketch of a nozzle geometry

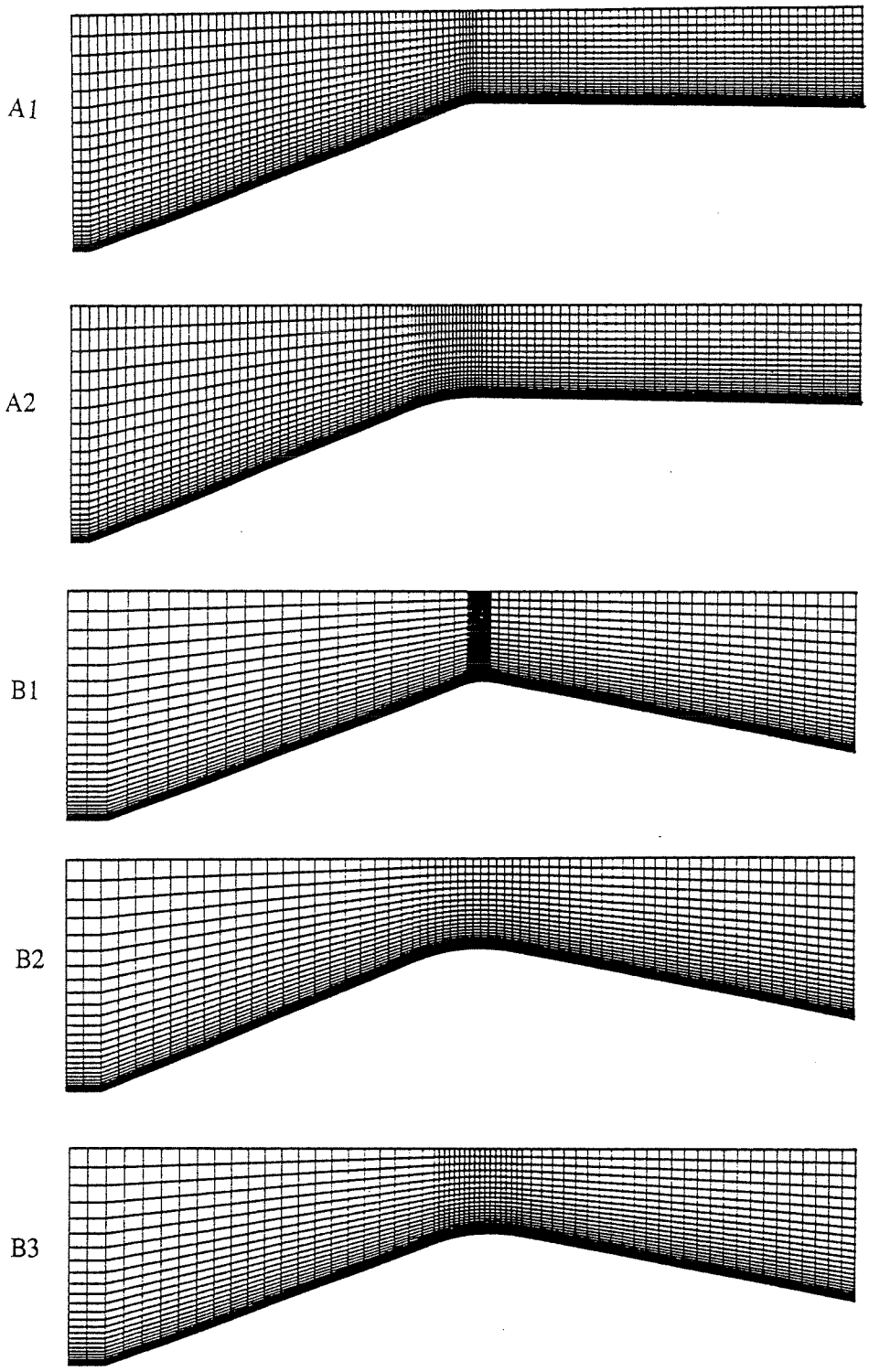

Fig. 6.1. (22) The streamwise sections of the five nozzles

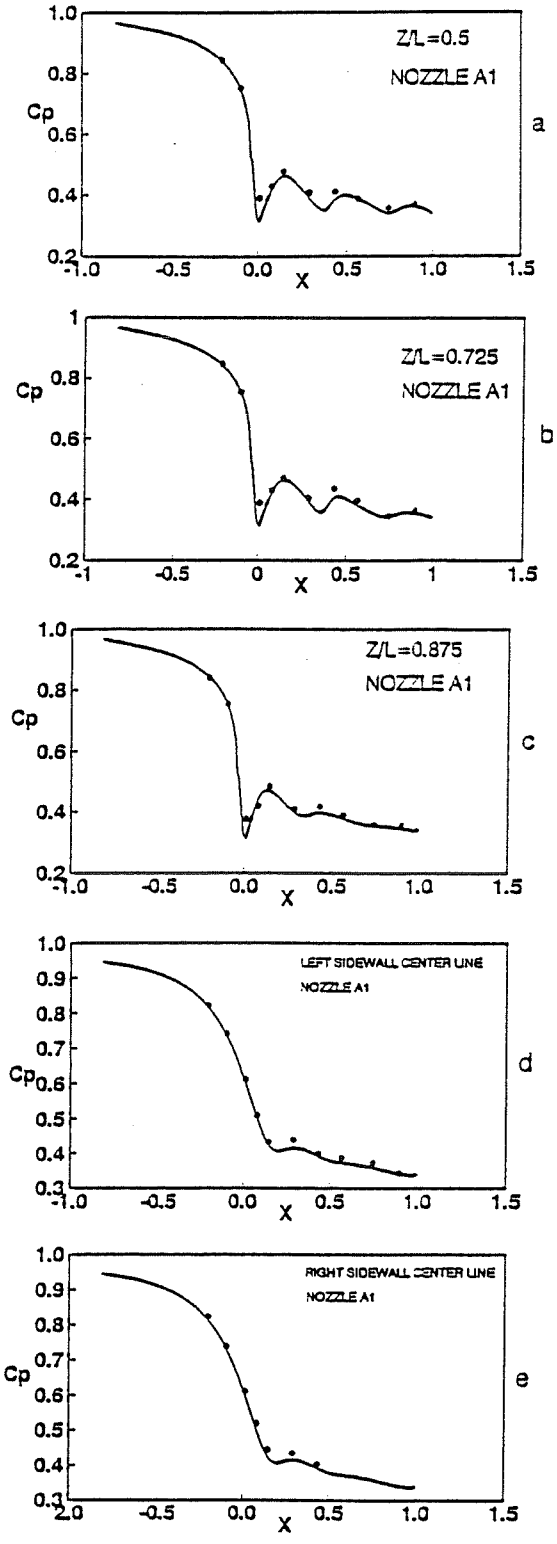

Fig. 6.1 (23) Pressure distributions of nozzle A1, • Experiment, -- Calculation

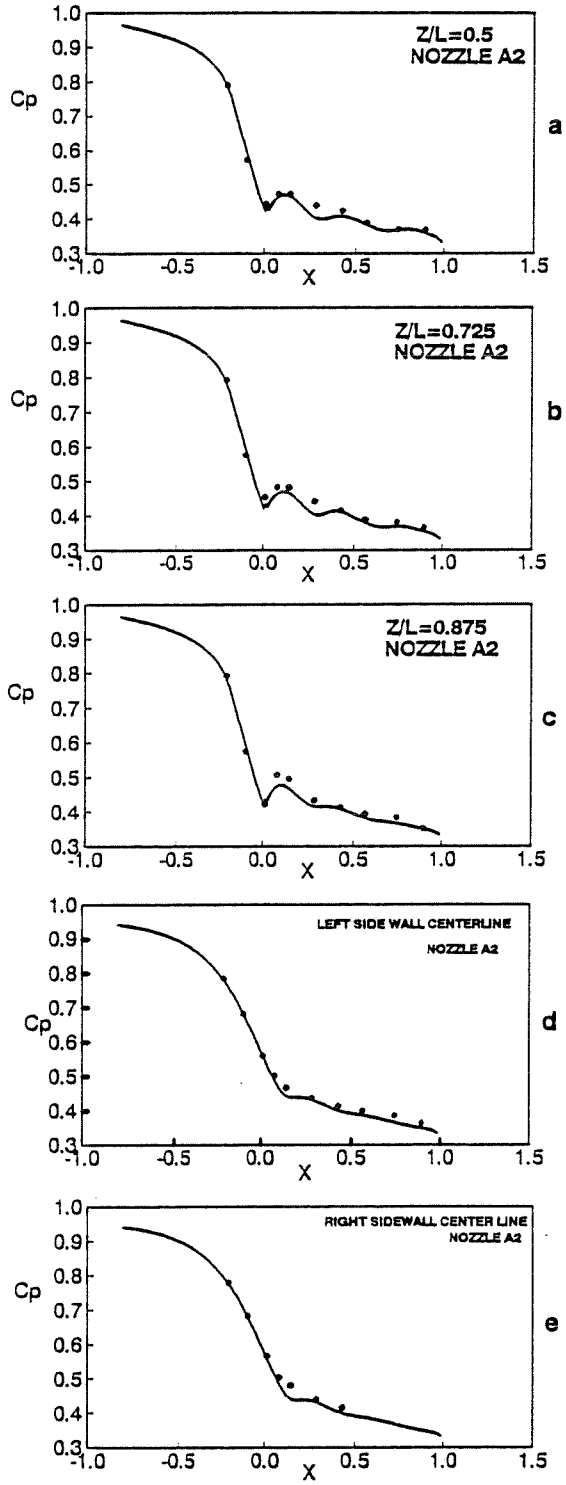

Fig. 6.1. (24) Pressure distributions of nozzle A2, • Experiment, – Calculation

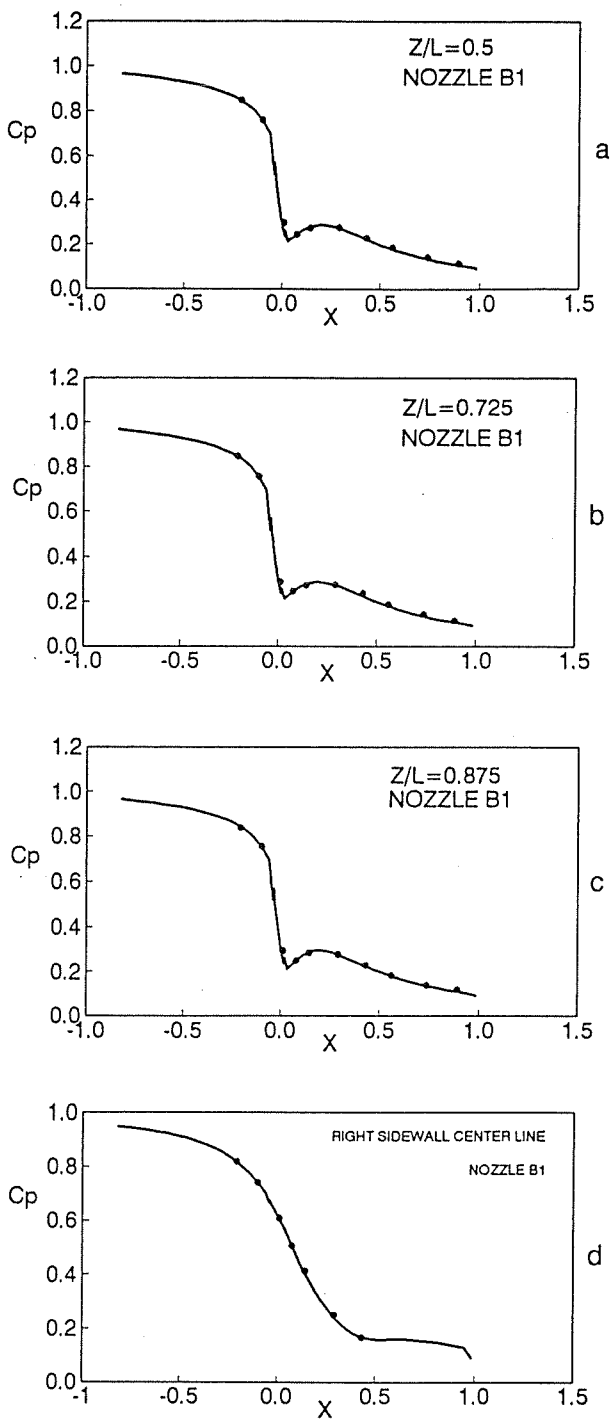

Fig. 6.1. (25) Pressure distributions of nozzle B1, • Experiment, – Calculation

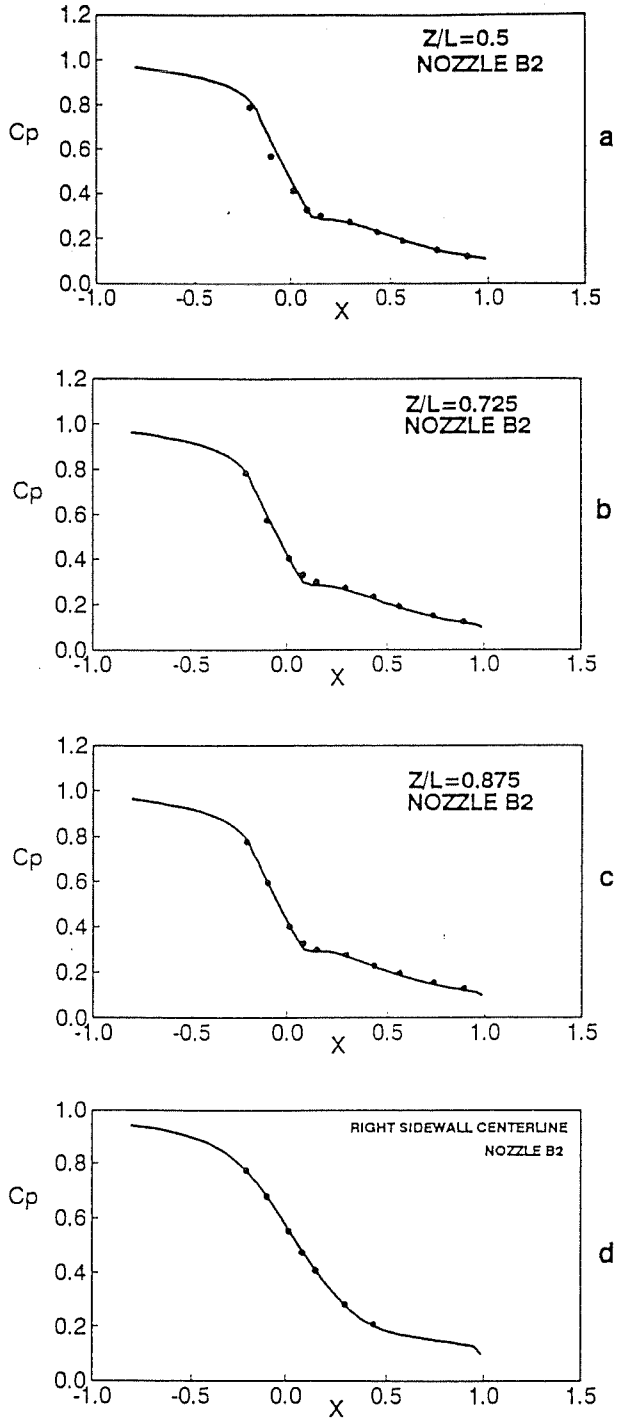

Fig. 6.1. (26) Pressure distributions of nozzle B2, • Experiment, – Calculation

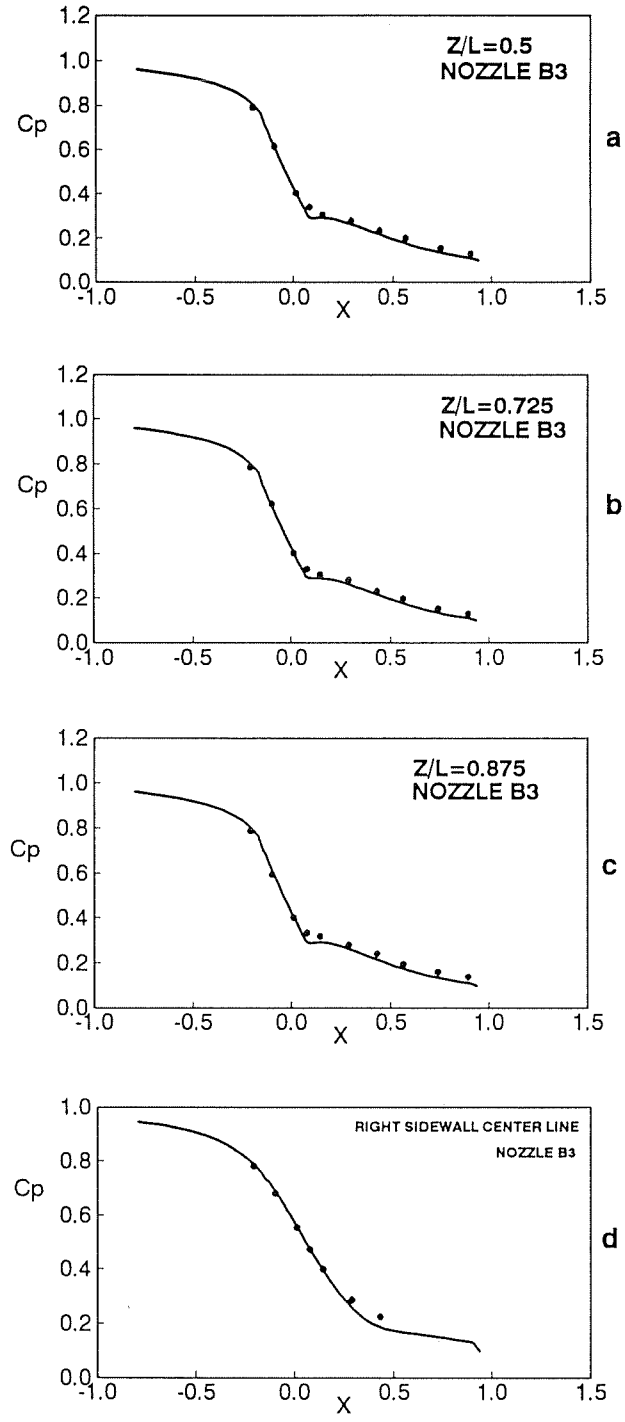

Fig. 6.1. (27) Pressure distributions of nozzle B3, • Experiment, – Calculation

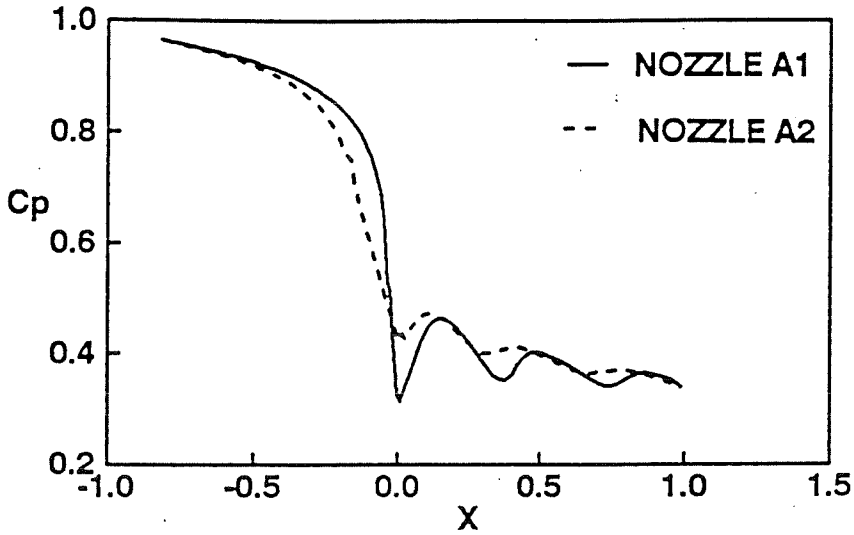

Fig. 6.1. (28) Calculated lower wall central-line pressure distributions

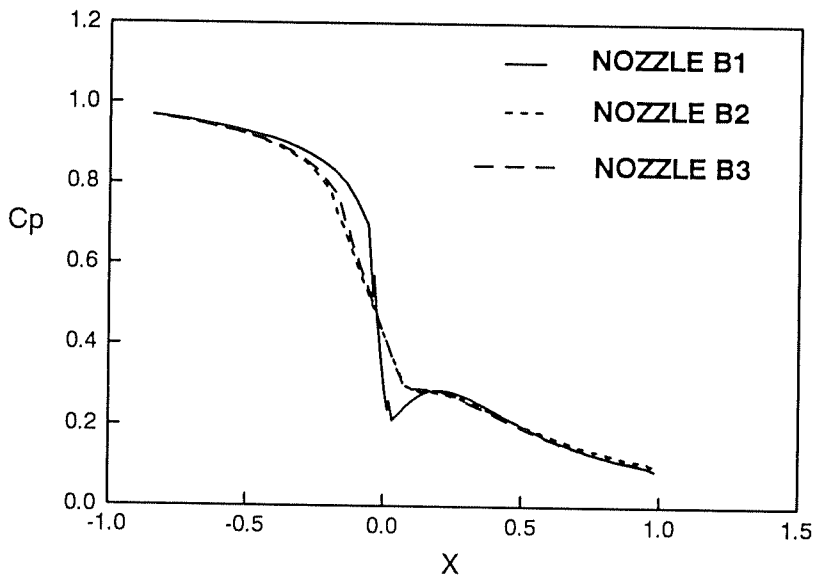

Fig. 6.1. (29) Calculated lower wall central-line pressure distributions

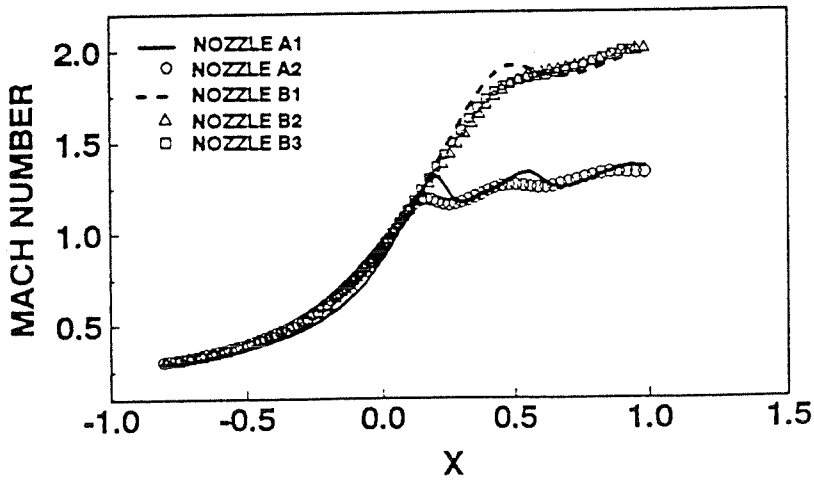

Fig. 6.1. (30) Mach number distributions along the nozzle central lines

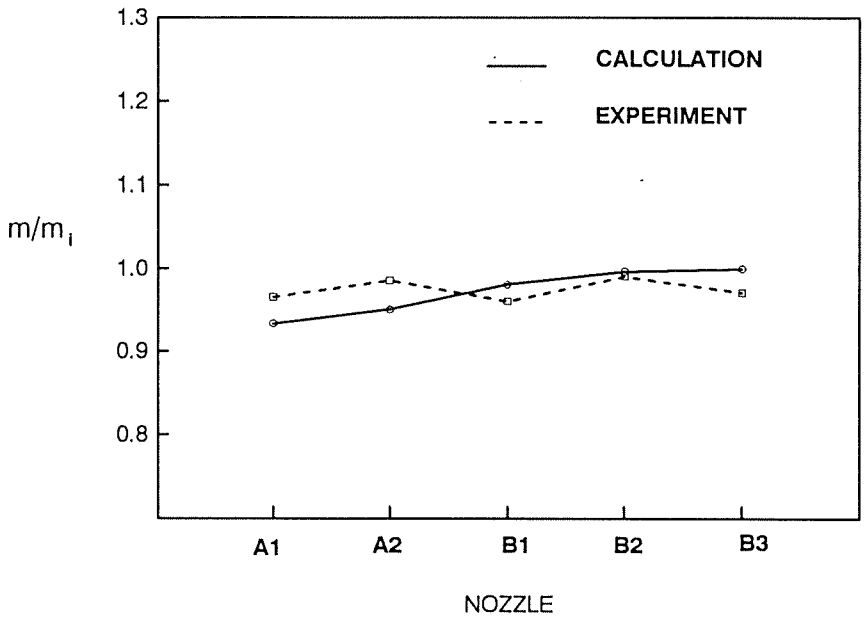

Fig. 6.1. (31) The discharge coefficients of the nozzles

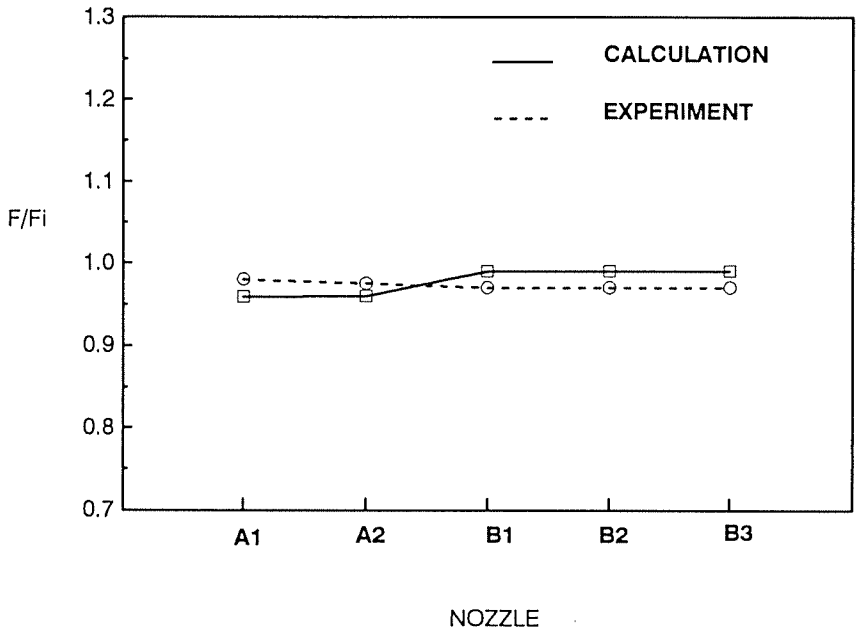

Fig. 6.1. (32) The thrust ratios of the nozzles

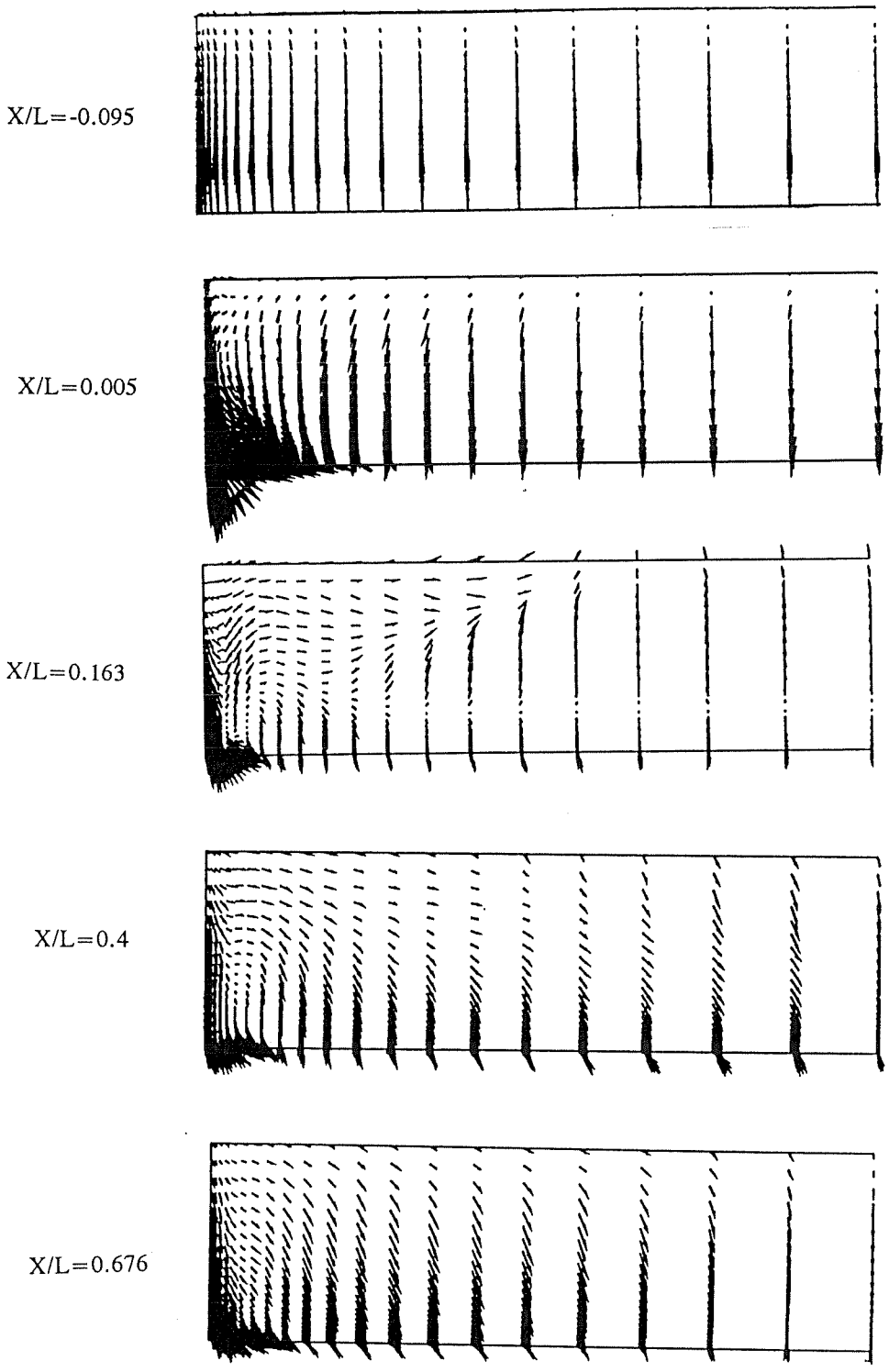

Fig. 6.1. (33) Spanwise section velocity fields of Nozzle A1

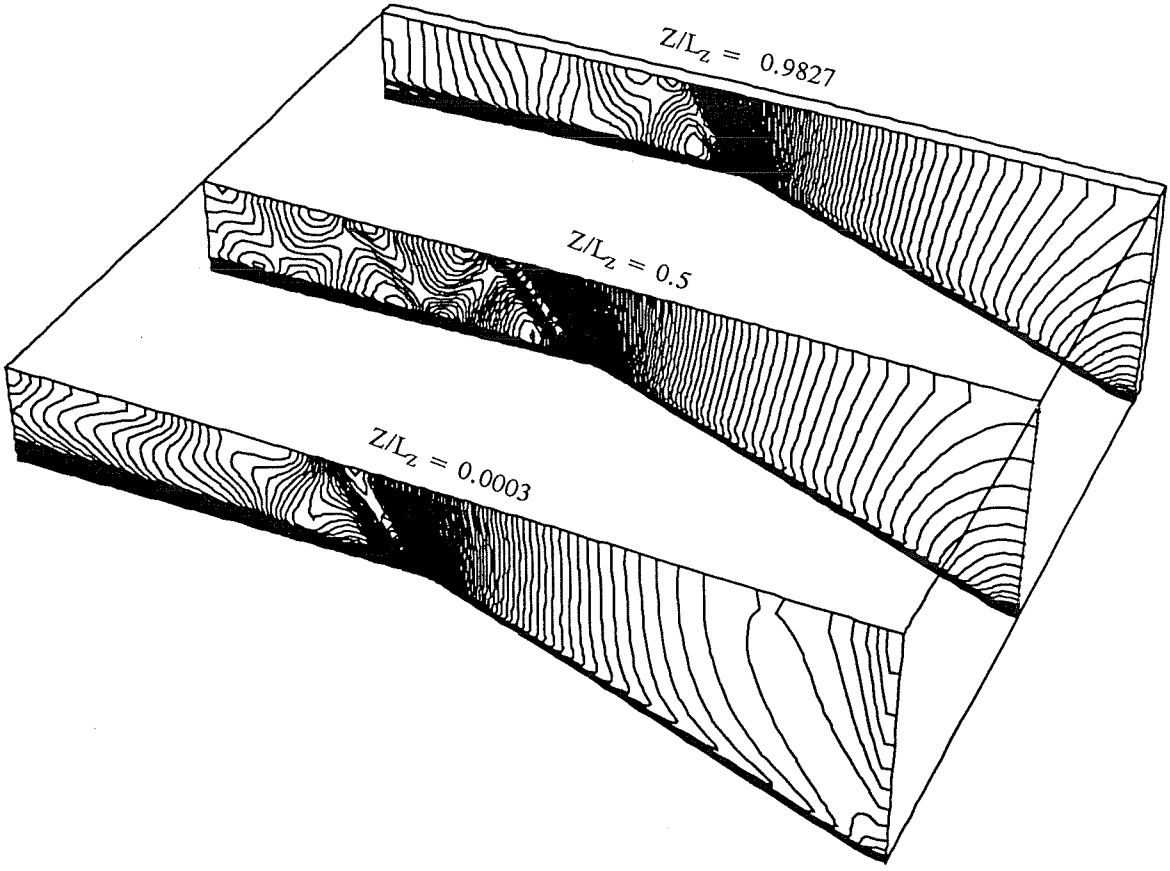

Fig. 6.1. (34) Mach number contours at different sections of Nozzle A1

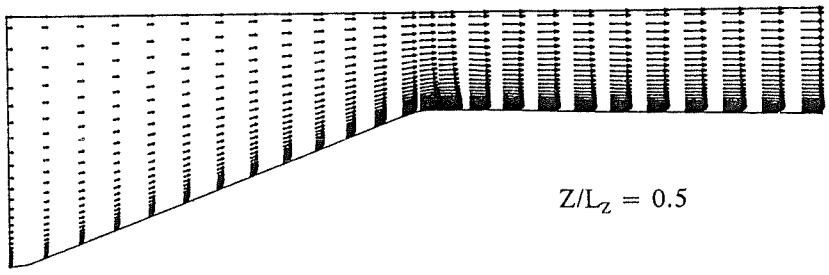

Fig. 6.1. (35) Streamwise section velocity field of Nozzle A1

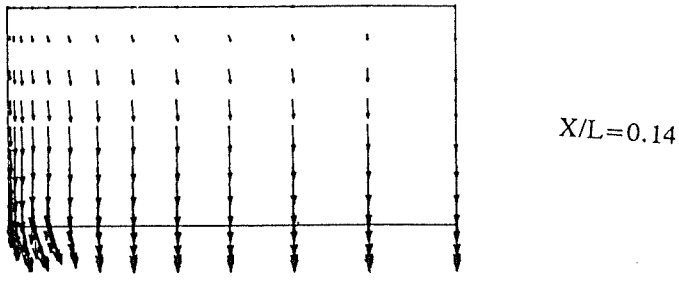

Fig. 6.1. (36) Spanwise section velocity field near the exit of Nozzle B2

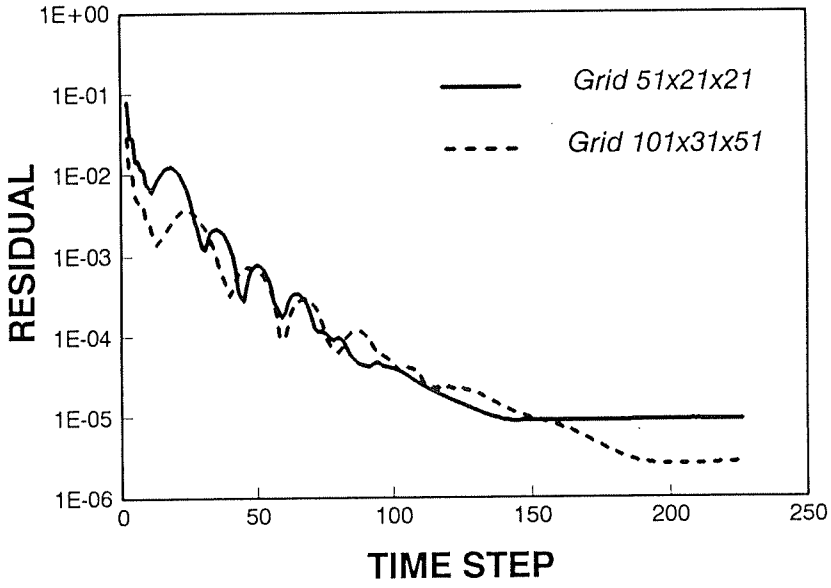

Fig. 6.1. (37) Convergence Histories of Nozzle A2

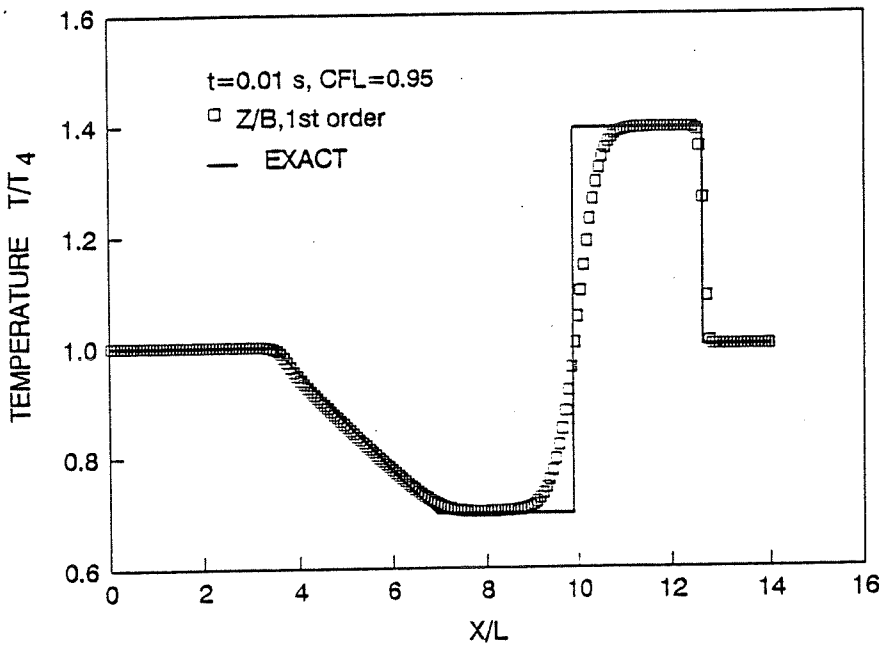

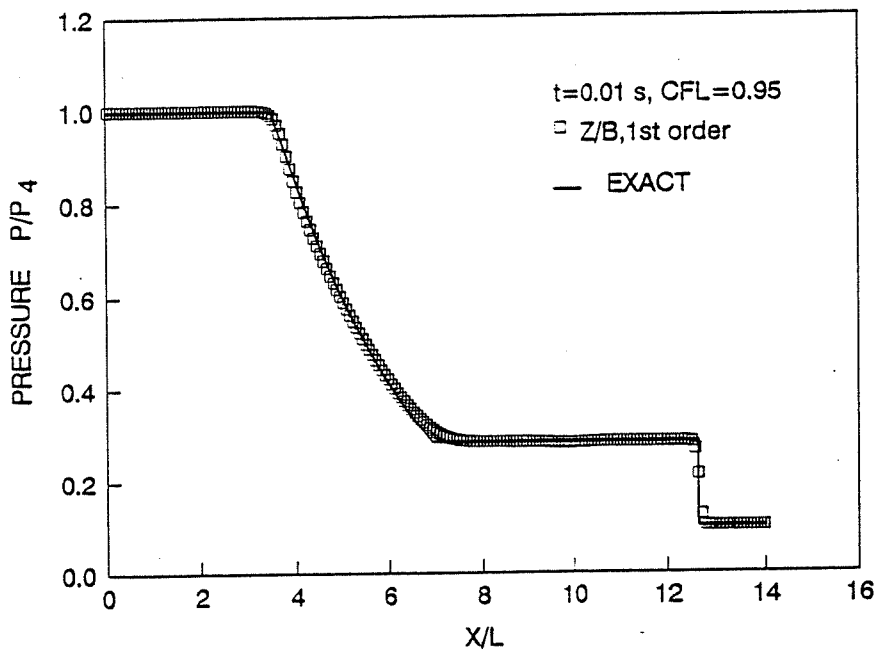

Fig. 6.2. (1) 1D Shock tube results calculated by using the present scheme, grid size: 201, Temperature and Pressure

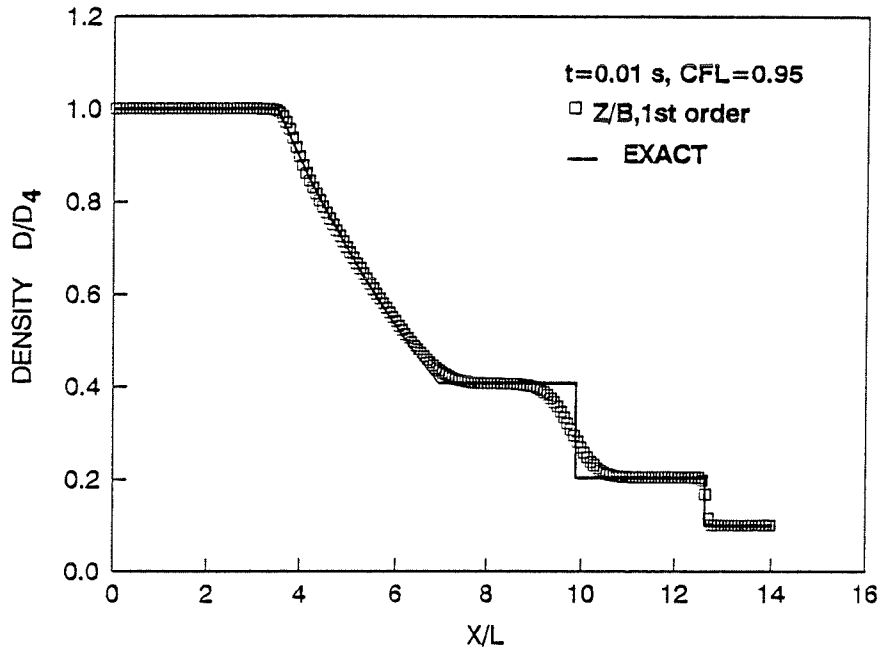

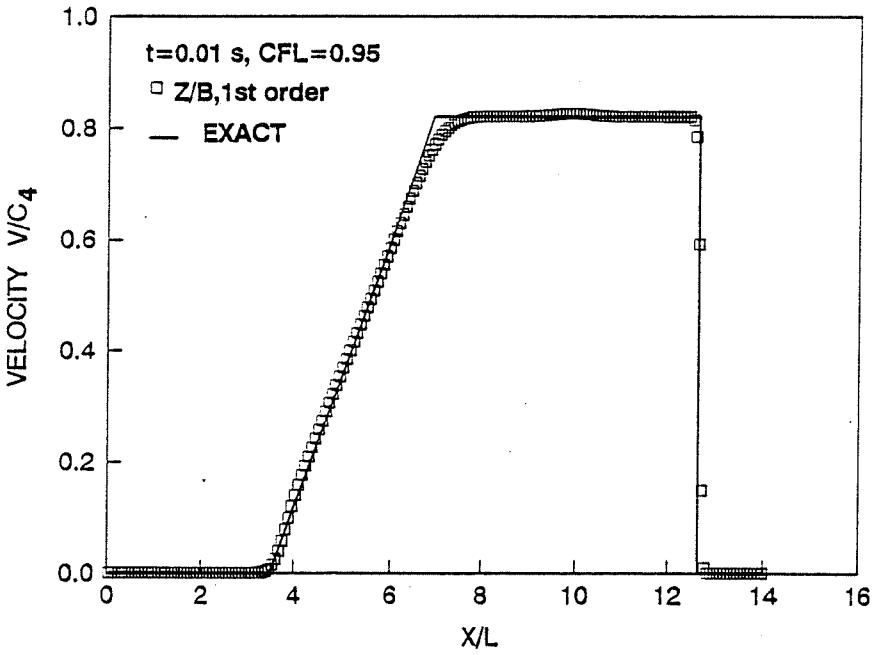

Fig. 6.2. (2) 1D Shock tube results calculated by using the present scheme, grid size: 201, Density and Velocity

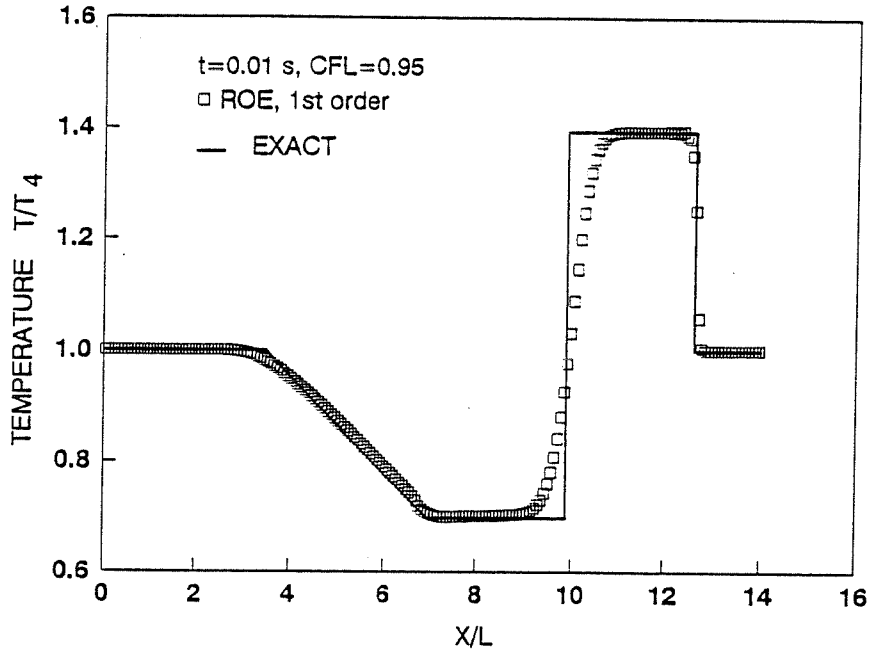

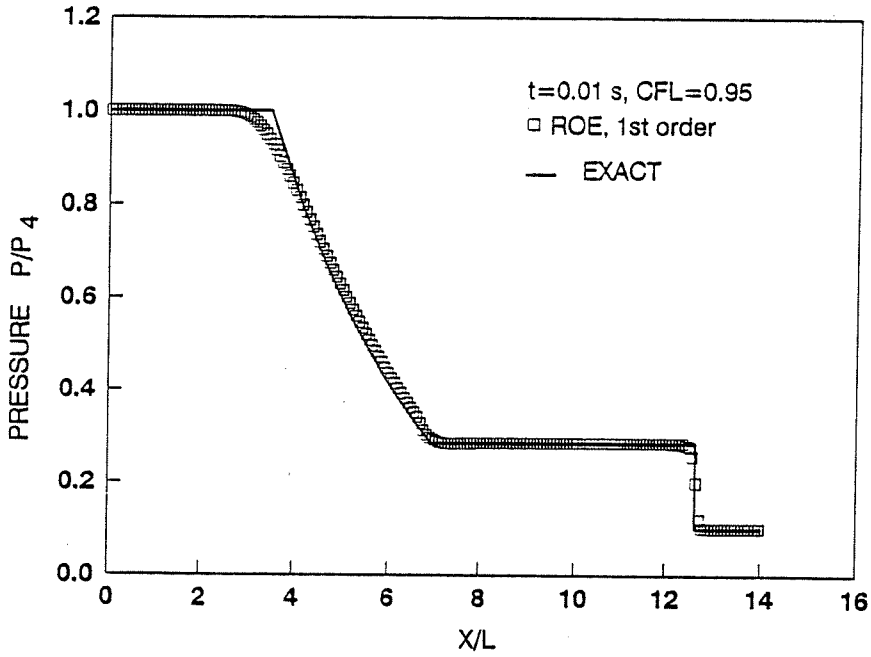

Fig. 6.2. (3) 1D Shock tube results calculated by using Roe scheme, grid size: 201, Temperature and Pressure

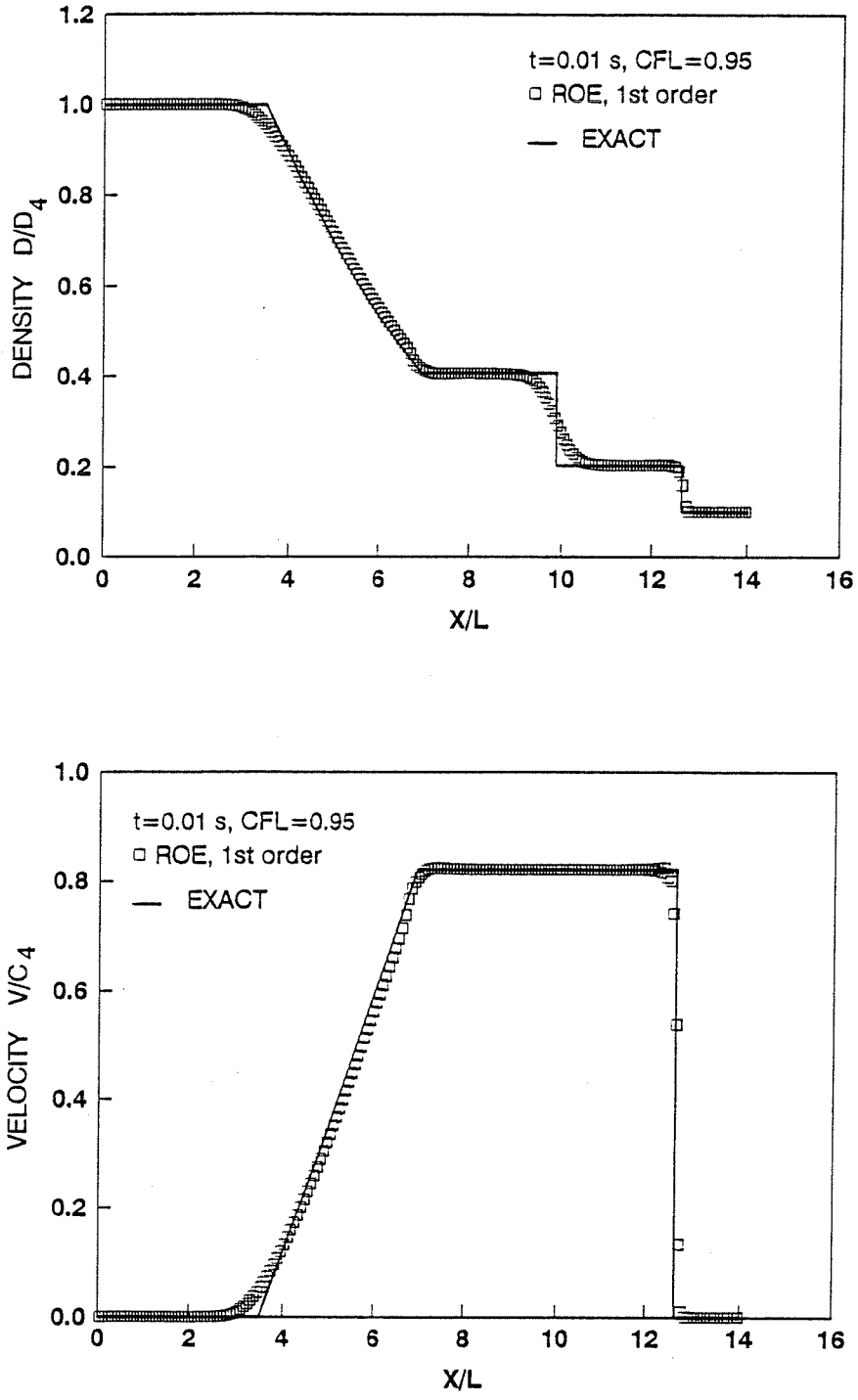

Fig. 6.2. (4) 1D Shock tube results calculated by using Roe scheme, grid size: 201, Density and Velocity

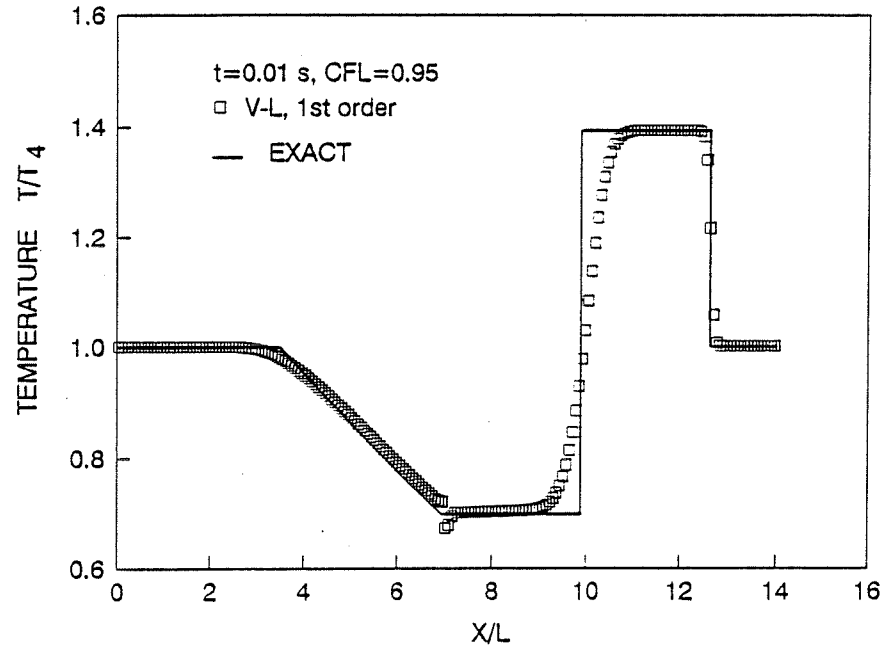

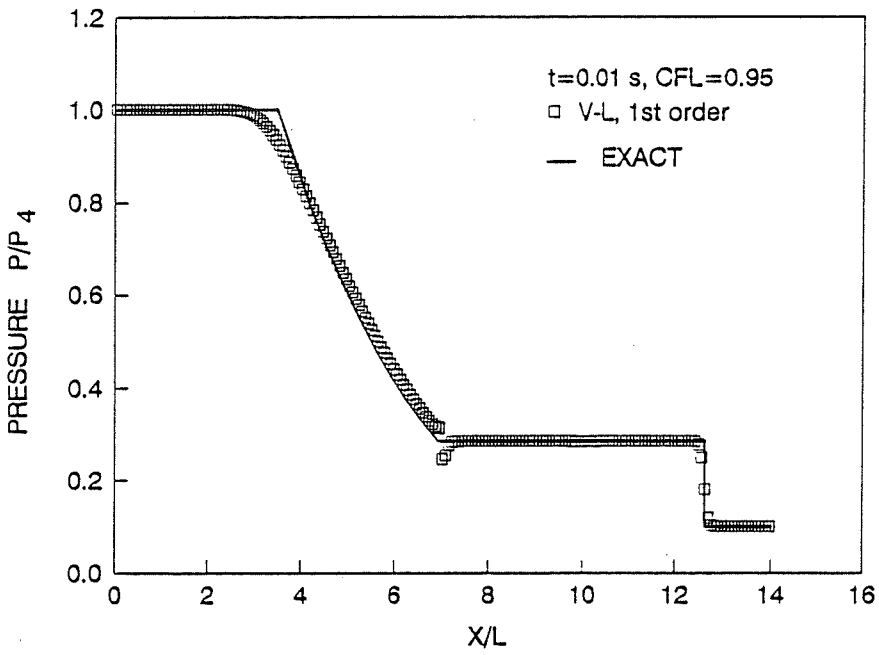

Fig. 6.2. (5) 1D Shock tube results calculated by using Van Leer scheme, grid size: 201, Temperature and Pressure

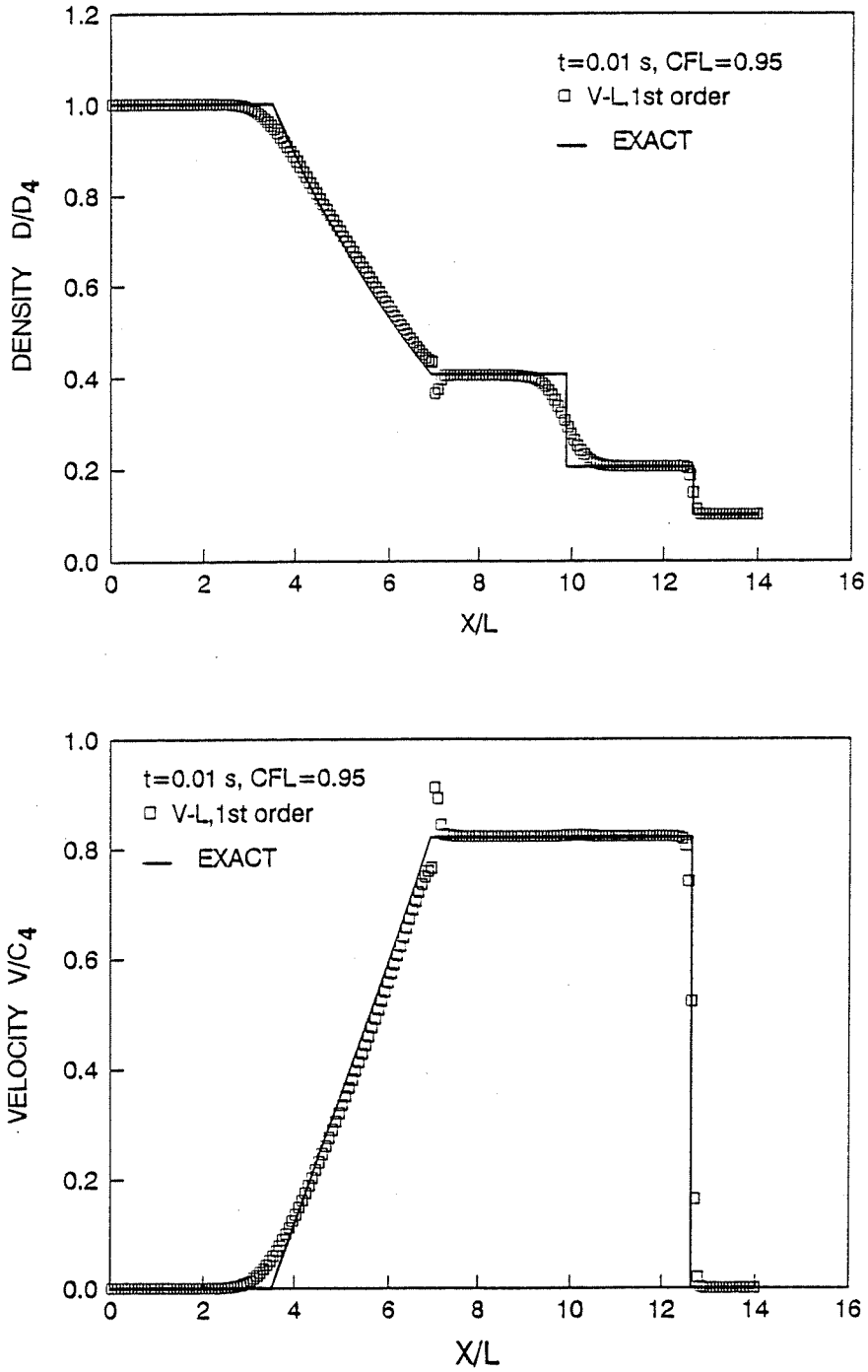

Fig. 6.2. (6) 1D Shock tube results calculated by using Van Leer scheme, grid size: 201, Density and Velocity

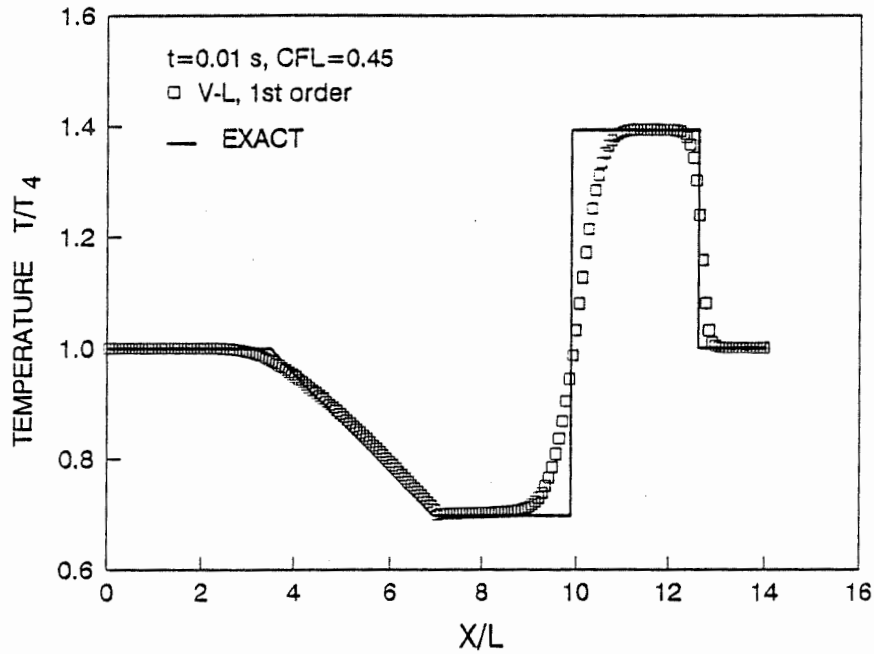

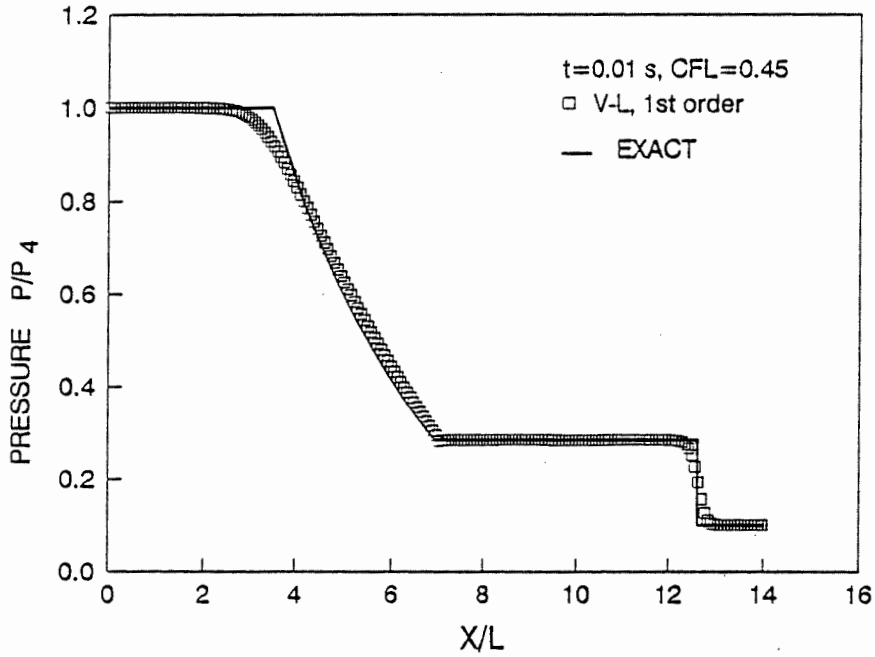

Fig. 6.2. (7) 1D Shock tube results calculated by using Van Leer scheme, grid size: 201, Temperature and Pressure

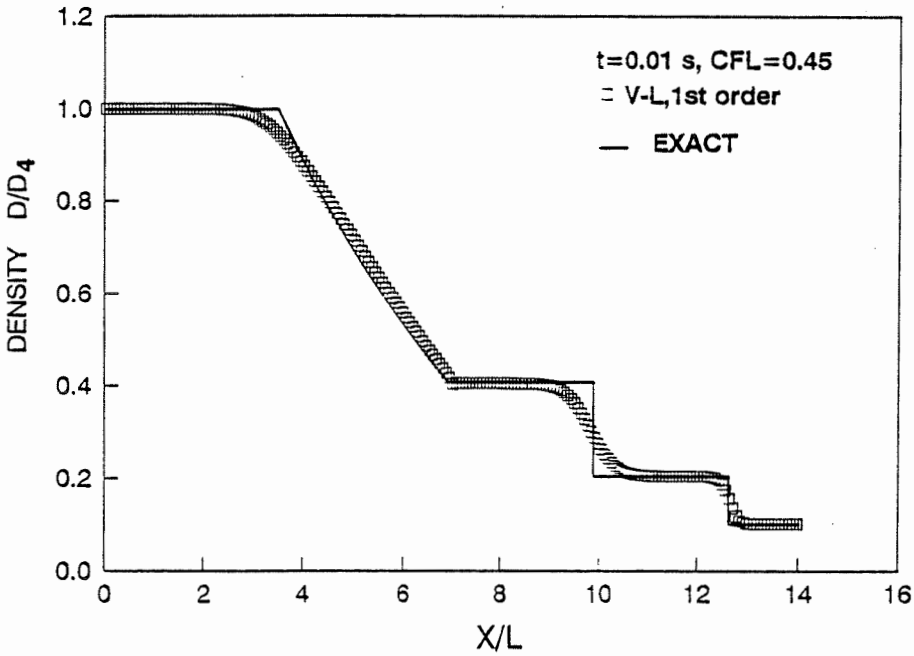

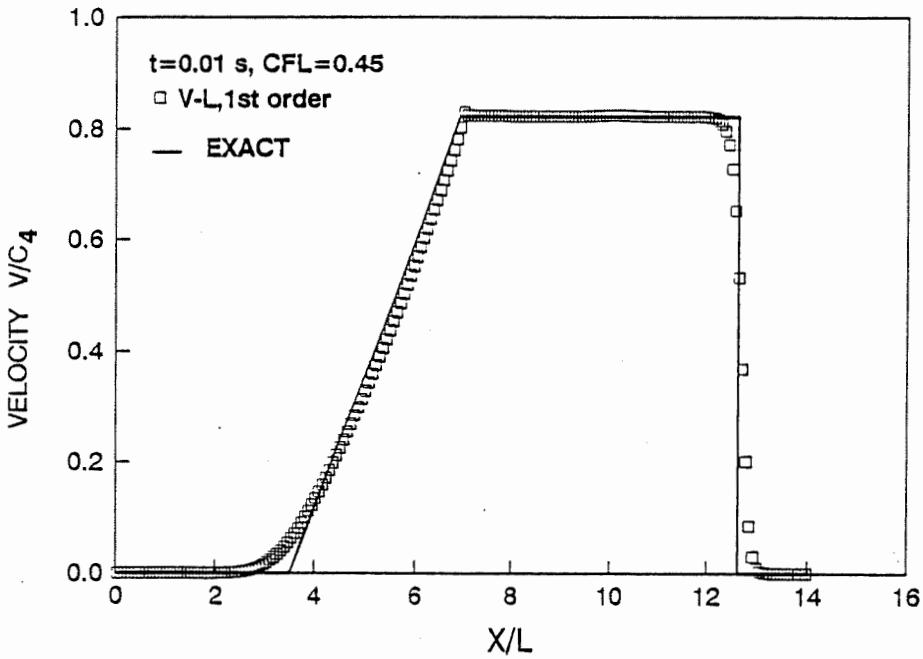

Fig. 6.2. (8) 1D Shock tube results calculated by using Van Leer scheme, grid size: 201, Density and Velocity

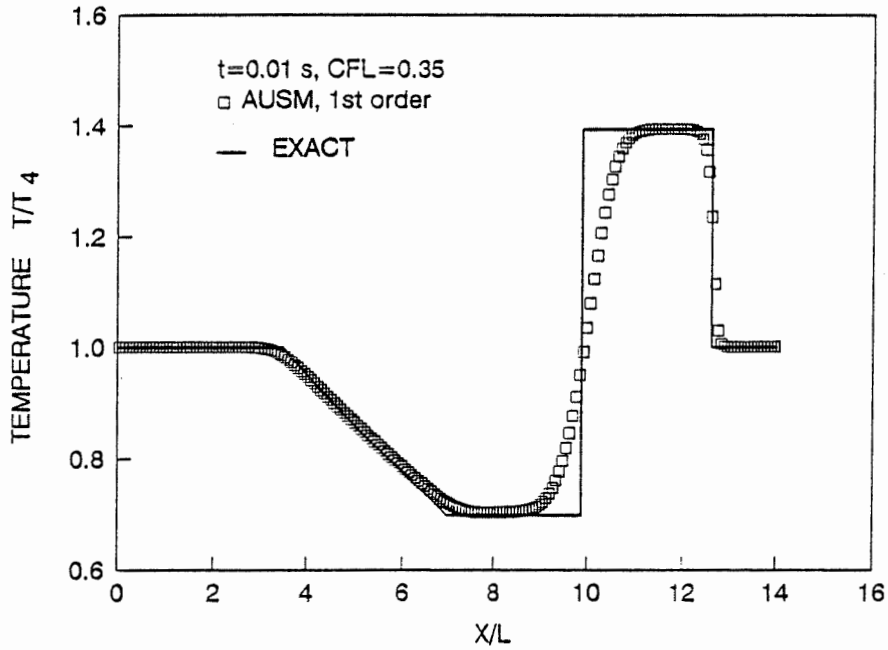

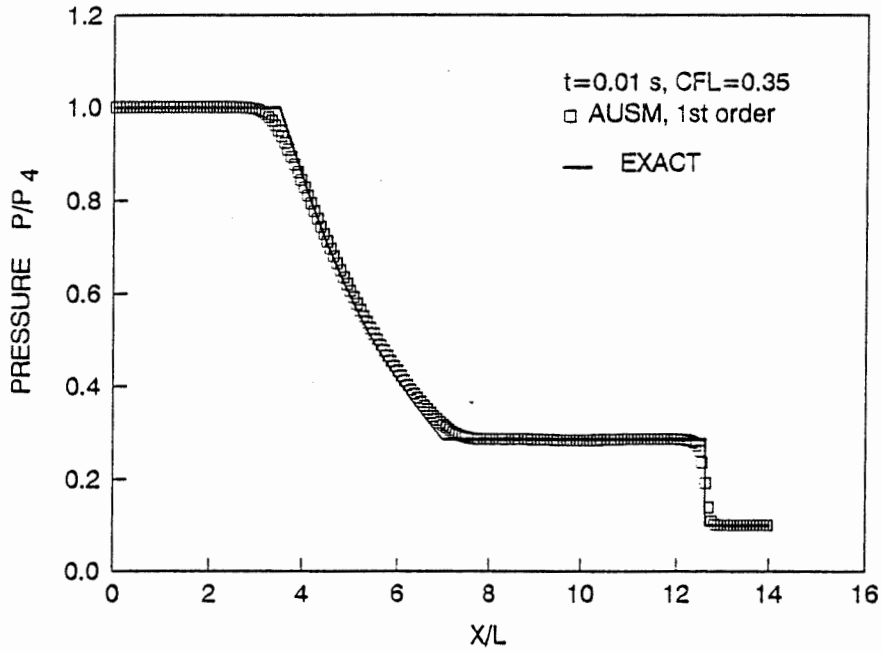

Fig. 6.2. (9) 1D Shock tube results calculated by using AUSM scheme, grid size: 201, Temperature and Pressure

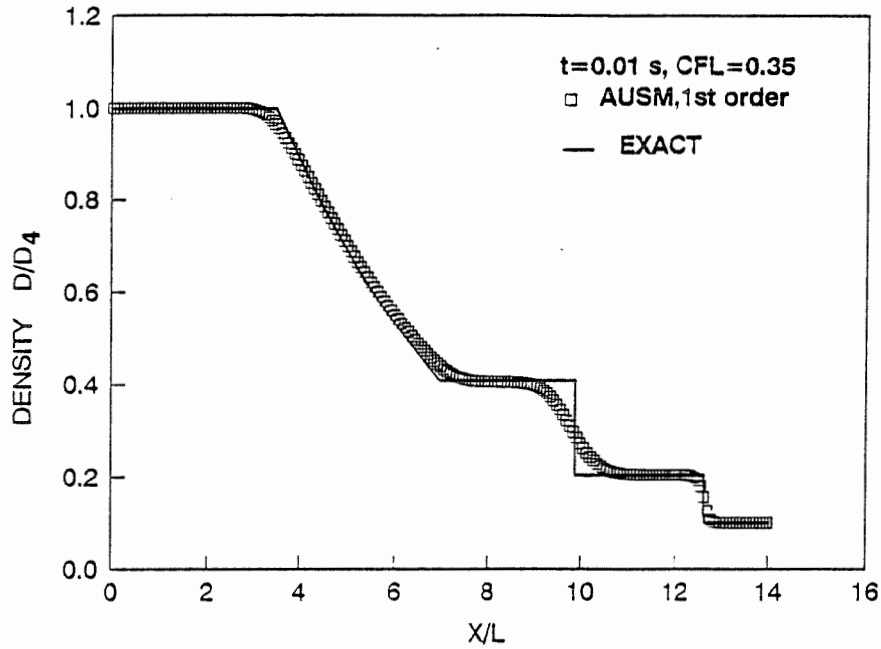

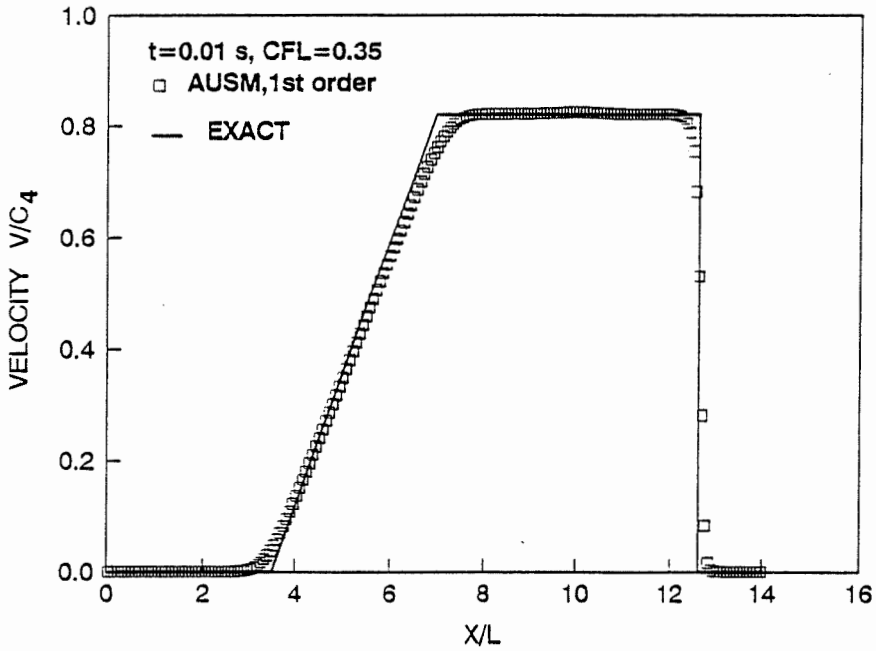

Fig. 6.2. (10) 1D Shock tube results calculated by using AUSM scheme, grid size: 201, Density and Velocity

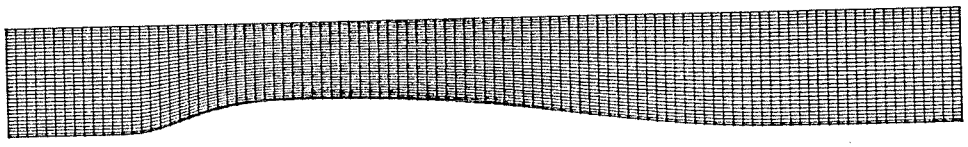

Fig. 6.2. (11) 2D Grid of the Inlet-Diffuser, 101 x 31

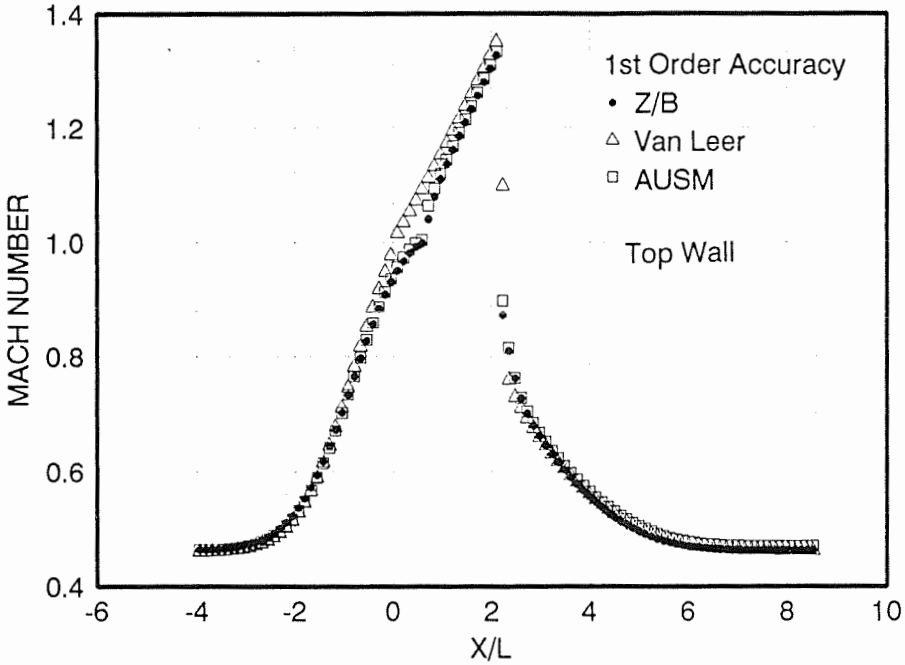

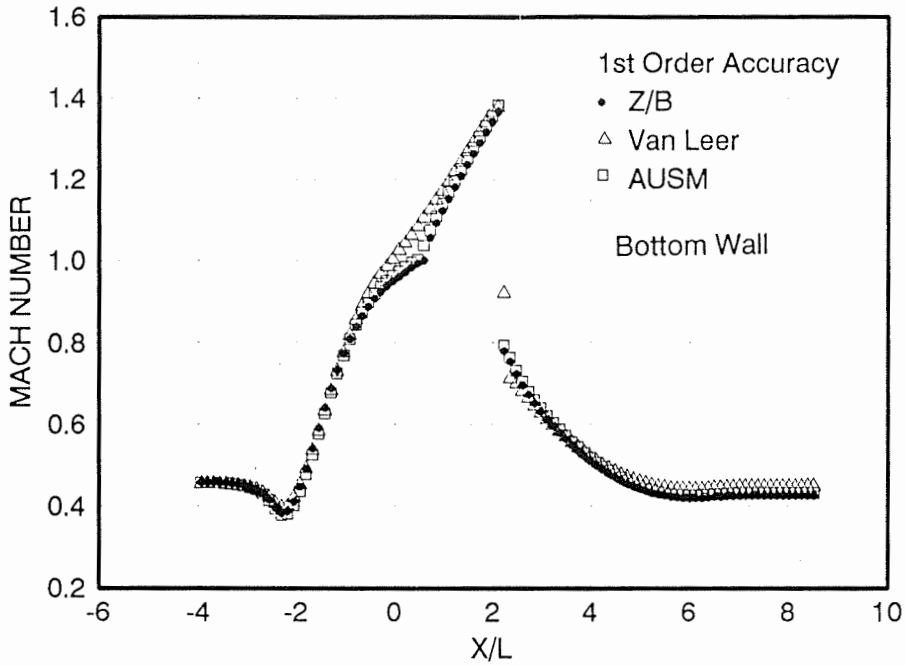

Fig. 6.2. (12) Mach number distributions along the walls of the inlet-diffuser with grid 101 x 31

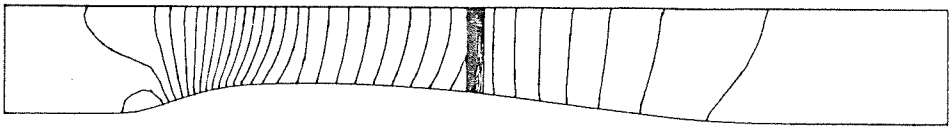

Van Leer Scheme

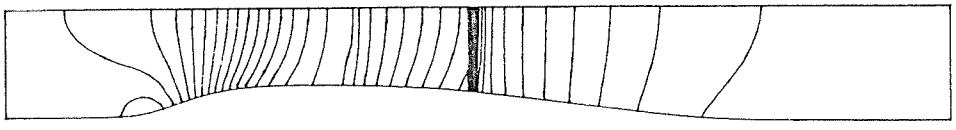

AUSM Scheme

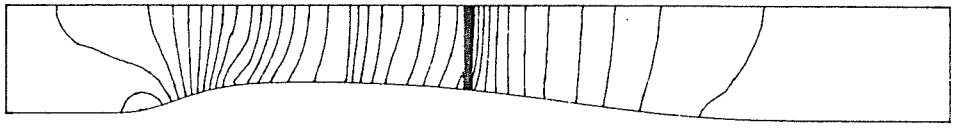

The Present Scheme

Fig. 6.2. (13) The pressure contours of the inlet-diffuser calculated by using the first order differencing with grid 101 x 31

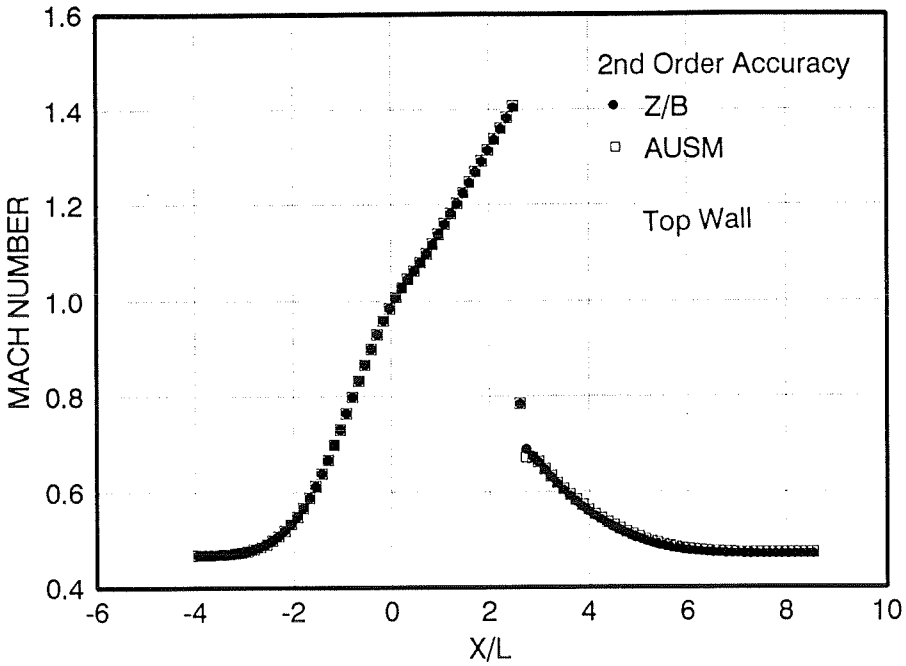

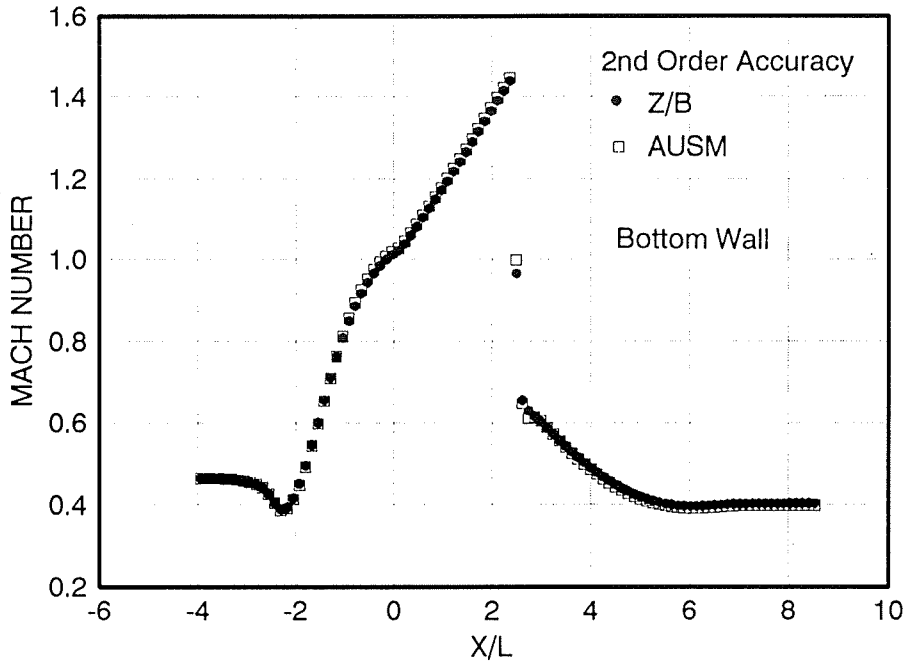

Fig. 6.2. (14) Mach number distributions along the walls of the inlet-diffuser with grid 101 x 31

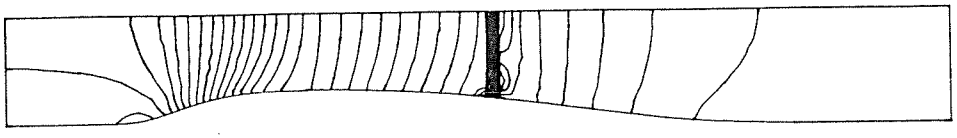

AUSM Scheme

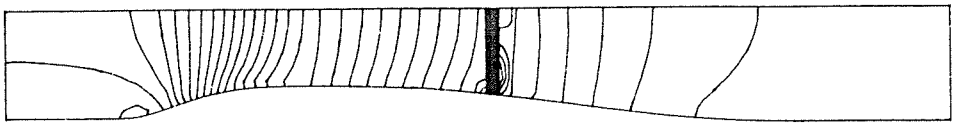

The Present Scheme

Fig. 6.2. (15) The pressure contours of the inlet-diffuser calculated by using the second order differencing with grid 101 x 31

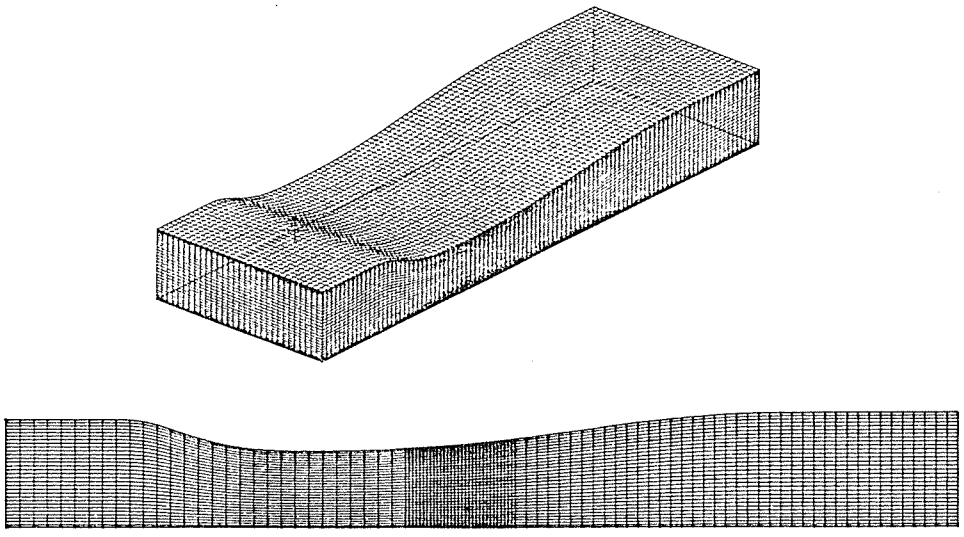

Fig. 6.2. (16) 3D Grid of the Inlet-Diffuser with grid 101 x 31 x 31. To see the geometry, the bottom of the diffuser is shown at the top.

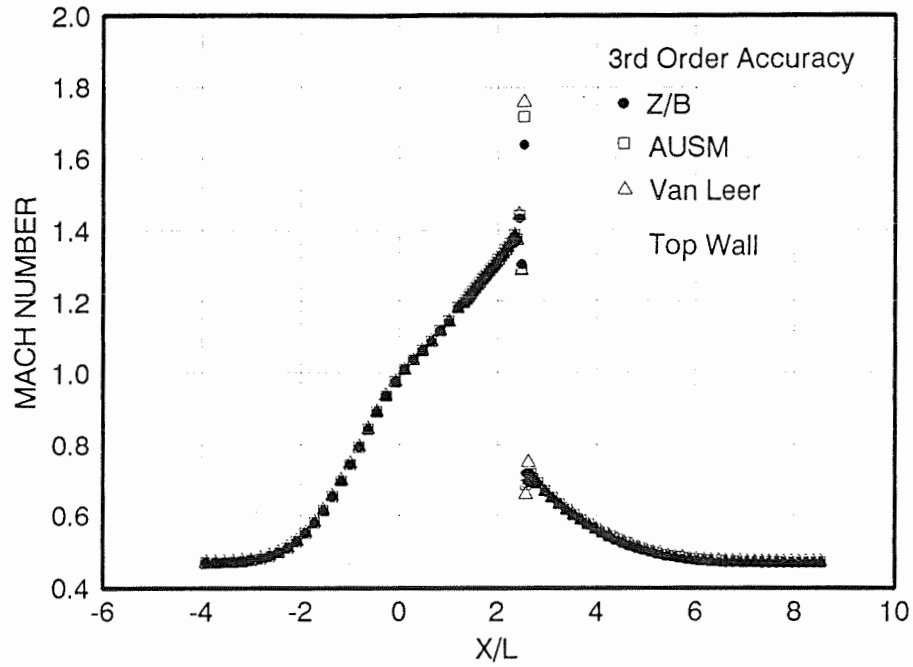

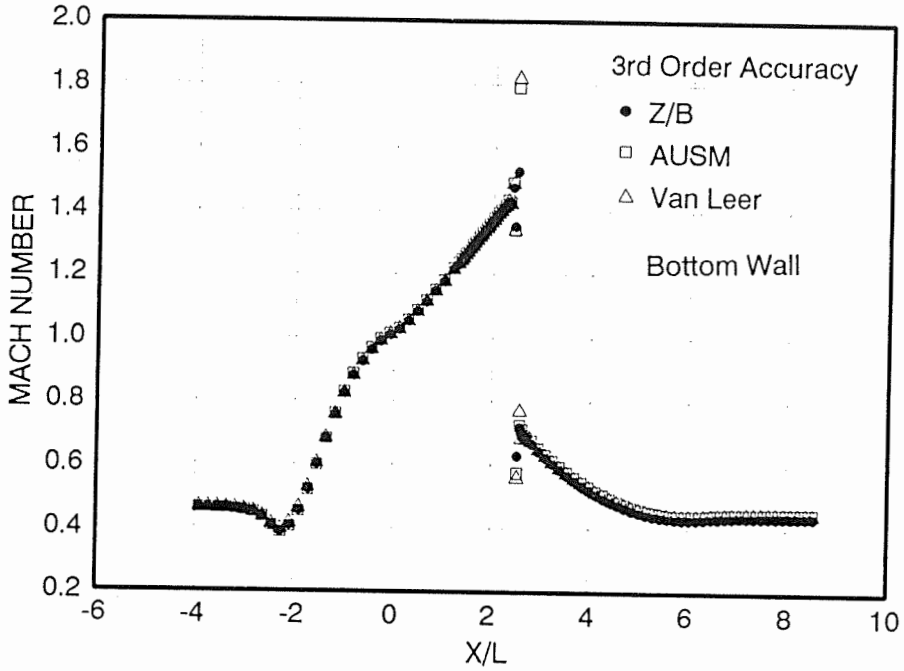

Fig. 6.2. (17) Mach number distributions along the walls of the inlet-diffuser with grid 101 x 31

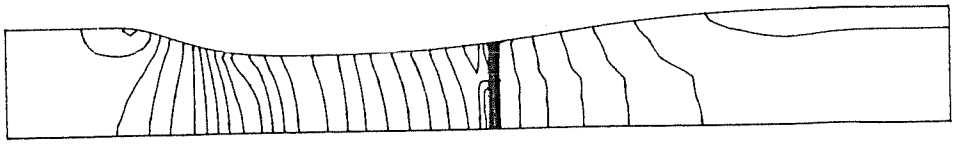

Van Leer Scheme

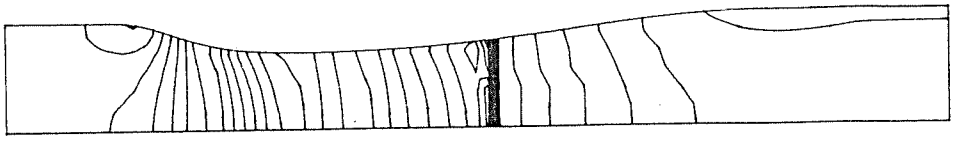

AUSM Scheme

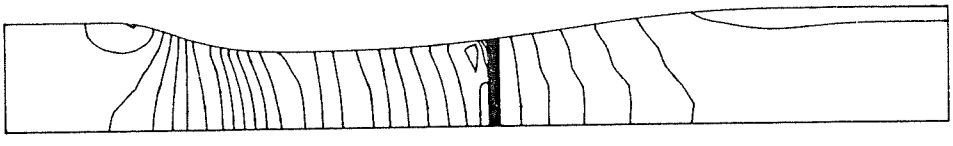

The Present Scheme

Fig. 6.2. (18) The Mach number contours of the inlet-diffuser calculated by using the third order differencing with 101 x 31 x 31

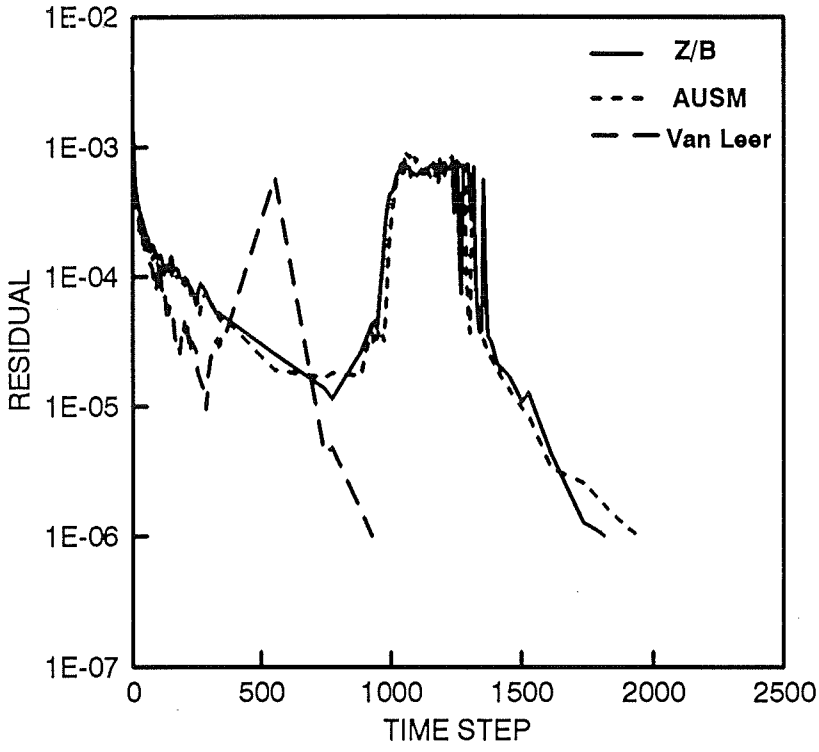

Fig. 6.2. (19) Convergence histories of the 3D inlet-diffuser by using the third order differencing

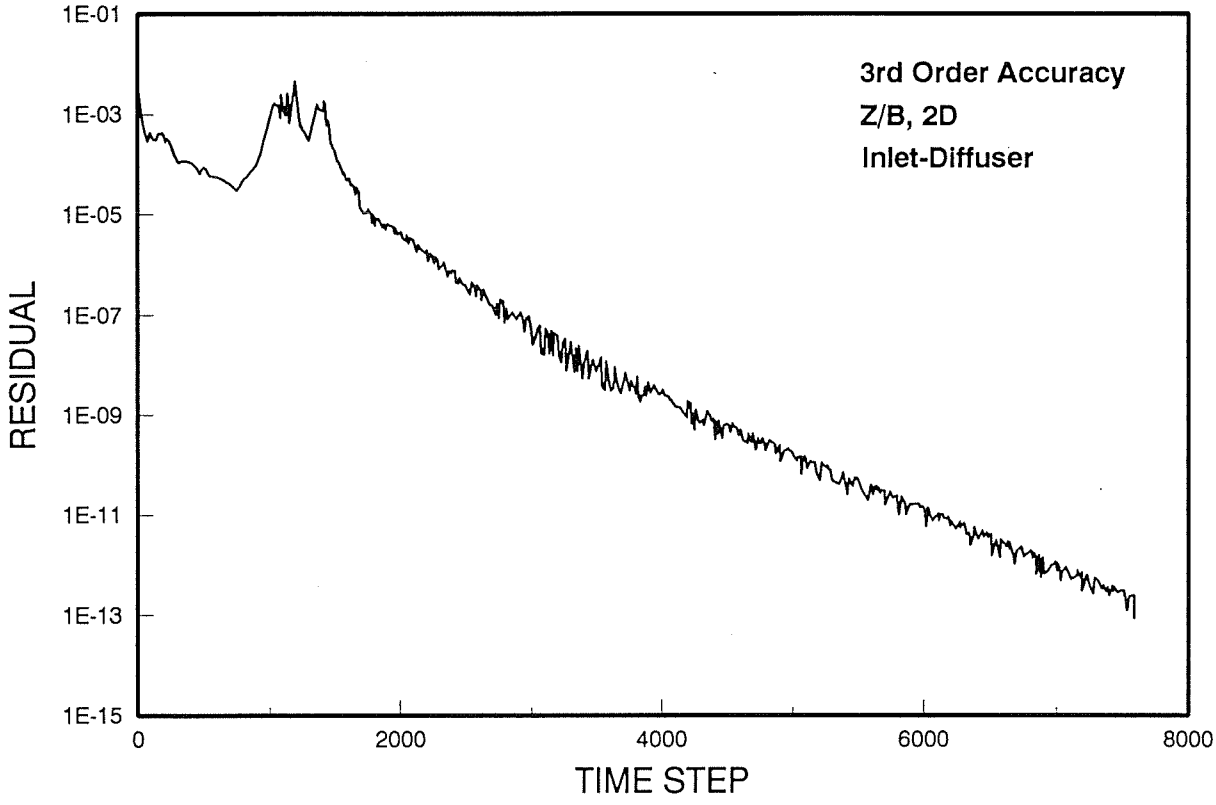

Fig. 6.2. (20) Convergence history of the 2D inlet-diffuser by using the present scheme with grid 101 x 31

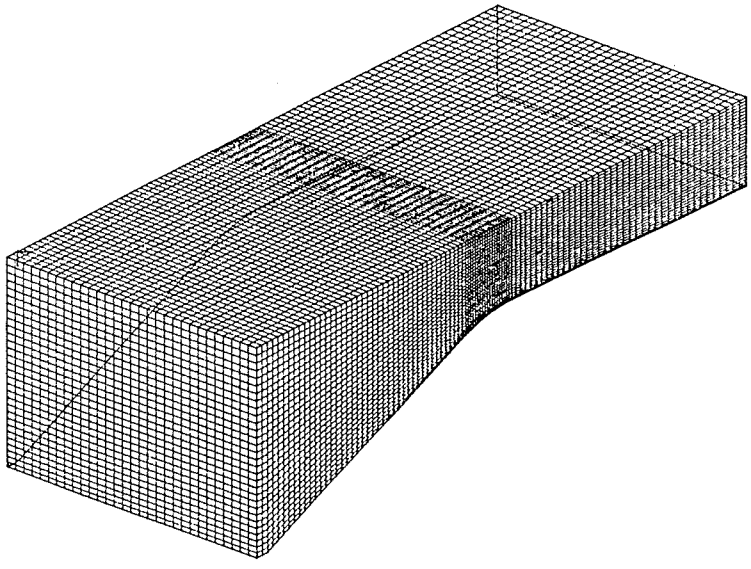

Fig. 6.2. (21) 3D grid of the transonic nozzle with grid 101 x 31 x 31.

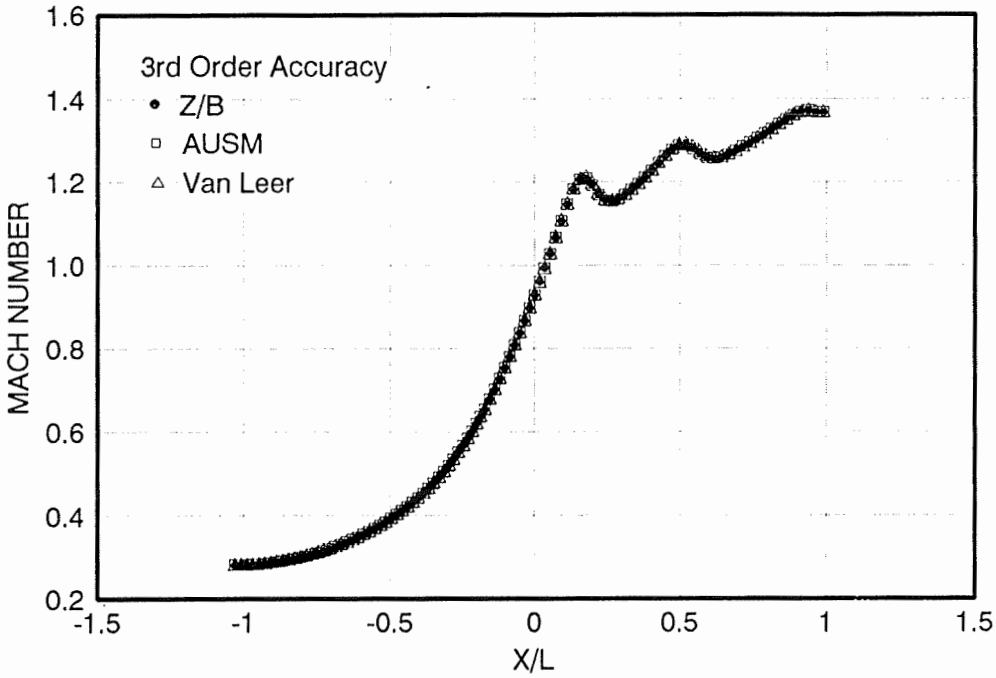

Fig. 6.2. (22) Mach number distributions along the bottom wall center line of the transonic nozzle with grid 101 x 31 x 31

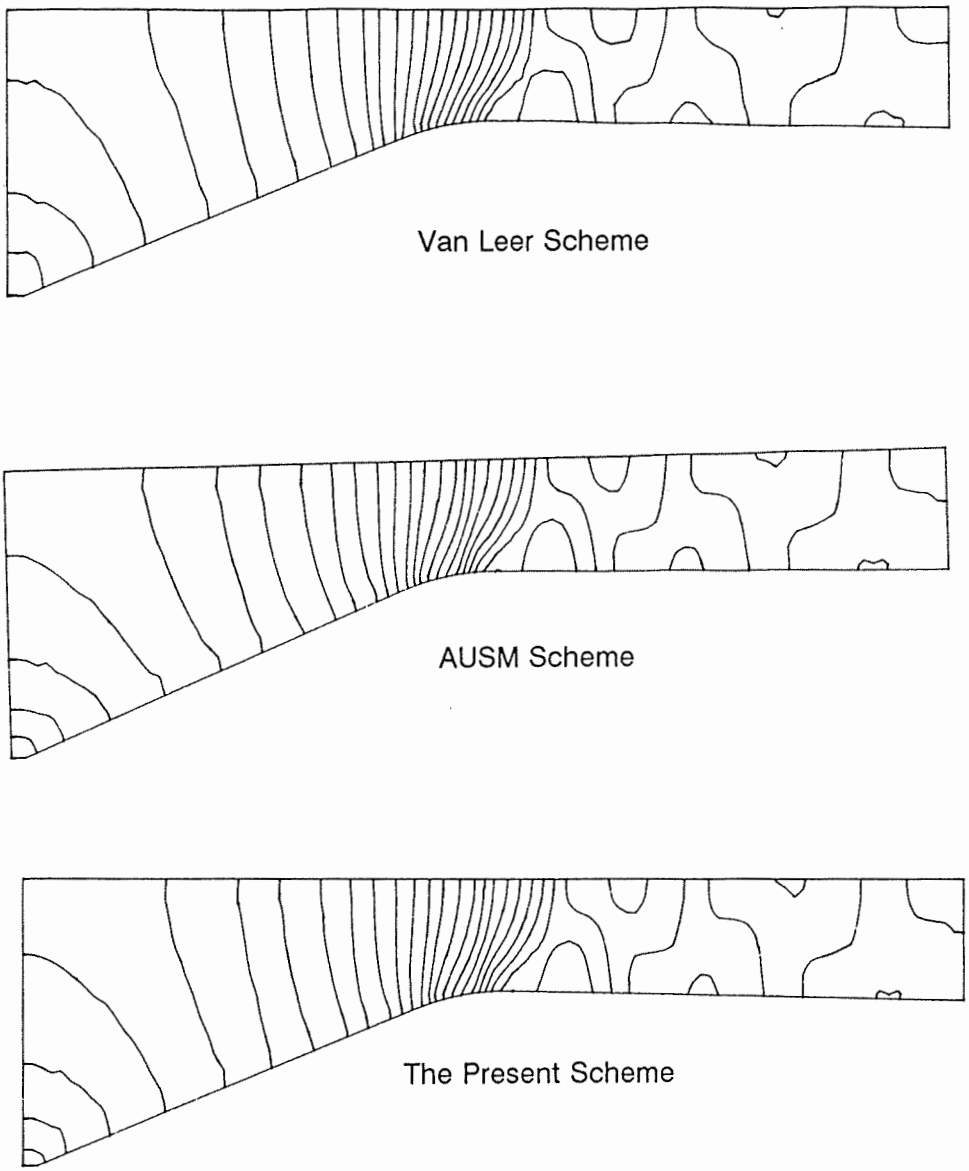

Fig. 6.2. (23) The Mach number contours of the transonic nozzle calculated by using the third order differencing with grid 101 x 31 x 31

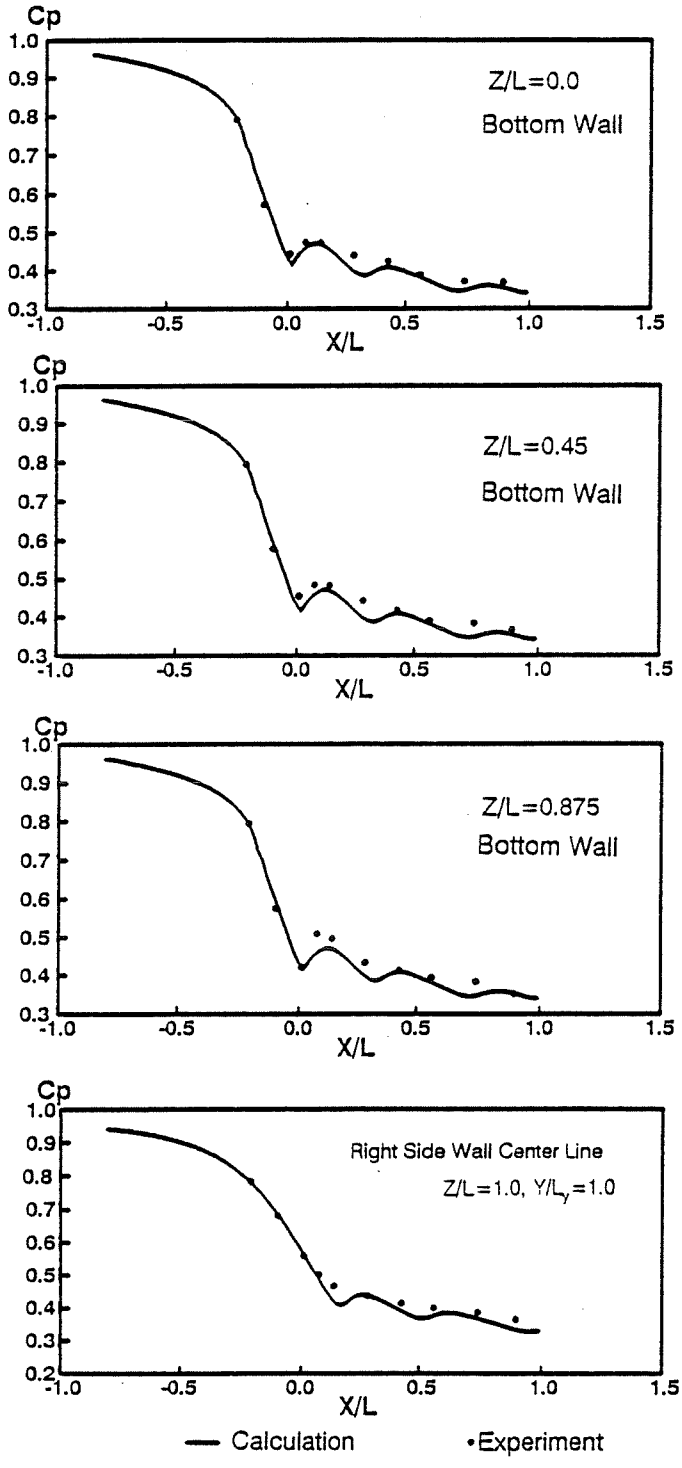

Fig. 6.2. (24) Pressure distributions of the transonic nozzle at four locations in spanwise directions

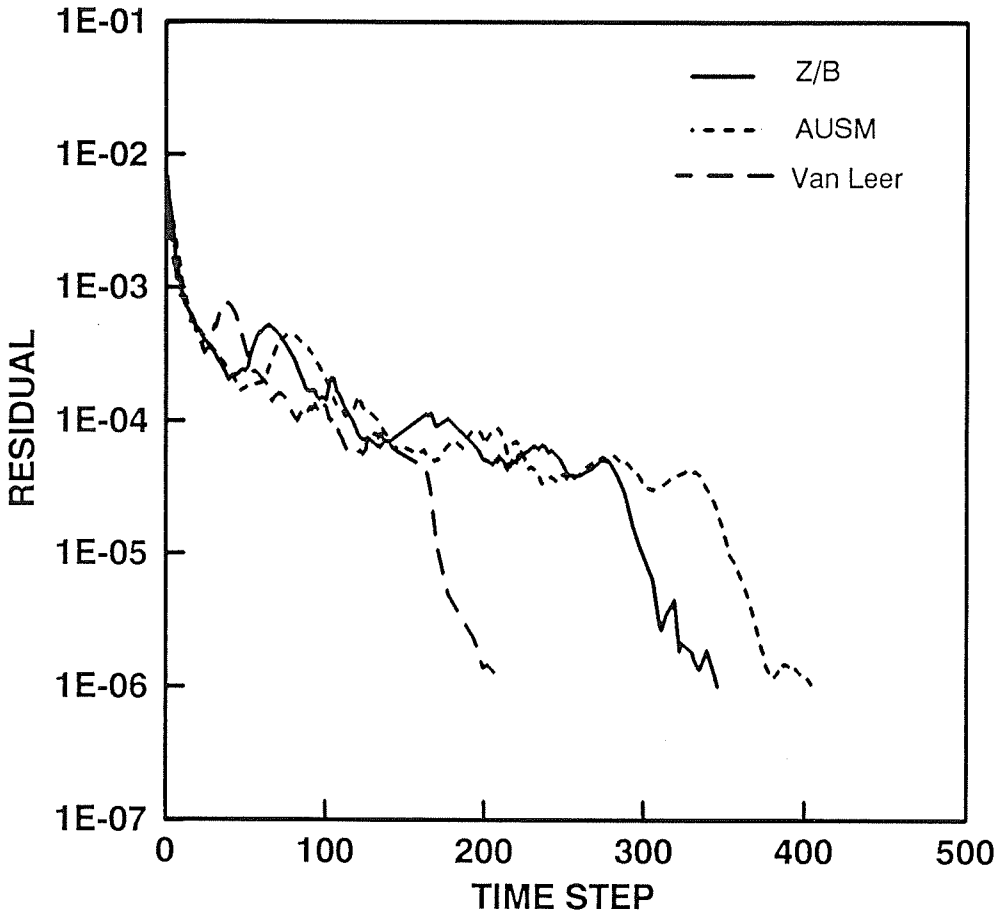

Fig. 6.2. (25) Convergence histories of the transonic nozzle with grid 101 x 31 x 31

ÉCOLE POLYTECHNIQUE DE MONTRÉAL
3 9334 00243121 9